Mixing of Frenkel and Charge-Transfer Excitons and Their Quantum Confinement in Thin Films

Michael Hoffmann
Institut für Angewandte Photophysik, Technische Universität Dresden, 01062 Dresden, Germany,
email: mi-hoffm@iapp.de, web: www.iapp.de/∼mi-hoffm

This manuscript has been published as:
Michael Hoffmann, 'Mixing of Frenkel and Charge-Transfer Excitons and Their Quantum Confinement in Thin Films', in: V. M. Agranovich and G. F. Bassani (Eds.), Electronic Excitations in Organic Multilayers and Organic Based Heterostructures, Elsevier, Amsterdam, 2003, pp. 221–292, Chapter 5, (Thin Films and Nanostructures, Vol. 31).

Contents

1 Introduction

For opto-electronic applications of organic semiconductors, a microscopic understanding of the lowest excited states is essential for further developments. This chapter reviews a minimum set of phenomena that are relevant for one particular class of organic semiconductors: quasi-one-dimensional molecular crystals. It is based on the concepts of exciton theory for molecular crystals and it therefore excludes polymers and amorphous molecular solids.

Within a one-dimensional theory, the major effects of Frenkel exciton transfer, mixing of Frenkel and charge-transfer (CT) excitons and coupling to one intramolecular vibrational mode are described within a common framework. This framework was developed to model the exciton states of PTCDA (3,4,9,10-perylenetetracarboxylic dianhydride, see Fig. 1) and related perylene pigment dyes.

To understand the optical properties of a semiconductor crystal, one can use two different approaches: One approach is to start from the viewpoint of one-particle states for charge carriers (valence and conduction bands) and then to refine this picture by introducing correlation effect. The correlated many-particle states (e.g. Wannier-Mott excitons) are called large-radius excitons. This approach is useful if the exciton formation is a small energetic effect compared to the formation of the one-particle bands. For example, in GaAs, the one-particle bandwidths are in the order of 2 eV, whereas the binding energy of the Wannier-Mott exciton is only 4.2 meV (cf. e.g. [1]).

The alternative approach starts from the correlated many-particle states of isolated molecules and then introduces intermolecular interactions (small radius exciton theories). This approach is useful if the exciton binding energy is large compared to the one-particle bandwidths and the optical spectra are more closely related to the molecular states than to one-particle crystal states. Such a situation is typical for molecular crystals, which are characterized by small Van-der-Waals interactions between the molecules. Even for crystals with coplanar stacking and relatively strong interactions, e.g. PTCDA, the binding energy of the lowest excitons is in the order of 1 eV,[1] compared to estimated one-particle bandwidths in the order of 0.2 eV (see Section 4.1).

The most basic small radius exciton theory considers only Frenkel excitons, i.e. crystal states are described as superpositions of neutral molecular states. That means, all states in which electrons would be transferred from one molecule to another one are excluded, and the exciton radius defined as the mean separation between the excited electron and the remaining hole is necessarily smaller than one lattice constant. Frenkel exciton theory is now a standard tool described in many reviews and monographs (e.g. [3, 4, 5]). It was extensively applied in the third quarter of the 20th century to describe optical properties of naphthalene and anthracene crystals. In its mature versions, it tries to include as many interactions as possible to obtain quantitative predictions, in particular for the well defined phenomenon of Davydov splitting (see e.g. [6]).

Current interest in molecular crystals concentrates on materials with promising properties

[1] Binding energy of the lowest CT state in PTCDA from Ref. [2]. The lowest Frenkel exciton lies even 0.1 eV below, see Section 4.1.

for opto-electronics. Especially the demand for reasonably high charge-carrier mobilities leads to materials with strong intermolecular interactions. In connection with the demand for exciton energies in the visible range, this draws attention to aromatic dyes in which the molecules form stacks with a close coplanar arrangement of the aromatic system. Prominent examples are derivatives of the perylene tetracarboxylic acid or phthalocyanines. We will use two perylene derivatives as model compounds for this situation:MePTCDI(N-N′-dimethylperylene-3,4,9,10-dicarboximide)andPTCDA(3,4,9,10-perylenetetracarboxylic dianhydride), see Fig. 1).

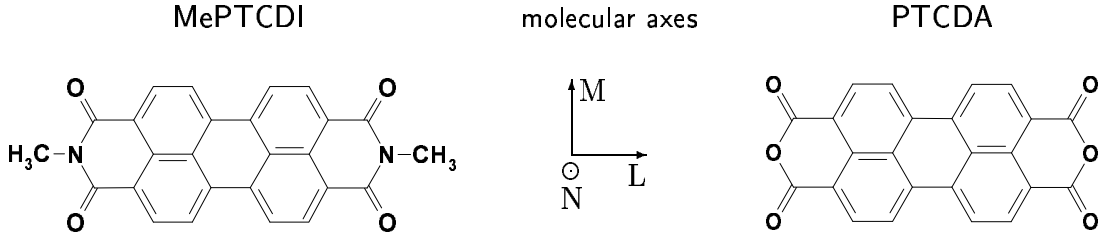

Figure 1:
Chemical structures of the investigated molecules and definition of the molecular axes. MePTCDI = N-N′-dimethylperylene-3,4:9,10-dicarboximide, PTCDA = 3,4:9,10-perylene-tetracarboxylic dianhydride.

PTCDA has become a paradigm because it readily forms highly ordered films [7, 8], while related perylene derivatives have solar cells applications [9, 10, 11]. Several works have sought to understand the PTCDA absorption spectrum and related properties of its electronic excitations [12, 13, 14, 15, 16, 17, 18]. A whole class of PTCDA-derivatives is provided by various substituents in place of the methyl group in MePTCDI. The crystal structures of such PTCDA-derivatives are always characterized by molecular stacks, as shown for MePTCDI in Fig. 2. The geometrical arrangement suggests that the interactions within the stacks will be much stronger than inter-stack interactions. Therefore, we call such materials quasi-one-dimensional. An experimental evidence of the quasi-one-dimensional nature is given by the value of the Davydov splitting, which characterizes the inter-stack interaction between the translationally non-equivalent molecules of the unit cell. In MePTCDI, this Davydov splitting was observed, and it is indeed much smaller than the effects related to interactions within the stacks [16].

A major advantage of PTCDA-derivatives is simple and accessible molecular behavior. The lowest electronic excitation is a dipole allowed π-π^* transition with a strong transition dipole along the long molecular axis (e.g. [19, 20]). It couples predominantly to one effective vibrational mode of the carbon-backbone (cf. Section 3.1), which causes the vibronic progression seen in the absorption spectrum in Fig. 3a between 2.2 and 3.3 eV. The next higher allowed electronic transition is the small feature at 3.4 eV in Fig. 3a, which is related to an M-axis polarized transition [19, 20].

Since the optical spectra of the isolated molecule are determined by the conjugated system they are almost independent of the outer substituents [21]. However, the changes upon crystal formation depend sensitively on the actual crystal structure. Klebe et al. [21] discuss empirically

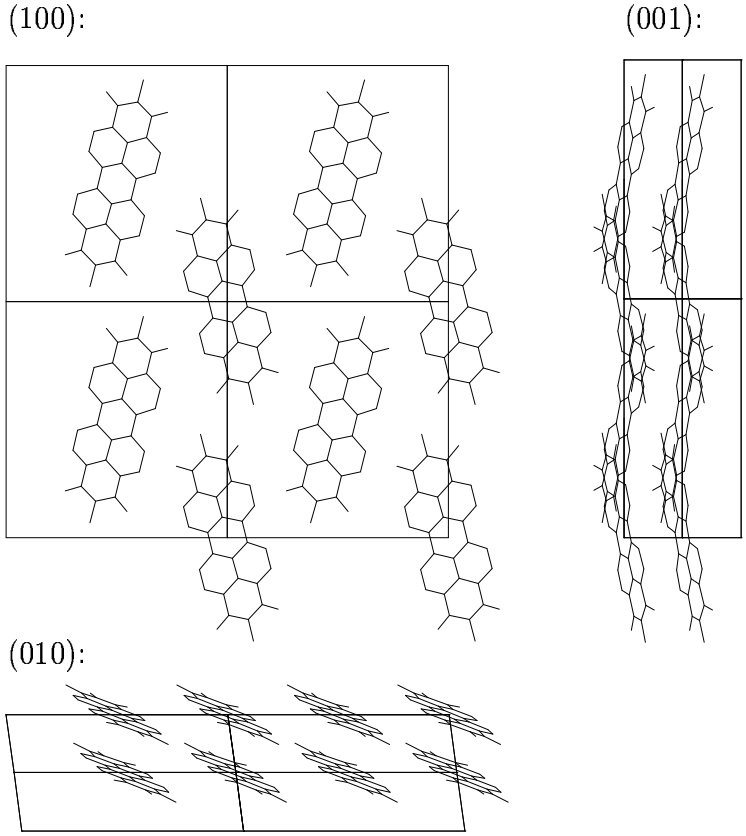

Figure 2:
Crystal structure of MePTCDI from data of Ref. [85]. We show the projections of 2×2 unit cells onto the b-c-plane (100), the a-b-plane (001) and onto the a-c-plane (010). The crystal structure is monoclinic, space group $P2_1/c$, $Z = 2$ molecules per unit cell, $a = 3.874\,\text{Å}$, $b = 15.580\,\text{Å}$, $c = 14.597\,\text{Å}$, $\beta = 97.65°$.

the relation between the crystal absorption spectra and the crystal geometry for a large set of PTCDA derivatives. Because of the quasi-one-dimensional nature of the crystals, and because of the nearly constant distance between the molecular planes in the stacks, the crucial parameter is the lateral displacement of neighboring molecules. We illustrate this dependence for our two model compounds MePTCDI and PTCDA in Fig. 3b and 3c.

On a very rough scale, the crystal spectra in Fig. 3b and 3c still show similarities with the monomer spectrum, which corresponds to the nature of a molecular crystal and motivates the approach by small radius exciton theories. However, on the scale of the vibronic progression (0.17 eV), the differences between the monomer and the crystal spectrum are pronounced. This effect of the intermolecular interactions is much stronger than for the lowest transition in the early model compound anthracene. These strong interactions require the inclusion of charge-

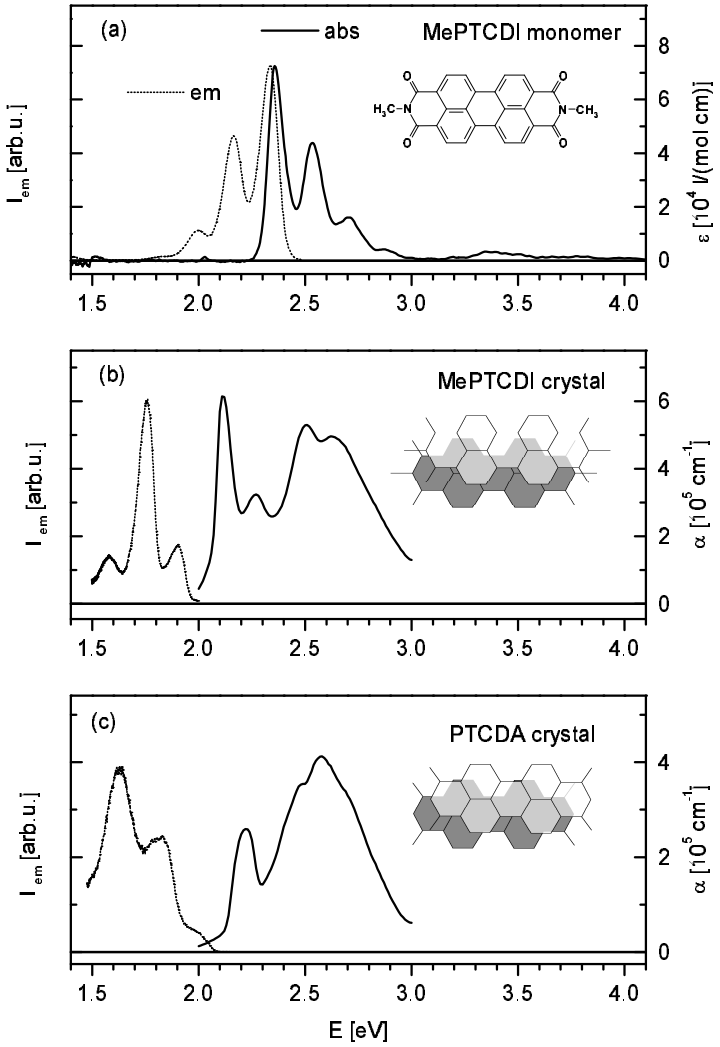

Figure 3:
Absorption and emission spectra of the monomer unit compared to crystal spectra. (a) cw spectra of MePTCDI dissolved in chloroform at room temperature, absorption spectrum (at concenration 0.5 μM) from [16], emission spectrum at concentration 0.3 μM. (b) and (c): absorption spectra of thin polycrystalline films at 10 K, from [16], emission spectra of small single crystals, MePTCDI from [106], PTCDA from [88]. The insets in (b) and (c) show the arrangment of nearest stack neighbors projected onto the molecular planes.

transfer states in the small radius exciton description.

This chapter will present the basic models that are needed to describe the lowest exciton states in such quasi-one-dimensional systems. In Section 2, we describe the purely electronic

problem for a small radius exciton theory in a one-dimensional molecular crystal. We emphasize the relation between the general Merrifield Hamiltonian and minimum models involving just Frenkel and nearest-neighbor charge-transfer states. In Section 3, the tools for the inclusion of internal phonons are discussed. Section 4 demonstrates the path to quantitative application of these models. In Section 4.1, it is shown that the electronic Hamiltonian for Frenkel and CT excitons, together with coupling to internal phonons, can give a realistic description of absorption spectra of the model compounds. In Section 4.2, the implications of such models for finite systems are discussed.

2 Electronic Frenkel and charge-transfer excitons in rigid one-dimensional crystals

2.1 Localized basis states in real and momentum space

Let us first consider the purely electronic states of a one-dimensional molecular crystal. That means, we presume that the positions of all nuclei are fixed in space. In a molecular crystal the constituting molecules retain their individuality to a high degree. This molecular structure provides the basis for small radius exciton theories, in which the *changes* of the electronic structure relative to a reference system of non-interacting molecules are considered.

In many cases, the problem can be conveniently posed in form of empirical model Hamiltonians. That means, one defines the system by introducing a basis set of localized excited states and by choosing the matrix elements between them. Then, the properties of the model can be studied and compared to experiments. On this level, an explicit microscopic definition of the basis states and matrix elements is not necessary.

Let $|\varphi_n^f\rangle$ denote such an excited basis state localized at the lattice position n in the one-dimensional crystal. In simple cases, this might be a localized neutral excitation (Frenkel exciton) or an ionized molecule (charge carrier). Generally, it might be a state with an arbitrary internal structure, which has to be specified by further variables (e.g. the radius of a charge-transfer state). This set of internal variables shall be denoted by f. These states are assumed to form an orthonormal basis:

$$\langle\varphi_m^g|\varphi_n^f\rangle = \delta_{mn}\delta_{gf} \; . \tag{1}$$

We denote the electronic ground state of the crystal by $|o\rangle$ and introduce creation and annihilation operators as

$$X_{nf}^\dagger|o\rangle = |\varphi_n^f\rangle \tag{2}$$

$$X_{nf}|\varphi_n^f\rangle = |o\rangle \; . \tag{3}$$

The Hamiltonian in the representation of these localized basis states consists of on-site energies

$$\epsilon_f = \langle\varphi_n^f|H|\varphi_n^f\rangle \tag{4}$$

and transfer integrals

$$J_{nf,mg} = \langle\varphi_m^g|H|\varphi_n^f\rangle \qquad (n \neq m) \; . \tag{5}$$

Because of the translational symmetry in the crystal, the on-site energies do not depend on the site-index n and the transfer integrals only depend on the distance between the site indices:

$$J_{nf,mg} = J_{(n-m)f,0g} \; . \tag{6}$$

In second quantization, the Hamiltonian can be written as

$$H = \epsilon_f \sum_{nf} X_{nf}^\dagger X_{nf} + \sum_{\substack{nf \\ mg}}{}' J_{nf,mg} X_{nf}^\dagger X_{mg} \; . \tag{7}$$

The prime at the summation symbol indicates that the terms for $n = m$ are to be omitted. In this notation, the transfer terms can be visualized as a transfer of the exciton of type g at site m into an exciton of type f at site n ("$mg \Rightarrow nf$").

The translational symmetry of the crystal can be readily used to split the complete Hilbert space of basis states $|\varphi_{nf}\rangle$ into nonmixing subspaces of definite total momentum. We assume a periodicity length of N and transform all operators into their momentum space representation:

$$X_{kf} = \frac{1}{\sqrt{N}} \sum_n \mathrm{e}^{-\mathrm{i}kn} X_{nf} \ . \tag{8}$$

Here, the coordinate k of the quasi-momentum takes the values

$$k = \frac{2\pi}{N} l \quad \text{with} \quad l = \ldots, -1, 0, +1, \ldots \quad \text{and} \quad -\frac{N}{2} < l \leq +\frac{N}{2} \ . \tag{9}$$

The back-transformation is given by

$$X_{nf} = \frac{1}{\sqrt{N}} \sum_k \mathrm{e}^{\mathrm{i}kn} X_{kf} \ . \tag{10}$$

In this momentum space representation, operators with different k do not mix anymore:

$$X^\dagger_{kf} X_{k'g} = \delta_{kk'} X^\dagger_{kf} X_{kg} \tag{11}$$

This can be proven by inserting the momentum space representation (8) into (11)

$$X^\dagger_{kf} X_{k'g} = \frac{1}{N} \sum_{nn'} \mathrm{e}^{\mathrm{i}(kn - k'n')} X^\dagger_{nf} X_{n'g}$$

and introducing a new summation index $m = n' - n$. Because of the translational symmetry and the periodic boundary conditions, we can substitute $X^\dagger_{nf} X_{(n+m)g} \Rightarrow X^\dagger_{0f} X_{mg}$ and obtain

$$X^\dagger_{kf} X_{k'g} = \frac{1}{N} \sum_n \mathrm{e}^{-\mathrm{i}(k-k')n} \sum_m \mathrm{e}^{-\mathrm{i}km} X^\dagger_{0f} X_{mg} \ .$$

Using the identity

$$\sum_n \mathrm{e}^{-\mathrm{i}(k-k')n} = N\delta_{kk'} \quad \text{for all } k,k' \text{ from Eq. (9)} \ , \tag{12}$$

Eq. (11) is obtained.

Now, the back-transformation (10) can be inserted into the real space representation of H from Eq. (7). If the relation (11) as well as the arguments for its proof are used, the Hamiltonian takes the form:[2]

$$H = \sum_k H_k \tag{13}$$

$$H_k = \sum_f \epsilon_f X^\dagger_{kf} X_{kf} + \sum_{fg} L^{fg}_k X^\dagger_{kf} X_{kg} \ . \tag{14}$$

[2] Cf. Ref. [4, p. 123] or [22] for the case of Frenkel excitons.

Here, the symbol L_k^{fg} is used to abbreviate the lattice sum

$$L_k^{fg} = \sum_{m \neq 0} \mathrm{e}^{\mathrm{i}km} J_{0f,mg} \; . \tag{15}$$

Eq. (14) describes the mixing of the various momentum space basis states (8) within the subspace of a given total momentum k. The dimension of this k-subspaces is determined by the number F of localized basis states at a fixed position. The aim of an empirical small-radius exciton model is the identification of a small number of relevant basis states.

2.2 Model Hamiltonians for Frenkel and charge-transfer states

One of the simplest examples is the following Frenkel exciton Hamiltonian. As localized basis states one considers states $|n\rangle$ in which molecule number n is in the first excited state whereas all other molecules are in the electronic ground state. A nearest-neighbor hopping model for Frenkel excitons can now be written as

$$H_{\mathrm{NN}}^{\mathrm{FE}} = \epsilon_{\mathrm{FE}} \sum_n a_n^\dagger a_n + J \sum_n (a_n^\dagger a_{n+1} + a_{n+1}^\dagger a_n) \tag{16}$$

Here, ϵ_{FE} denotes the on-site energy of a localized Frenkel exciton and J the nearest-neighbor exciton transfer integral (hopping integral). If introduced as an empirical model, Hamiltonian (16) reflects no more than heuristic assumptions about the physical situation. One assumes that only one excited state of the molecule is important, one assumes that localized basis states can be introduced corresponding to this excited molecular state and one assumes that only the nearest-neighbor matrix elements are important. A strict microscopic justification and a derivation of the precise meaning of the model parameters is another task on which we will not focus here.

In the case of the Frenkel exciton Hamiltonian (16), the connection to microscopic theory is well established (a widely available review is given in Ref. [4]). In this case, the localized functions $|n\rangle$ are strictly identified with the eigenfunctions of the noninteracting case, and their orthogonality has to be introduced as an approximation. From the analysis of the Schrödinger equation with the complete interaction Hamiltonian, the model parameters can be related to exact expressions using molecular wave functions. For example, it is seen that the on-site energy ϵ_{FE} deviates from the excitation energy of the noninteracting molecule by a solvent shift term. Furthermore, the nature of the involved approximations becomes clear. In this case, one is working in the Heitler-London approximation, which is valid only for $|J| \ll \epsilon_{\mathrm{FE}}$.

Using the representation in momentum space, k-states according to Eq. (8) can be introduced:

$$a_k = \frac{1}{\sqrt{N}} \sum_n \mathrm{e}^{-\mathrm{i}kn} a_n \; . \tag{17}$$

Then, the Frenkel exciton Hamiltonian (16) takes the diagonal form

$$H_{\mathrm{NN}}^{\mathrm{FE}} = \sum_k H_k \tag{18}$$

$$H_k = (\epsilon_f + 2J \cos k) a_k^\dagger a_k \; . \tag{19}$$

Thus, the momentum space Frenkel excitons $a_k^\dagger|o\rangle$ are already eigenstates of the Hamiltonian $H_{\mathrm{NN}}^{\mathrm{FE}}$. They form an energy band

$$E(k) = \epsilon_f + 2J\cos k \qquad k \in [0, \pi] \; . \tag{20}$$

The Frenkel exciton model from Eq. (16) can be directly extended to the case of a three-dimensional crystal with inclusion of arbitrary exciton transfer integrals $J_{\mathbf{n},\mathbf{m}}$. Then, it reads

$$H_{\mathrm{3D}}^{\mathrm{FE}} = \epsilon_{\mathrm{FE}} \sum_{\mathbf{n}} a_{\mathbf{n}}^\dagger a_{\mathbf{n}} + {\sum_{\mathbf{n},\mathbf{m}}}' J_{\mathbf{n},\mathbf{m}} a_{\mathbf{n}}^\dagger a_{\mathbf{m}} \; . \tag{21}$$

Here, the site indices $\mathbf{n}$, $\mathbf{m}$ are three-dimensional vectors. The second sum runs over all pairs $\mathbf{n}$, $\mathbf{m}$ with $\mathbf{n} \neq \mathbf{m}$, which is symbolized by the prime at the summation index. Such a type of exciton model was already suggested by Frenkel in 1931 [23, 24] and first applied to molecular crystals by Davydov in 1948 [25].

One way to extend the two-level model (21) is to include higher excited states of the molecule. For the one-dimensional crystal, this leads to model Hamiltonians of the form

$$H = \sum_{nf} \epsilon_f a_{nf}^\dagger a_{nf} + {\sum_{\substack{nf \\ mg}}}' J_{nf,mg} a_{nf}^\dagger a_{mg} \; , \tag{22}$$

where $a_{nf}^\dagger$ now creates a localized Frenkel exciton in level f at molecule n with on-site energy ϵ_f and $J_{nf,mg}$ denotes the hopping integrals between the various localized states. The prime at the summation excludes the terms with $n = m$.

The interaction of various molecular excited states (mixing of molecular configurations) as in Eq. (22) was extensively investigated. It was first considered by Craig [26] to explain the experimentally observed polarization ratios of the Davydov components in anthracene crystals. A general treatment in second quantization was given by Agranovich [27]. Reviews are available in Refs. [28, 4, 5].

Another extension of the two-level model (21) is the inclusion of charge-transfer states (CT states). In the one-dimensional crystal, a localized CT state can be written as

$$|n, f\rangle = c_{n,f}^\dagger |o\rangle \; , \tag{23}$$

meaning that an electron is transferred from molecule n, where it leaves a hole, to molecule $n + f$. If arbitrary electron-hole distances f are allowed, the complete set of the CT basis states $|n, f\rangle$ can describe not only bound CT states but also unbound states corresponding to free charge carriers.

CT states are the lowest electronic excitations in so-called charge-transfer crystals, which are mixed crystals containing donor and acceptor type molecules. Prominent example are anthracene-PMDA (anthracene as donor and pyromellitic dianhydride as acceptor) or TTF-TCNQ (tretrathiafulvalene as donor and tetracyano-p-quinodimethane as acceptor). The fundamental optical properties of such crystals are reviewed e.g. in Ref. [29], and electronic model

Hamiltonians in second quantization are reviewed e.g. in Ref. [30]. In such charge-transfer crystals, the lowest electronic excitations are pure CT states and Frenkel excitons can be neglected. We are interested, however, in one-component molecular crystals. In this case, CT excitons are expected to lie energetically above — but maybe close — to the lowest Frenkel excitons. Then, both types of states have to be included in model Hamiltonians, and the true eigenstates can be of mixed character. The possibility of such mixed states was first pointed out in 1957 by Lyons [31]. A detailed theoretical investigation of this general case was presented 1961 in the work of Merrifield [32]. This model was extended for a description of absorption by Hernandez and Choi [33] and for the inclusion of several Frenkel excitons by Pollans and Choi [34]. In anthracene crystals, CT states are essential to describe electro-absorption spectra [35, 36, 37, 38, 39] and charge-generation mechanisms [40]. However, their effect on the low energy optical absorption and emission spectra is still very small. In quasi-one dimensional crystals with close coplanar arrangement of the molecules, Frenkel and CT states are considered to be strongly mixed even in the lowest energy region [15, 16, 41, 17] and thus this mixing is an essential feature even for the description of the linear absorption spectra.

The general one-dimensional Merrifield model for Frenkel-CT mixing [32] considers one electron (position n_e) and one hole (position n_h), which can perform nearest neighbor hops independently of each other. The corresponding transfer integrals are t_e and t_h, respectively. Electron-hole correlation is introduced by a Coulombic attraction potential $V(n_\mathrm{e} - n_\mathrm{h})$. The special situation $n_\mathrm{e} = n_\mathrm{h}$ is considered as a Frenkel exciton with an on-site energy ϵ_FE. This Frenkel exciton can perform arbitrary hops with hopping integrals $J_{n,m}$ as in the Frenkel exciton Hamiltonian (22).

In Merrifield's work, the localized basis states are expressed by electron and hole positions and the Frenkel exciton occurs just as a special position. Now, we will write down his Hamiltonian in our notation of Frenkel and CT excitons. For Merrifield's general case, our notation becomes much less convenient but it reveals the path towards simplified small radius exciton Hamiltonians. First, we explicitly split the Merrifield Hamiltonian into a Frenkel part H^FE, a CT part H^CT and a term that mixes Frenkel and CT states $H^\mathrm{FE-CT}$:

$$H_\mathrm{Merri} = H^\mathrm{FE}_\mathrm{Merri} + H^\mathrm{CT}_\mathrm{Merri} + H^\mathrm{FE-CT}_\mathrm{Merri} \tag{24}$$

The Frenkel part corresponds to the Frenkel exciton Hamiltonian (22) with just one molecular configuration:

$$H^\mathrm{FE}_\mathrm{Merri} = \epsilon_\mathrm{FE} \sum_n a_n^\dagger a_n + {\sum_{nm}}' J_{n,m} a_n^\dagger a_m \tag{25}$$

The CT part treats the nearest-neighbor hopping of electrons and holes, which always means the transfer of a CT state with separation f into a CT state with separation $f \pm 1$. Since f can be arbitrarily large, these CT basis states can also describe the motion of an unbound (free) electron-hole pair. However, all Frenkel states (which correspond to an electron-hole separation $f = 0$) have to be excluded now, which we denote by primes at the summation symbols:

$$H^\mathrm{CT}_\mathrm{Merri} \quad = \quad {\sum_{nf}}' V(f) c_{n,f}^\dagger c_{n,f}$$

$$+\sum_{nf}{}' \left[t_{\rm h} \underbrace{c^\dagger_{n+1,f-1} c_{n,f}}_{n \stackrel{\rm h}{\rightarrow} n+1} + t_{\rm h} \underbrace{c^\dagger_{n-1,f+1} c_{n,f}}_{n \stackrel{\rm h}{\rightarrow} n-1} + \text{h.c.} \right]$$

$$+\sum_{nf}{}' \left[t_{\rm e} \underbrace{c^\dagger_{n,f+1} c_{n,f}}_{n+f \stackrel{\rm e}{\rightarrow} n+f+1} + t_{\rm e} \underbrace{c^\dagger_{n,f-1} c_{n,f}}_{n+f \stackrel{\rm e}{\rightarrow} n+f-1} + \text{h.c.} \right] \tag{26}$$

The first sum in this notation covers the on-site energies of the CT states, which only depend on the separation f. The second sum includes all nearest-neighbor hops of a hole ("$n \stackrel{\rm h}{\rightarrow} n \pm 1$"), and the third sum the corresponding hops of an electron ("$n+f \stackrel{\rm e}{\rightarrow} n+f+1 \pm 1$").

Finally, the Frenkel-CT mixing part in Merrifield's Hamiltonian can be expressed as:

$$\begin{aligned} H^{\rm FE-CT}_{\rm Merri} &= \sum_n \left[t_{\rm e} \underbrace{a^\dagger_n c_{n,+1}}_{n+1 \stackrel{\rm e}{\rightarrow} n} + t_{\rm e} \underbrace{a^\dagger_n c_{n,-1}}_{n-1 \stackrel{\rm e}{\rightarrow} n} + \text{h.c.} \right] \\ &\quad + \sum_n \left[t_{\rm h} \underbrace{a^\dagger_n c_{n+1,-1}}_{n+1 \stackrel{\rm h}{\rightarrow} n} + t_{\rm h} \underbrace{a^\dagger_n c_{n-1,+1}}_{n-1 \stackrel{\rm h}{\rightarrow} n} + \text{h.c.} \right] \end{aligned} \tag{27}$$

Here, the first sum describes the processes in which a nearest neighbor CT state (separation $f = 1$) is transferred into a Frenkel exciton by a hop of the electron to the position of the hole ("$n \pm 1 \stackrel{\rm e}{\rightarrow} n$"). The reverse transfer of a Frenkel into a CT state is included in the Hermitian conjugated part. The second sum describes the analogous process for the jump of the hole ("$n \pm 1 \stackrel{\rm h}{\rightarrow} n$").

At this stage, the separation of the charge hopping processes into $H^{\rm CT}_{\rm Merri}$ and $H^{\rm FE-CT}_{\rm Merri}$ seems like an unnecessary complication. However, this separation makes an important point obvious: The charge hops in $H^{\rm CT}_{\rm Merri}$ and in $H^{\rm FE-CT}_{\rm Merri}$ are not identical, since they connect different kinds of states. Only in an uncorrelated one-particle picture, it would not make a difference for the hopping integrals whether the final position is neutral or occupied by an opposite charge. Strictly speaking, even the hopping integrals that connect the various CT states in $H^{\rm CT}_{\rm Merri}$ might be different from each other. Using one value for all one-particle hopping integrals is a clearly definable approximation in the model. An explicit distinction of the various hops becomes more important with the rising availability of computational methods that allow microscopic calculations of both dissociation integrals and one-particle hopping integrals on highly correlated levels.

As a second important point, the separation into $H^{\rm CT}_{\rm Merri}$ and $H^{\rm FE-CT}_{\rm Merri}$ allows the approximate separation of low-lying small radius excitons. Let us first consider $H^{\rm CT}_{\rm Merri}$. The basis states that are mixed by this CT Hamiltonian have on-site energies $V(f)$. In the simplest approximation, which was also used by Merrifield, the on-site energies follow Coulomb's law $V(f) = V_1/|f|$.

Then, the separation between the lowest CT states ($|f| = 1$) and the second lowest ones ($|f| = 2$) is $V_1/2$. In our model compound PTCDA, the lowest CT states lie at approximately 2.3 eV (cf. Section 4.1) giving a separation of 1.2 eV. Detailed microscopic models predict a separation of 0.5 eV [2].

The mixing of this states with the higher states is determined by the charge carrier hopping integrals t. In molecular crystals, these hopping integrals are small and even for quasi-one-dimensional materials such as PTCDA, values on the order of 0.05 eV are typically discussed (cf. Section 4.1). These values are much smaller than the separation from higher CT states. Thus, the lowest CT states will mix only weakly with the higher CT states. In contrast, the separation of the higher CT states becomes smaller and tends to zero for $f \to \infty$. Thus, these higher states will strongly mix with each other.

From this discussion we can derive the qualitative structure of the eigenstates of $H^{\mathrm{CT}}_{\mathrm{Merri}}$. The lowest eigenstates will be dominated by the two lowest CT basis states ($f = -1, +1$). In the momentum space representation, the CT Hamiltonian for the lowest states becomes

$$H^{\mathrm{CT}}_{\mathrm{Merri}}(k) = V(1)(c^{\dagger}_{k,-1}c_{k,-1} + c^{\dagger}_{k,+1}c_{k,+1}) \tag{28}$$

Thus, the two lowest CT basis states $|k, +1\rangle$ and $|k, -1\rangle$ are two degenerate eigenstates. However, these states do not yet represent the symmetry of the Hamiltonian for inversion about any site n. Therefore, one can introduce symmetry adapted basis states

$$\frac{|k, +1\rangle \pm |k, -1\rangle}{\sqrt{2}} \; .$$

These symmetry adapted states are the simplest version of small radius CT states in a crystal with translational and inversion symmetry. The mixing of such states with Frenkel excitons will be the main topic of the following sections.

For the higher CT states, the matrix elements between CT states with different separation f will be in the same order or larger than their decreasing energetic separation. Therefore, it is not possible anymore to isolate weakly interacting subspaces in the Hamiltonian that correspond to CT states of a certain radius f. In Merrifield's analytical solution [32], this situation is treated exactly. Qualitatively, the situation now becomes similar to a Wannier-Mott exciton since for large exciton radii the discrete lattice structure of the molecular crystal can be replaced by a continuum model with effective masses for the charge carriers.[3]

Now, we will consider the situation that only the lowest CT states $|k, \pm 1\rangle$ can mix with the Frenkel states $|k, 0\rangle$. If we neglect all higher CT states in the Merrifield Hamiltonian (24), we arrive at a much simpler Hamiltonian that includes only nearest-neighbor CT states and mixing of these states with Frenkel excitons at the site of either the electron or the hole. If, as a further simplification, we also reduce the Frenkel exciton hopping to nearest neighbors, we arrive at a

[3]The equivalence between both models can be directly seen in the difference equations (18) of Ref. [32] for the expansion coefficients $\alpha(n)$. For large radii n, $(\alpha(n-1)+\alpha(n+1))/2$ can be approximated by the second derivative $\partial^2\alpha/\partial n^2$ and the difference equation transforms into the Schrödinger equation for the relative coordinate of an electron-hole pair in a Coulomb potential.

nearest-neighbor Hamiltonian of the form

$$
\begin{aligned}
H_{\mathrm{NN}} &= H_{\mathrm{NN}}^{\mathrm{FE}} + H_{\mathrm{NN}}^{\mathrm{CT}} + H_{\mathrm{NN}}^{\mathrm{FE-CT}} \\
H_{\mathrm{NN}}^{\mathrm{FE}} &= \epsilon_{\mathrm{FE}} \sum_n a_n^\dagger a_n + J \sum_n (a_n^\dagger a_{n+1} + a_{n+1}^\dagger a_n) \\
H_{\mathrm{NN}}^{\mathrm{CT}} &= \epsilon_{\mathrm{CT}} \sum_{nf} c_{nf}^\dagger c_{nf} \\
H_{\mathrm{NN}}^{\mathrm{FE-CT}} &= \sum_n \left\{ t_{\mathrm{e}} (\underbrace{a_n^\dagger c_{n,+1}}_{n+1 \overset{\mathrm{e}}{\to} n} + \underbrace{a_n^\dagger c_{n,-1}}_{n-1 \overset{\mathrm{e}}{\to} n}) + t_{\mathrm{h}} (\underbrace{a_n^\dagger c_{n+1,-1}}_{n+1 \overset{\mathrm{h}}{\to} n} + \underbrace{a_n^\dagger c_{n-1,+1}}_{n-1 \overset{\mathrm{h}}{\to} n}) + \mathrm{h.c.} \right\} .
\end{aligned}
\tag{29}
$$

In this nearest-neighbor version of the Merrifield-Hamiltonian, the FE-CT mixing term is identical with the original Eq. (27).

After Fourier transformation $a_n \to a_k$ and $c_n \to c_k$ according to Eq. (8), the Hamiltonian becomes:

$$
\begin{aligned}
H_{\mathrm{NN}} &= \sum_k \left(H_{\mathrm{NN}}^{\mathrm{FE}}(k) + H_{\mathrm{NN}}^{\mathrm{CT}}(k) + H_{\mathrm{NN}}^{\mathrm{FE-CT}}(k) \right) \\
H_{\mathrm{NN}}^{\mathrm{FE}}(k) &= (\epsilon_{\mathrm{FE}} + 2J\cos k) a_k^\dagger a_k \\
H_{\mathrm{NN}}^{\mathrm{CT}}(k) &= \epsilon_{\mathrm{CT}} \left(c_{k,+1}^\dagger c_{k,+1} + c_{k,-1}^\dagger c_{k,-1} \right) \\
H_{\mathrm{NN}}^{\mathrm{FE-CT}}(k) &= a_k^\dagger \left[(t_{\mathrm{e}} + t_{\mathrm{h}} \mathrm{e}^{-\mathrm{i}k}) c_{k,+1} + (t_{\mathrm{e}} + t_{\mathrm{h}} \mathrm{e}^{\mathrm{i}k}) c_{k,-1} \right] + \mathrm{h.c.}
\end{aligned}
\tag{30}
$$

Now, the Frenkel-CT mixing part in $H_{\mathrm{NN}}^{\mathrm{FE-CT}}(k)$ can be further simplified by introducing symmetry adapted CT operators with even or odd symmetry with respect to change of the direction of the charge-transfer:[4]

$$
\tilde{c}_{k\pm} \equiv \frac{1}{\sqrt{2} t_k} \left[(t_{\mathrm{e}} + t_{\mathrm{h}} \mathrm{e}^{-\mathrm{i}k}) c_{k,+1} \pm (t_{\mathrm{e}} + t_{\mathrm{h}} \mathrm{e}^{+\mathrm{i}k}) c_{k,-1} \right] , \tag{31}
$$

where

$$
t_k \equiv \sqrt{t_+^2 \cos^2 \frac{k}{2} + t_-^2 \sin^2 \frac{k}{2}} \tag{32}
$$

with

$$
t_\pm \equiv t_{\mathrm{e}} \pm t_{\mathrm{h}} . \tag{33}
$$

The Hamiltonian for the CT states then simplifies to:

$$
H_{\mathrm{NN}}^{\mathrm{CT}}(k) = \epsilon_{\mathrm{CT}} \left\{ \tilde{c}_{k+}^\dagger \tilde{c}_{k+} + \tilde{c}_{k-}^\dagger \tilde{c}_{k-} \right\} \tag{34}
$$

$$
H_{\mathrm{NN}}^{\mathrm{FE-CT}}(k) = \sqrt{2}\, t_k a_k^\dagger \tilde{c}_{k+} \; + \; \mathrm{h.c.} \tag{35}
$$

[4] $\tilde{c}_{k+}$ is directly chosen as the term $[\ldots]$ multiplied with an - at first unknown - normalization constant. The normalization constant $1/(\sqrt{2}t_k)$ is then obtained by demanding the correct expression of $H_{\mathrm{NN}}^{\mathrm{CT}}(k)$ in Eq. (34).

Now, the odd operator $\tilde{c}_{k-}$ does not mix with the Frenkel operators a_k anymore. The odd CT state $\tilde{c}^\dagger_{k-}|o\rangle = |k,1\rangle_-$ is a non-mixing eigenstate of $H^{\rm CT}_{\rm NN}(k)$ and thereby of the complete Frenkel-CT Hamiltonian (30). It lies at the energy $\epsilon_{\rm CT}$ of the localized CT states.

The remaining even part of the k-dependent Hamiltonian can be represented by the two even basis states $|k,0\rangle = a^\dagger_k|o\rangle$ and $|k,1\rangle_+ = \tilde{c}^\dagger_{k+}|o\rangle$. In this representation, it has the form of a 2×2 matrix:

$$\underline{H}_{\rm NN+}(k) = \begin{pmatrix} \epsilon_{\rm FE} + 2J\cos k & \sqrt{2}\,t_k \\ \sqrt{2}\,t_k & \epsilon_{\rm CT} \end{pmatrix} \tag{36}$$

The two eigenstates $|\Psi_j(k)\rangle$ $(j=1,2)$ of this problem are linear combinations

$$|\Psi_j(k)\rangle = u_{{\rm FE}j}(k)|k,0\rangle + u_{{\rm CT}j}(k)|k,1\rangle_+ \,. \tag{37}$$

The composition of the states is characterized by the squared coefficients $|u|^2$ in terms of a Frenkel exciton character

$$F_{{\rm FE}j}(k) \equiv |u_{{\rm FE}j}(k)|^2 = |\langle\Psi_j(k)|a^\dagger_k|o\rangle|^2 \tag{38}$$

and a CT character

$$F_{{\rm CT}j}(k) \equiv |u_{{\rm CT}j}(k)|^2 = |\langle\Psi_j(k)|\tilde{c}^\dagger_{k+}|o\rangle|^2 \,. \tag{39}$$

From the matrix representation (36), one can directly see that the off-diagonal term between Frenkel and CT states is entirely given by t_k. This term depends in a characteristically k-dependent way on the combination of the electron and hole transfer integrals. In particular, one has at the boundaries of the Brillouin zone:

$$\begin{aligned} t_{k=0} &= t_+ = t_{\rm e} + t_{\rm h} \\ t_{k=\pi} &= t_- = t_{\rm e} - t_{\rm h} \,. \end{aligned}$$

If one looks, e.g., only at absorption spectra ($k=0$), the two parameters $t_{\rm e}$ and $t_{\rm h}$ are reduced to one effective parameter t_+.

For illustration, we show several concrete exciton band structures of this Hamiltonian in Figs. 4 and 5. Since an additive constant in the on-site energies has no physical meaning in this model, we always take $\epsilon_{\rm FE} = 0$. An example without FE-CT mixing is shown in Fig. 4a ($t_{\rm e} = t_{\rm h} = 0$). All other pictures demonstrate the situation for various mixing situations, as explained in the figure captions. The characters of the bands (FE or CT) are always indicated by the upper and lower stripes. The vertical height of each stripe is always proportional to the character $F(k)$.

The visualization scheme of Figs. 4 and 5 easily allows to realize the two main features that determine the exciton band structure. The first important feature is the overall dispersion of the contributing Frenkel exciton. The pure Frenkel exciton band is a simple cosine function as seen in Fig. 4a. If this band is mixed with other bands, also the FE character is distributed over all mixed bands. However, the center of mass of the FE character

$$\bar{E}_{\rm FE}(k) \equiv \sum_j F_{{\rm FE}j}(k) E_j(k) \tag{40}$$

exactly follows the dispersion of the pure FE band:

$$\bar{E}_{\mathrm{FE}}(k) = \epsilon_{\mathrm{FE}} + 2J\cos k \ . \tag{41}$$

The same holds for the center of mass of the CT character:

$$\bar{E}_{\mathrm{CT}}(k) \equiv \sum_j F_{\mathrm{CT}j}(k) E_j(k) \ , \tag{42}$$

and

$$\bar{E}_{\mathrm{CT}}(k) = \epsilon_{\mathrm{CT}} \ . \tag{43}$$

Both identities (41) and (43) follow directly from the theory of unitary transformations: If $\underline{U} = (u_{ij})$ is the transformation matrix that diagonalizes $\underline{H}$ by $\mathrm{diag}(E_j) = \underline{U}^\dagger \underline{H} \underline{U}$, then

$$\sum_j u_{ij}^2 E_j = H_{ii} \ . \tag{44}$$

The physical meaning of Eqs. (41) and (43) is very intuitive: No matter in which way the FE and CT states mix, the original dispersion of these states remains as a center of mass dispersion of the corresponding characters. Therefore, the upper stripes of the FE character will always disperse to lower energies and thus keep on average their original dispersion. This average dispersion can easily be tracked by the eye. By the same token, the average position of the lower stripes represents the dispersion-less band of the pure CT state.

2.3 Characters and transition dipoles of the eigenstates

With knowledge of the eigenstates (37) of our considered Frenkel-CT Hamiltonian (29), we can investigate the transition dipoles these states. Let $\hat{\vec{P}}$ be the total transition dipole operator, which is a one-electron operator acting on all electrons in the system:

$$\hat{\vec{P}} = \sum_i e\vec{r}_i \ . \tag{45}$$

First, we decompose the transition dipole into a Frenkel and CT component by means of Eq. (37):

$$\begin{aligned} \vec{P}_j &= \langle \Psi_j(k) | \hat{\vec{P}} | o \rangle \\ &= \underbrace{u_{\mathrm{FE}j}(k) \langle k,0 | \hat{\vec{P}} | o \rangle}_{\equiv \vec{P}_{\mathrm{FE}j}} + \underbrace{u_{\mathrm{CT}j}(k)_+ \langle k,1 | \hat{\vec{P}} | o \rangle}_{\equiv \vec{P}_{\mathrm{CT}j}} \ . \end{aligned} \tag{46}$$

The FE component $\vec{P}_{\mathrm{FE}j}$ becomes

$$\vec{P}_{\mathrm{FE}j} = u_{\mathrm{FE}j}(k) \frac{1}{\sqrt{N}} \sum_n \mathrm{e}^{\mathrm{i}kn} \underbrace{\langle n,0 | \hat{\vec{P}} | o \rangle}_{=\vec{p}_{\mathrm{FE}}}$$

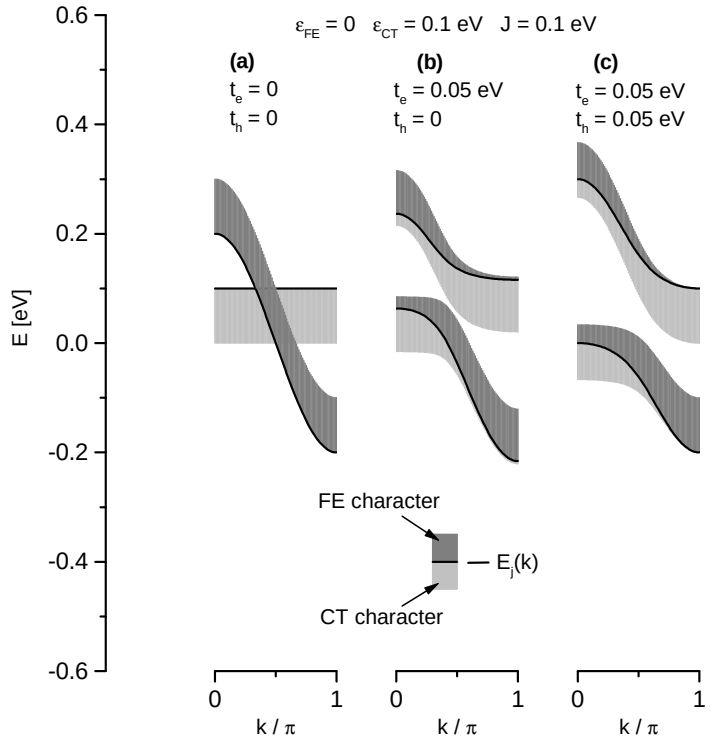

Figure 4:
Exciton bands for increasing charge-transfer parameters t_e, t_h and constant ϵ_FE, ϵ_CT, J. The FE character $F_{\mathrm{FE}j}$ of each band is indicated by the upper stripe, the CT character $F_{\mathrm{CT}j}$ by the lower one (cf. Eqs. (38), (39)). **(a)** With $t_\mathrm{e} = 0$ and $t_h = 0$, all interactions between the FE and CT states are are turned off. The pure CT excitons form a dispersionless band at ϵ_CT, the Frenkel excitons form a pure FE band with bandwidth $4J$. **(b)** With one charge-transfer integral (t_e) nonzero, FE and CT excitons can mix. Both bands have a mixed character and their crossing is avoided. The composition of the bands varies with k. For $t_\mathrm{h} > 0$ and $t_\mathrm{e} = 0$, the picture would be the same. **(c)** Now, both CT integrals are nonzero, which increases the overall mixing and repulsion of the bands. In the shown special case $t_\mathrm{e} = t_\mathrm{h}$, the bands are not mixed at $k = \pi$.

$$
\begin{aligned}
&= u_{\mathrm{FE}j}(k)\vec{p}_\mathrm{FE}\frac{1}{\sqrt{N}}\underbrace{\sum_n \mathrm{e}^{\mathrm{i}kn}}_{\overset{(12)}{=}N\delta_{k,0}} \\
&= u_{\mathrm{FE}j}(k)\delta_{k,0}\sqrt{N}\vec{p}_\mathrm{FE} \qquad (47)
\end{aligned}
$$

Here, we have introduced the transition dipole $\vec{p}_\mathrm{FE}$ of a localized Frenkel exciton basis state:

$$\vec{p}_\mathrm{FE} \equiv \langle n, 0|\hat{\vec{P}}|o\rangle \ . \qquad (48)$$

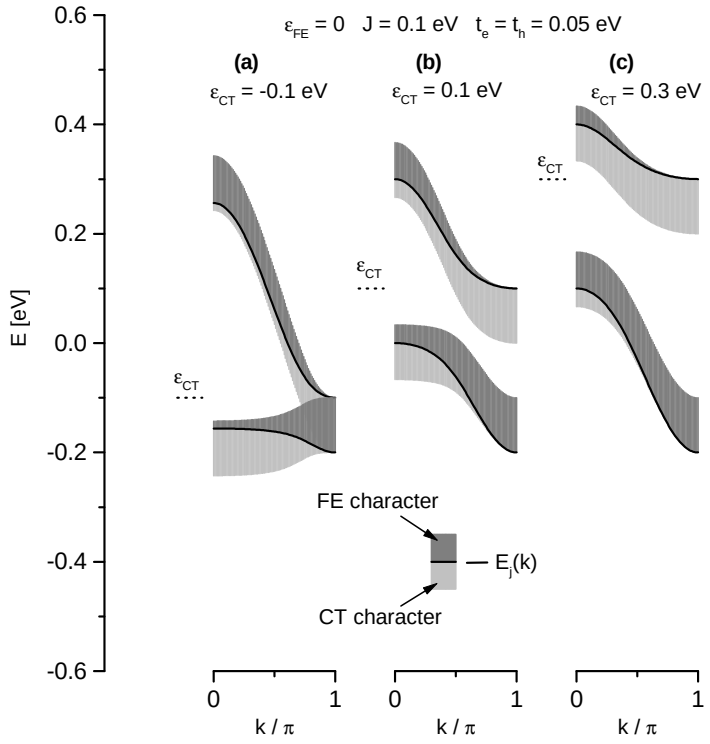

Figure 5:
Exciton bands for varying CT on-site energy ϵ_{CT} and constant ϵ_{FE}, J, $t_{\mathrm{e}} = t_{\mathrm{h}}$. The FE character $F_{\mathrm{FE}j}$ of each band is indicated by the upper stripe, the CT character $F_{\mathrm{CT}j}$ by the lower one (cf. Eqs. (38), (39)). Because of $t_{\mathrm{e}} = t_{\mathrm{h}}$, the FE band and the CT band mix strongly at $k = 0$ but do not mix at $k = \pi$ (cf. Fig. 4). **(a)** With $\epsilon_{\mathrm{CT}} = -0.1\,\mathrm{eV}$, the CT state is energetically well below the FE band at $k = 0$ (cf. Fig. 4a) and strong mixing occurs only for intermediate k. **(b)** With $\epsilon_{\mathrm{CT}} = 0.1\,\mathrm{eV}$, both bands are strongly mixed at $k = 0$. **(c)** With $\epsilon_{\mathrm{CT}} = 0.3\,\mathrm{eV}$, the CT band lies above the pure FE band and both states are weakly mixed.

This local Frenkel exciton transition dipole represents the transition from the ground state of the crystal to a localized Frenkel excitation at any position n. It corresponds to the transition dipole of an isolated molecule, although it is not strictly identical with it due to the formal difference between the localized crystal functions and the wave functions of an isolated molecule.

The CT component in Eq. (46) becomes by means of Eq. (31)

$$\begin{aligned}\vec{P}_{\mathrm{CT}j} &= u_{\mathrm{CT}j}(k)\frac{1}{\sqrt{2}t_k}\Big\{(t_{\mathrm{e}} + t_{\mathrm{h}}\mathrm{e}^{\mathrm{i}k})\langle k,+1|\hat{\vec{P}}|o\rangle \\ &\quad +(t_{\mathrm{e}} + t_{\mathrm{h}}\mathrm{e}^{-\mathrm{i}k})\langle k,-1|\hat{\vec{P}}|o\rangle\Big\}\end{aligned}$$

$$
\begin{aligned}
&= u_{\mathrm{CT}j}(k)\frac{1}{\sqrt{2}t_k}\left\{(t_\mathrm{e}+t_\mathrm{h}\mathrm{e}^{\mathrm{i}k})\frac{1}{\sqrt{N}}\sum_n \mathrm{e}^{\mathrm{i}kn}\underbrace{\langle n,+1|\hat{\vec{P}}|o\rangle}_{=\vec{p}_\mathrm{CT}/\sqrt{2}}\right.\\
&\qquad \left.+(t_\mathrm{e}+t_\mathrm{h}\mathrm{e}^{-\mathrm{i}k})\frac{1}{\sqrt{N}}\sum_n \mathrm{e}^{\mathrm{i}kn}\underbrace{\langle n,-1|\hat{\vec{P}}|o\rangle}_{=\vec{p}_\mathrm{CT}/\sqrt{2}}\right\} \qquad (49)\\
&= u_{\mathrm{CT}j}(k)\delta_{k,0}\sqrt{N}\frac{\vec{p}_\mathrm{CT}}{\sqrt{2}}\underbrace{\frac{1}{\sqrt{2}t_k}\left\{(t_\mathrm{e}+t_\mathrm{h}\mathrm{e}^{\mathrm{i}k})+(t_\mathrm{e}+t_\mathrm{h}\mathrm{e}^{-\mathrm{i}k})\right\}}_{=\sqrt{2}\text{ for }k=0}\\
&= u_{\mathrm{CT}j}(k)\delta_{k,0}\sqrt{N}\vec{p}_\mathrm{CT} \qquad (50)
\end{aligned}
$$

In analogy to Eq. (48), we have used the transition dipole of a localized CT basis state, which will be discussed again in Eq. (71):

$$\vec{p}_\mathrm{CT}/\sqrt{2} \equiv \langle n,+1|\hat{\vec{P}}|o\rangle = \langle n,-1|\hat{\vec{P}}|o\rangle \ . \qquad (51)$$

Both in Eq. (47) for the Frenkel transition dipole and in Eq. (50) for the CT transition dipole, the k selection rule follows mathematically from identity (12). Combination of Eq. (47) and Eq. (50) in Eq. (46) gives the final expression

$$\vec{P}_j = \delta_{k,0}\sqrt{N}\left[u_{\mathrm{FE}j}(k)\vec{p}_\mathrm{FE}+u_{\mathrm{CT}j}(k)\vec{p}_\mathrm{CT}\right] \ . \qquad (52)$$

The oscillator strength f_j of a transition $|o\rangle \rightarrow |\Psi_j\rangle$ with transition dipole $\vec{P}_j$ is defined as

$$f_j = \frac{2mE_j}{e^2\hbar^2}\vec{P}_j^2 \ , \qquad (53)$$

with m being the free electron mass and E_j the transition energy. In simple cases, e.g. for molecules in vacuum, f_j directly determines the peak area in an absorption spectrum.

Typically, the CT transition dipole is very small compared to the Frenkel transition dipole. If we neglect the CT transition dipole, the FE part of the oscillator strength becomes:

$$f_{\mathrm{FE}j} = \frac{2mE_j}{e^2\hbar^2}N\vec{p}_\mathrm{FE}^2 \times F_{\mathrm{FE}j}(0) \ . \qquad (54)$$

In our case, we are always interested in a group of transitions that span an energy region given by the order of magnitude of the interaction parameters and by the variation in the on-site energies. This relevant energy region is typically small compared to the total on-site energies ϵ_FE and ϵ_CT. Furthermore, an arbitrary offset in the on-site energies would only appear as an additive constant in our model Hamiltonians. Therefore, the factor E_j in Eq. (54) can be seen as a mere proportionality constant and the relation simplifies to

$$f_{\mathrm{FE}j} \propto F_{\mathrm{FE}j}(0) \ . \qquad (55)$$

In this way, the Frenkel character introduced in Eq. (38) as the FE contents in the eigenstate obtains an additional meaning: The FE character at $k = 0$ directly gives the FE part of the oscillator strength of the corresponding state. This statement is very obvious for the case of purely electronic states, but it remains valid and becomes more valuable for vibronic states (exciton-phonon mixtures) in Section 3.

If Frenkel and CT basis-states are strongly mixed, both resulting eigenstates can have a significant Frenkel character (see e.g. Figs. 4 and 5). This redistribution of the oscillator strength from the Frenkel state to all eigenstates is depicted by the notion that the CT states borrow oscillator strength from the Frenkel states.

If the CT transition dipole has a significant size, it can contribute to the total transition dipole (52) of the Frenkel-CT mixed eigenstates. Since the coefficients $u_{\mathrm{CT}j}(k)$ vary for the different eigenstates, not only the size but even the direction of the total transition dipole can be different for the different eigenstates. The pure CT contribution to the oscillator strength is proportional to the CT character:

$$f_{\mathrm{CT}j} = \frac{2mE_j}{e^2\hbar^2} N \vec{p}_{\mathrm{CT}}^{\,2} \times F_{\mathrm{CT}j}(0) \; . \tag{56}$$

Typically, this CT contribution cannot be directly observed since it is masked by the much stronger Frenkel contribution. But if $\vec{p}_{\mathrm{CT}} \nparallel \vec{p}_{\mathrm{FE}}$, this CT oscillator strength could be directly probed by light with polarization perpendicular to $\vec{p}_{\mathrm{FE}}$.

As for the Frenkel part, the CT part of the oscillator strength is essentially given by the CT character at $k = 0$:

$$f_{\mathrm{CT}j} \propto F_{\mathrm{CT}j}(0) \; . \tag{57}$$

Because of the proportionality of the oscillator strengths to the corresponding character, the characters are also named spectral weights.

2.4 Direction of charge-transfer transition dipoles

Let us now discuss the small CT transition dipole $\vec{p}_{\mathrm{CT}}$ from Eq. (51) in more detail. For this, we consider as the simplest model system a dimer of two identical closed-shell molecules A and B. Let us assume that the molecules themselves have inversion symmetry and that there is an additional center of inversion between the molecules, which always holds if the dimer corresponds to translationally equivalent nearest-neighbor molecules from a crystal with inversion symmetry. The inversion symmetry is fulfilled in many typical examples of one-component molecular crystals, and it simplifies the situation considerably.

Let us further assume that the electronic structure of the isolated molecules can be represented by just two molecular orbitals, the HOMO (highest occupied molecular orbital) and the LUMO (lowest unoccupied molecular orbital). Thus, we have a one-particle basis set of four monomer orbitals (H_{A}, H_{B}, L_{A}, L_{B}) and we can construct many-particle configurations by distributing the four electrons on these orbitals. Note that this monomer orbital set is not completely orthogonal since $\langle H_{\mathrm{A}}|H_{\mathrm{B}}\rangle$ and $\langle L_{\mathrm{A}}|L_{\mathrm{B}}\rangle$ can be nonzero. We only have

$$\langle H_{\mathrm{A}}|L_{\mathrm{A}}\rangle = \langle H_{\mathrm{B}}|L_{\mathrm{B}}\rangle = 0 \tag{58}$$

since the orbitals from each molecule are orthogonal by definition. Furthermore, from the inversion symmetry and the orthogonality (58), one can show that

$$\langle H_{\rm A}|L_{\rm B}\rangle = \langle H_{\rm B}|L_{\rm A}\rangle = 0\ . \tag{59}$$

From the monomer orbitals $H_{\rm A/B}$, $L_{\rm A/B}$, we can directly construct the following localized basis states:[5]

$$\begin{aligned}
|{\rm ME_A}\rangle &= |H_{\rm A}\to L_{\rm A}\rangle \\
&= \frac{1}{\sqrt{2}}\left\{|L_{\rm A}\bar{H}_{\rm A}H_{\rm B}\bar{H}_{\rm B}\rangle^{(-)} + |H_{\rm A}\bar{L}_{\rm A}H_{\rm B}\bar{H}_{\rm B}\rangle^{(-)}\right\} &(60)\\
|{\rm ME_B}\rangle &= |H_{\rm B}\to L_{\rm B}\rangle \\
&= \frac{1}{\sqrt{2}}\left\{|H_{\rm A}\bar{H}_{\rm A}L_{\rm B}\bar{H}_{\rm B}\rangle^{(-)} + |H_{\rm A}\bar{H}_{\rm A}H_{\rm B}\bar{L}_{\rm B}\rangle^{(-)}\right\} &(61)\\
|{\rm CT_{A\to B}}\rangle &= |H_{\rm A}\to L_{\rm B}\rangle \\
&= \frac{1}{\sqrt{2}}\left\{|L_{\rm B}\bar{H}_{\rm A}H_{\rm B}\bar{H}_{\rm B}\rangle^{(-)} + |H_{\rm A}\bar{L}_{\rm B}H_{\rm B}\bar{H}_{\rm B}\rangle^{(-)}\right\} &(62)\\
|{\rm CT_{B\to A}}\rangle &= |H_{\rm B}\to L_{\rm A}\rangle \\
&= \frac{1}{\sqrt{2}}\left\{|H_{\rm A}\bar{H}_{\rm A}L_{\rm A}\bar{H}_{\rm B}\rangle^{(-)} + |H_{\rm A}\bar{H}_{\rm A}H_{\rm B}\bar{L}_{\rm A}\rangle^{(-)}\right\} &(63)
\end{aligned}$$

The two molecular excitations $|{\rm ME_{A/B}}\rangle$ represent excited states of the isolated molecules. Furthermore, there are two charge-transfer excitations $|{\rm CT_{A\to B}}\rangle$ and $|{\rm CT_{B\to A}}\rangle$, which represent the transfer of an electron to the other molecule. These configurations are depicted in Fig. 6. They are all strictly orthogonal to the ground state, which is obvious for the molecular excitations and which also follows from Eq. (59) for the CT excitations.[6]

However, there is no strict orthogonality between the molecular and the CT excitations, since the scalar products $\langle{\rm ME_A}|{\rm CT_{A\to B}}\rangle$ and $\langle{\rm ME_B}|{\rm CT_{B\to A}}\rangle$ include the overlap $\langle L_{\rm A}|L_{\rm B}\rangle$. This means, the CT states $|{\rm CT_{A\to B}}\rangle$ and $|{\rm CT_{B\to A}}\rangle$ constructed from orbitals of isolated molecules are only approximations for the CT basis states needed in the crystal Hamiltonian $H_{\rm NN}$ in Eqs. (29). For a strict microscopic description of the CT crystal basis states, a further orthogonalization of either the molecular orbitals (leading to Wannier orbitals) or of the localized many-electron configurations would be necessary.

For a qualitative discussion of the CT transition dipole, we will now ignore the difference between the true orthogonal crystal basis and the localized basis states derived from monomer orbitals. Then, the transition dipole of the CT state $\vec{p}_{\rm B\to A} = \langle{\rm CT_{B\to A}}|\hat{\vec{P}}|o\rangle$ can be related to the molecular monomer orbitals. This problem was already discussed in detail by Mulliken [43],

[5] We use a quantum chemical notation for spin orbitals as e.g. in Ref. [42].

[6] In order to calculate the overlap ${}^{(-)}\langle H_{\rm A}\bar{H}_{\rm A}H_{\rm B}\bar{H}_{\rm B}|{\rm CT_{A\to B}}\rangle$ of the localized CT state with the ground state, one has to represent the CT state in an orthogonal orbital basis, since for the nonorthogonal basis $H_{\rm A,B}, L_{\rm A,B}$ the standard rules for Slater determinants cannot be applied. A suitable orthogonalized orbital basis is given by symmetric and antisymmetric linear combinations of the monomer orbitals.

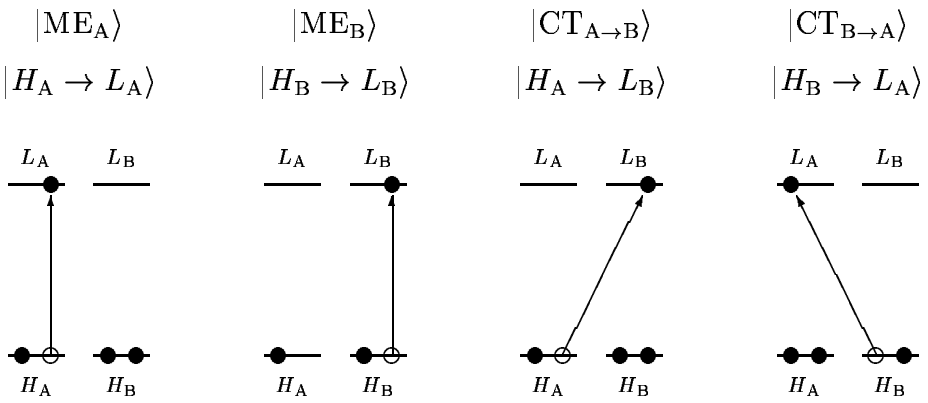

Figure 6:
Scheme of the localized configurations for an idealized dimer with four monomer orbitals. All configurations represent excited singlet states and therefore no spin is indicated for the electrons.

and we can use his expression[7]

$$\vec{p}_{\mathrm{B}\to\mathrm{A}} = -e\langle L_\mathrm{A}|\vec{r}|H_B\rangle \ . \tag{64}$$

Thus far, this result is very intuitive: The CT transition dipole is given as the dipole moment of the transition density

$$\varrho_{\mathrm{AB}}(\vec{r}) = L_\mathrm{A}(\vec{r})H_\mathrm{B}(\vec{r}) \tag{65}$$

by

$$\vec{p}_{\mathrm{B}\to\mathrm{A}} = -e\int d^3r\ \vec{r}\times\varrho_{\mathrm{AB}}(\vec{r}) \ . \tag{66}$$

The structure of the transition density cloud $\varrho_{\mathrm{AB}}(\vec{r})$, however, cannot be easily predicted for complicated molecules.

Mulliken and Person ([44], pp. 23ff) give a qualitative discussion for the case of a σ-type overlap between atomic orbitals. In this case, the transition density forms a small cloud without nodes and is localized between the two molecules. Then, $\int d^3r\ \vec{r}\varrho_{\mathrm{AB}}$ can be approximated by

$$\int d^3r\ \vec{r}\varrho_{\mathrm{AB}} \approx \vec{R}_{\mathrm{AB}}\int d^3r\ \varrho_{\mathrm{AB}} = \vec{R}_{\mathrm{AB}}S_{\mathrm{AB}} \ , \tag{67}$$

where S_{AB} is the overlap $\langle L_\mathrm{A}|H_\mathrm{B}\rangle$ and $\vec{R}_{\mathrm{AB}}$ is the average position of the transition density cloud. Based on this approximation, the CT transition dipole in a donor-acceptor complex is

[7] Mulliken actually considered a dimer of an electron donor B and a chemically different acceptor A, without inversion symmetry. Then, Eq. (59) does not hold and Mulliken had to consider the mixing with the ground state as well as terms arising from the overlap $\langle L_\mathrm{A}|H_\mathrm{B}\rangle$. Eq. (64) is accordingly a simplified version for his expression for μ_{01}.

derived as[8]

$$\vec{p}_{\mathrm{B}\to\mathrm{A}} = -e\sqrt{2}\frac{S_{\mathrm{AB}}}{\sqrt{1+S_{\mathrm{AB}}^2}}(\vec{R}_{\mathrm{AB}} - \vec{R}_{\mathrm{B}}) \,. \tag{68}$$

This result is very intuitive: The CT transition dipole can be visualized as the transfer of an electron from the donor (position $\vec{R}_{\mathrm{B}}$) to the overlap region between donor and acceptor (position $\vec{R}_{\mathrm{AB}}$). The direction of $\vec{p}_{\mathrm{B}\to\mathrm{A}}$ is along the connection line between donor and acceptor.

We want to emphasize that this intuitive picture completely breaks down in our case of a dimer with inversion symmetry. All effects included in Eq. (68) result from the nonzero overlap S_{AB} between the donor HOMO and the acceptor LUMO, and they vanish for the symmetric dimer. The next nonzero term (Eq. (66)) in the symmetric dimer results not from the average position $\vec{R}_{\mathrm{AB}}$ of the transition density cloud $\varrho_{\mathrm{AB}}(\vec{r})$ but from its internal structure.

As another consequence of the inversion symmetry, the true eigenstates within the CT manifold will also obey the symmetry. These symmetry adapted CT states are:

$$|\mathrm{CT}_{\pm}\rangle \equiv \frac{|\mathrm{CT}_{\mathrm{A}\to\mathrm{B}}\rangle \pm |\mathrm{CT}_{\mathrm{B}\to\mathrm{A}}\rangle}{\sqrt{2}} \,. \tag{69}$$

The transition dipoles of these symmetry-adapted CT states are

$$\vec{p}_{\mathrm{CT}\pm} = \frac{\vec{p}_{\mathrm{B}\to\mathrm{A}} \pm \vec{p}_{\mathrm{A}\to\mathrm{B}}}{\sqrt{2}} \,. \tag{70}$$

The two CT-transition dipoles $\vec{p}_{\mathrm{B}\to\mathrm{A}}$ and $\vec{p}_{\mathrm{A}\to\mathrm{B}}$ in Eq. (70) are equal because of the inversion symmetry, which can also be seen from Eq. (64):

$$\vec{p}_{\mathrm{B}\to\mathrm{A}} = \vec{p}_{\mathrm{A}\to\mathrm{B}} \equiv \vec{p}_{\mathrm{CT}}/\sqrt{2} \,. \tag{71}$$

Thus, Eq. (70) becomes:

$$\vec{p}_{\mathrm{CT}+} = \vec{p}_{\mathrm{CT}} \tag{72}$$

$$\vec{p}_{\mathrm{CT}-} = 0 \,. \tag{73}$$

In the case of coplanar stacked aromatic molecules, the structure of the transition density cloud cannot be easily approximated. ϱ_{AB} is formed by two complicated π orbitals, which overlap in the region between the molecules. There it forms a flat, quasi-two dimensional cloud with dimensions of the molecular size. Furthermore, like the contributing monomer orbitals, it has a complicated nodal structure with lobes of alternating sign. Therefore, it can be expected that the transition dipole $\vec{p}_{\mathrm{B}\to\mathrm{A}}$ will lie approximately in the plane of this quasi-two dimensional transition density cloud, i.e. parallel to the molecular planes. If there are no additional symmetries, the actual direction cannot be estimated. As an illustration, we show the monomer orbitals L_{A} and H_{B} and the resulting transition density for a MePTCDI dimer in Fig. 7. There, it is clearly visible how the transition density is formed in the plane between the molecules. In conclusion, the direction the CT transition dipole and the underlying leading terms are very different for a symmetric dimer compared to the classical donor-acceptor complexes studied by Mulliken [43].

[8] See [43], Eqs. (18) and(19). We give only the leading term for strong CT character of the excited state.

a) $L_{\mathrm{A}}(\vec{r})$

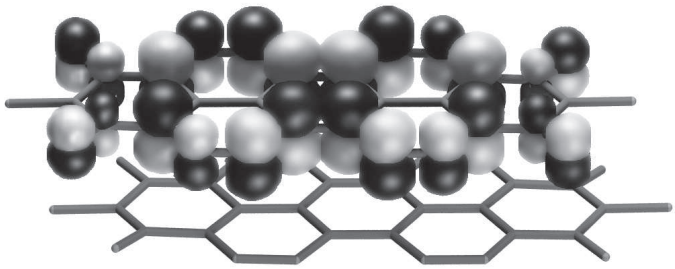

b) $H_{\mathrm{B}}(\vec{r})$

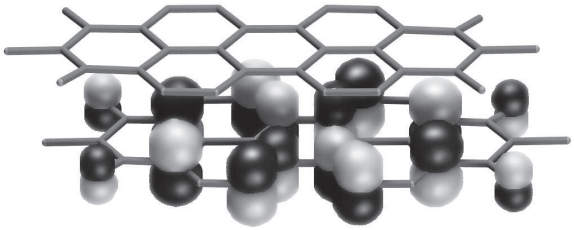

c) $\varrho_{\mathrm{AB}}(\vec{r})$

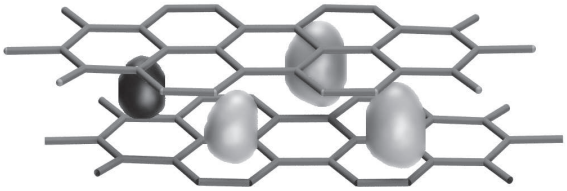

Figure 7:
Formation of the transition density cloud in a dimer of MePTCDI molecules. a) LUMO L_{A}. b) HOMO H_{B}. c) Illustration of the transition density $\varrho_{\mathrm{AB}} = H_{\mathrm{B}}(\vec{r}) \times L_{\mathrm{A}}(\vec{r})$. The molecular structure corresponds to nearest-neighbors along the stacking direction (a-axis) from the experimental crystal structure [85], see Figure 2. The molecular orbitals were calculated with the ZINDO/S method as implemented by HyperChem [107], the transition density was calculated from these orbitals. Its precise structure is not very accurate since the orthogonality relations are not exact in the ZINDO/S scheme, but the location between the molecules can be illustrated. Calculations and pictures by K. Schmidt.

3 Strong coupling of the electronic excitations with internal phonon modes

3.1 Exciton-phonon coupling in the isolated molecule

In Section 2, we have considered exciton states in a rigid lattice, which is a purely electronic problem. Now, we want to include exciton-phonon coupling, i.e. coupling of the electronic states to lattice vibrations. In this work, we consider only one type of exciton-phonon coupling, namely coupling to internal phonon modes (vibrations along intramolecular nuclear coordinates). These vibrations occur already in the isolated molecule, and their effect is usually demonstrated by a Franck-Condon picture as in Fig. 8. If the exciton-phonon coupling constant (see below) is in the order of one, the internal exciton-phonon coupling leads to a pronounced "vibronic progression" in the absorption and emission spectra of the isolated molecules. Such a progression is very conspicuous in the monomer spectra of our model compounds MePTCDI and PTCDA, as can be seen in Fig. 3a. In this section, we summarize the notation for exciton-phonon coupling in the isolated molecule, and in Sections 3.2-3.8 we deal with exciton-phonon coupling in one-dimensional systems.

Let us for simplicity assume that the isolated molecule has just one nuclear coordinate q. In Born-Oppenheimer approximation, the molecular wave functions can be split into an electronic and a vibrational part:

$$\psi_{f\nu}(\vec{\mathbf{r}}, q) = \varphi_f(\vec{\mathbf{r}}, q) \times \chi_{f\nu}(q) \ , \tag{74}$$

where f numbers the electronic and ν the vibrational levels. $\varphi_f(\vec{\mathbf{r}}, q)$ is the electronic wave function, which depends explicitly on all electron coordinates $\vec{\mathbf{r}}$ and parametrically on the nuclear coordinate q. $\chi_{f\nu}(q)$ are the vibrational wave functions in the electronic state f and vibrational level ν. They depend only on the nuclear coordinate q. In Born-Oppenheimer approximation, the Schrödinger equation for the molecule separates into an electronic problem at a fixed nuclear coordinate q and a vibrational problem for the nuclear coordinate q.

From the electronic problem, the total energy of the molecule in electronic state f is given as a function $V_f(q)$ of the nuclear coordinate. Therefore, the vibrational Hamiltonian in state f becomes:

$$H_f^{\text{vib}} = -\frac{\hbar^2}{2M_{\text{eff}}}\nabla^2 + V_f(q) \ . \tag{75}$$

For small elongations from the equilibrium position, the vibrational potential becomes a harmonic potential

$$V_f(q) = \frac{1}{2}M_{\text{eff}}\omega_f^2(q - q_{0f})^2 + v_f \ , \tag{76}$$

with effective mass M_{eff}, angular frequency ω_f and a total energy offset v_f.

Since the potential $V_1(q)$ in the excited state depends on all electrons but only a few electrons take part in the excitation, the curvature of $V_1(q)$ differs not strongly from that of the potential $V_0(q)$ in the ground-state. Hence, the vibronic spacing is very similar. For example, in the case of MePTCDI in chloroform, the difference of $\hbar\omega$ derived from the absorption and emission spectra amounts to 3 meV compared to $\hbar\omega = 170$ meV (values from Fig. 3). We therefore make

the further approximation that the vibrational spacings $\hbar\omega_f$ are identical for the ground and excited state.

As an abbreviation, we introduce the dimensionless nuclear coordinate[9]

$$\lambda \equiv \sqrt{\frac{M_{\text{eff}}\omega}{2\hbar}}\,(q - q_{00})\,, \tag{77}$$

which is centered around the equilibrium position q_{00} of the electronic ground state $f = 0$. Now, the vibrational potentials are in the electronic ground state

$$V_0(\lambda) = \hbar\omega\lambda^2 + v_0 \tag{78}$$

and in the excited state

$$V_1(\lambda) = \hbar\omega(\lambda - g)^2 + v_1\,. \tag{79}$$

The exciton-phonon coupling constant g introduced here is the displacement of the exited state potential V_1 with respect to the ground state potential V_0 along the dimensionless coordinate λ. Both potentials are illustrated in Fig. 8. If one introduces the vertical excitation energy

$$E_{\text{vert}} \equiv V_1(0) - V_0(0) \tag{80}$$

for the excitation energy in a rigid molecule ($\lambda \stackrel{!}{=} 0$), the excited state potential can be written as

$$V_1(\lambda) = \hbar\omega(\lambda - g)^2 + v_0 + E_{\text{vert}} - E_{\text{FC}}\,. \tag{81}$$

Here, the vibrational reorganization energy (Franck-Condon energy) E_{FC} gives the energy gain for the geometry relaxation of the electronically excited molecule after a "vertical excitation" into the new equilibrium geometry. The reorganization energy is trivially connected with the exciton-phonon coupling constant by

$$E_{\text{FC}} = \hbar\omega g^2\,. \tag{82}$$

Optical absorption corresponds to the transitions $|\psi_{00}\rangle \rightarrow |\psi_{1\nu}\rangle$, since for $\hbar\omega = 0.17\,\text{eV} \gg kT$ only the lowest vibrational level of the electronic ground state is occupied. The transition dipole moment is given by the matrix element with the dipole moment operator $\hat{\vec{P}}$:

$$\vec{p}^{\,\nu} = \langle\psi_{1\nu}|\hat{\vec{P}}|\psi_{00}\rangle \tag{83}$$

This matrix element refers to integration over all electron and nucleus coordinates. In the product representation (74), the vibrational part $\chi_{f\nu}$ only depends on the nucleus coordinates, whereas the electronic part φ_f contains these nucleus coordinates as a variable that varies slowly

[9] In the literature, several ways are common to introduce dimensionless coordinates and exciton-phonon coupling constants.

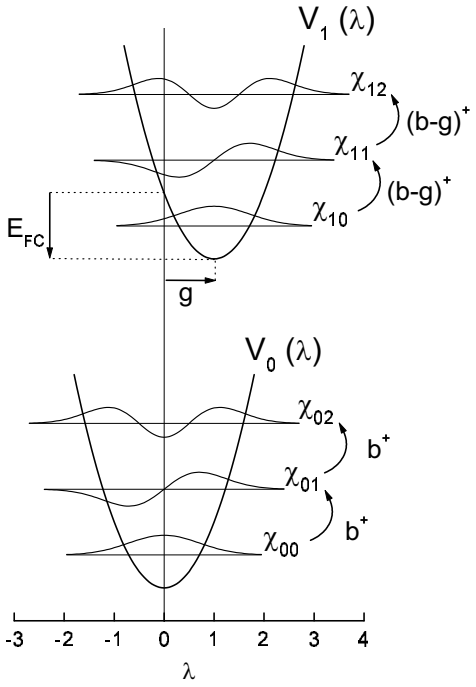

Figure 8:
Schematic energy diagram for the vibrational potentials of ground (V_0) and excited (V_1) state along the dimensionless coordinate λ. The excited-state potential is displaced on the λ-axis by the exciton-phonon coupling constant g, which corresponds to a vibrational reorganization energy $E_{\mathrm{FC}} = \hbar\omega g^2$. The vibrational wave functions $\chi_{f\nu}(\lambda)$ are shown for the lowest three levels. The operators $b^\dagger$ create phonons in the ground state potential, the displaced operators $(b-g)^\dagger$ create phonons in the excited state potential.

compared to the electron coordinates. Therefore, the integration can be split into an electronic and a vibrational matrix element (e.g. [45], p. 305):

$$\vec{p}^{\,\nu} = \underbrace{\langle\varphi_1|\hat{\vec{P}}|\varphi_0\rangle}_{\vec{p}_{\mathrm{FE}}} \times \underbrace{\langle\chi_{1\nu}|\chi_{00}\rangle}_{S(\,{}^{\nu}_{0}\,)} \tag{84}$$

Here, we have introduced the electronic transition dipole moment of the lowest molecular excitation $\vec{p}_{\mathrm{FE}}$ and the vibronic overlap factors $S(\,{}^{\nu}_{0}\,)$. The oscillator strength f for a transition with energy E is defined as $f = 2mE|\vec{p}|^2/(e^2\hbar^2)$ (cf. Eq. (53)), where $\vec{p}$ is the transition dipole moment. Thus, the oscillator strength (corresponding to the absorption peak area) of the ν-th transition is

$$f_\nu = \frac{2m_{\mathrm{e}}}{e^2\hbar^2} \cdot E^\nu |\vec{p}_{\mathrm{FE}}|^2 \times S^2(\,{}^{\nu}_{0}\,) \,. \tag{85}$$

The squared values $S^2(\begin{smallmatrix}\nu\\0\end{smallmatrix})$ are called the Franck-Condon factors. They determine the intensity distribution in the vibronic progression. In the considered case of a single vibrational coordinate λ and two harmonic potentials displaced by g, the Franck-Condon factors can be analytically expressed as (e.g. [46]):

$$S^2(\begin{smallmatrix}\nu\\0\end{smallmatrix}) = |\langle\chi_{1\nu}|\chi_{00}\rangle|^2 = \frac{g^{2\nu}}{\nu!}\mathrm{e}^{-g^2} \tag{86}$$

For large coupling constants g, the maximum intensity occurs at high vibrational levels, whereas for $g = 0$ exclusively the lowest vibrational level is excited ($f_\nu = \delta_{0\nu}$). For a coupling constant of $g = 1$, which is visualized in Fig. 8 and represents the order of magnitude in PTCDA-derivatives, the lowest and second lowest vibrational level obtain approximately the same oscillator strengths ($f_1 \approx f_0$). This leads to the characteristic spectrum in Fig. 3a, where the areas of the 0-0 peak and of the 0-1 peak are on the same order of magnitude.

In order to extend the molecular vibrational Hamiltonian (75) to an aggregate Hamiltonian, the introduction of phonon creation and annihilation operators is very helpful:[10]

$$b^\dagger \equiv \lambda - \frac{1}{2}\frac{\partial}{\partial\lambda}\,, \tag{87}$$

$$b \equiv \lambda + \frac{1}{2}\frac{\partial}{\partial\lambda}\,. \tag{88}$$

Then, the vibrational Hamiltonian in the electronic ground state becomes:

$$H_0^{\mathrm{vib}} = \hbar\omega\left(b^\dagger b + \frac{1}{2}\right) + v_0\,. \tag{89}$$

For the vibrational Hamiltonian in the excited state, it is more convenient to introduce displaced operators because of the potential displacement in Eq. (81):

$$\tilde{b}^\dagger \equiv b^\dagger - g\,, \tag{90}$$

$$\tilde{b} \equiv b - g\,. \tag{91}$$

Then, from comparison with Eq. (89), the Hamiltonian in the excited state can be written as

$$H_1^{\mathrm{vib}} = \hbar\omega\left(\tilde{b}^\dagger\tilde{b} + \frac{1}{2}\right) + v_0 + E_{\mathrm{vert}} - E_{\mathrm{FC}}\,. \tag{92}$$

After inserting relations (90), (91) and (82) for E_{FC}, we can express the excited state Hamiltonian with the undisplaced operators $b^\dagger$, b:

$$H_1^{\mathrm{vib}} = \hbar\omega\left(b^\dagger b - g(b^\dagger + b) + \frac{1}{2}\right) + v_0 + E_{\mathrm{vert}}\,. \tag{93}$$

[10] A good summary can be found in Ref. [47], pp. 248-252; a comprehensive introduction is given e.g. in Ref. [48].

Now, it is possible to combine the vibrational Hamiltonians for the ground and excited state by introducing electronic operators. For this, we assume that the electronic problem is a strict two-level problem with the electronic ground state $|\phi_0\rangle$ and the exited state $|\phi_1\rangle$. We define electronic operators $a^\dagger$ and a by

$$\begin{array}{rclrcl} a^\dagger|\phi_0\rangle & \equiv & |\phi_1\rangle & a|\phi_0\rangle & \equiv & 0 \\ a^\dagger|\phi_1\rangle & \equiv & 0 & a|\phi_1\rangle & \equiv & |\phi_0\rangle\,. \end{array} \tag{94}$$

That means, $a^\dagger$ creates an exciton at the molecule, a destroys it and $a^\dagger a$ is the exciton number operator.

Now, both operators $H_0^{\rm vib}$ and $H_1^{\rm vib}$ can be combined by multiplying the additional terms in $H_1^{\rm vib}$ with $a^\dagger a$. We obtain the monomer Hamiltonian

$$H_{\rm mono} = \hbar\omega\left(b^\dagger b + \frac{1}{2}\right) + v_0 + a^\dagger a \times \left(-\hbar\omega g(b^\dagger + b) + E_{\rm vert}\right)\,. \tag{95}$$

Here, the first term is the familiar Hamiltonian of the harmonic oscillator, which describes the internal phonons in the molecule. The constant offset v_0 for the total ground state energy of the molecule is not relevant here. $a^\dagger a$ is zero for the electronic ground state but one for the excited state. In the excited state, the linear exciton-phonon coupling $-\hbar\omega g(b^\dagger + b)$ and the vertical excitation energy $E_{\rm vert}$ are added. The exciton-phonon coupling, which is the most interesting term, entirely results from the displacement of the exited state vibrational potential.

3.2 The Holstein-Hamiltonian for exciton-phonon coupling

Now, we can extend the monomer Hamiltonian (95) to a one-dimensional chain. In the first step, we neglect intermolecular interactions and formally add the monomer Hamiltonians $H_{\rm mono}(n)$ of the molecules, which are numbered by the index $n = 1\ \ldots N$.

$$\begin{aligned} \sum_n H_{\rm mono}(n) &= \sum_n \Bigg[\hbar\omega\left(b_n^\dagger b_n + \frac{1}{2}\right) + v_0 \\ &\qquad + a_n^\dagger a_n\left(-\hbar\omega g(b_n^\dagger + b_n) + E_{\rm vert}\right)\Bigg]\,. \end{aligned} \tag{96}$$

We are exclusively interested in the one-exciton subspace of this problem ($\sum_n a_n^\dagger a_n = 1$). The energy of the lowest state in this one-exciton subspace is given by the lowest vibrational level of $N-1$ molecules in the electronic ground state and the lowest vibrational level of one molecule in the excited state:

$$\begin{aligned} & (N-1)\times\left[\hbar\omega\left(0+\frac{1}{2}\right)+v_0\right] + \left[\hbar\omega\left(0+\frac{1}{2}\right)+v_0+E_{\rm vert}-E_{\rm FC}\right] \\ = \;& N\times\left[\frac{1}{2}\hbar\omega + v_0\right] + E_{\rm vert} - E_{\rm FC} \end{aligned}$$

We want to use this state as the reference state and set the zero of the energy axis to its energy. Then, the Hamiltonian (96) in the non-interacting case becomes (with using $E_{\rm FC} = g^2\hbar\omega$)

$$H_{\rm non-inter} = H^{\rm ph} + H^{\rm FE-ph}\,, \tag{97}$$

with the phonon part

$$H^{\mathrm{ph}} = \hbar\omega \sum_n b_n^\dagger b_n \tag{98}$$

and the (Frenkel) exciton-phonon coupling part

$$H^{\mathrm{FE-ph}} = \hbar\omega \sum_n a_n^\dagger a_n \left(-g(b_n^\dagger + b_n) + g^2 \right) \ . \tag{99}$$

We call this non-interacting case the molecular limit.

Now, we add to the non-interaction Hamiltonian (97) one of the simplest electronic interaction terms, namely a nearest-neighbor Frenkel exciton hopping $H_{\mathrm{elec}}^{\mathrm{FE}}$ as introduced in Eq. (16):

$$H_{\mathrm{elec}}^{\mathrm{FE}} = J \sum_n (a_n^\dagger a_{n+1} + a_{n+1}^\dagger a_n) \ , \tag{100}$$

where J is the Frenkel exciton transfer integral. With this term, we obtain the classical Holstein Hamiltonian

$$H_{\mathrm{Hol}}^{\mathrm{FE}} = H_{\mathrm{elec}}^{\mathrm{FE}} + H^{\mathrm{ph}} + H^{\mathrm{FE-ph}} \ . \tag{101}$$

This Hamiltonian is one of the simplest model systems for exciton-phonon coupling. $H_{\mathrm{elec}}^{\mathrm{FE}}$ is a purely electronic operator for Frenkel-exciton hopping, H^{ph} is a purely vibrational operator for internal phonons and $H^{\mathrm{FE-ph}}$ is a linear coupling term, which couples excitons and phonons locally (i.e., if they occupy the same molecule).

The Hamiltonian (101) is commonly called Holstein Hamiltonian because of two fundamental works [49, 50] by Holstein on transport properties in this model system. The ground state of this Hamiltonian describes the states of free charge carriers or excitons that are responsible for electric conduction or exciton diffusion. Therefore, the ground state has been extensively studied by approximate analytical methods (reviews e.g. in Refs. [51, 52, 5, 53, 54]). Currently, much effort is also spent in obtaining numerical solutions for the full parameter range by variational approaches [55, 56, 57, 58, 59, 60, 61], direct diagonalization [62, 63, 64, 65, 66], quantum Monte-Carlo calculations [67, 68, 69, 70], and density-matrix renormalization-group techniques [71]. Compared to this, the properties of higher states have been much less investigated. These excited vibronic states, however, are essential for an understanding of optical absorption spectra. The relevant issues were identified in the initial studies of molecular crystals and limiting cases were analyzed (see e.g. [3, 72]). For intermediate cases, however, only a few quantitative studies have been published. These include direct diagonalization studies of dimers [73, 15], variational and direct-diagonalization studies of aggregates [74, 75, 76, 77, 78], and a discussion of the second lowest vibronic state in an infinite chain [66]. Here, we will present the numerical approach described in Ref. [41], which was specifically developed in the context of our work on PTCDA-related quasi-one-dimensional crystals.

3.3 Basis functions for numerical diagonalization

Our aim is to find the low energy eigenstates of the Holstein Hamiltonian (101) within the one-exciton manifold. For this, we use a numerical approach based on direct diagonalization.

At first, we define a set of basis functions for the Hilbert space on which the Hamiltonian acts. The basis functions should be close to the final solution. Then, already a small and finite subset of functions can reasonably represent the solution.

In our case, we obtain the basis functions from the reference system given by the non-interacting case ($J = 0$, molecular limit). In a localized picture, the eigenstates in the molecular limit are simple product functions of molecular vibronic states. One exciton is localized at site n is and the vibrational wave functions at this site are given by oscillator functions in the displaced potential V_1. At all other sites, which we count relative to the position of the exciton, the vibrational wave functions are oscillator functions in the ground state potential V_0. These localized eigenstates can be used as basis functions for representing the solution of the complete Hamiltonian.

Thus, the basis functions can be written as

$$\begin{aligned} |n\underline{\nu}\rangle &\equiv |n\rangle \times |\ldots \nu_{-1}\tilde{\nu}_0\nu_1\ldots\rangle \\ &\equiv a_n^\dagger|o_{\mathrm{el}}\rangle \times \tilde{B}_{n\underline{\nu}}^\dagger|o_{\mathrm{vib}}\rangle\ . \end{aligned} \tag{102}$$

Here, the first factor describes the electronic part of a localized Frenkel exciton at site n. The second factor describes the vibrational wave function of the chain. It is created by the action of the vibrational operator $\tilde{B}_{n\underline{\nu}}^\dagger$ on the vibrational ground state:

$$\tilde{B}_{n\underline{\nu}}^\dagger = \underbrace{\frac{1}{\sqrt{\nu_0!}}(\tilde{b}_n^\dagger)^{\nu_0}\cdot \mathrm{e}^{-\frac{g^2}{2}}\mathrm{e}^{gb_n^\dagger}}_{\text{displaced on } n} \times \underbrace{\prod_{m\neq 0}\frac{1}{\sqrt{\nu_m!}}(b_{n+m}^\dagger)^{\nu_m}}_{\text{undisplaced otherwise}}\ . \tag{103}$$

Here, the first factor ("displaced") describes internal phonons in the displaced potential at the site n of the exciton, where the factor $\mathrm{e}^{-\frac{g^2}{2}}\mathrm{e}^{gb_n^\dagger}$ transforms the undisplaced vibrational ground state $|o_n\rangle$ into the displaced ground state $|\tilde{o}_n\rangle$ (e.g. [47, p. 249]). The second factor ("undisplaced") describes internal phonons at all sites different from n in the undisplaced potential.

The phonon cloud state $|\underline{\nu}\rangle$ contains the phonon occupation numbers ν_m around the exciton for all lattice sites. In the long notation $|\ldots\nu_{-1}\tilde{\nu}_0\nu_1\ldots\rangle$, the special position of the exciton ($m = 0$) is denoted by the tilde. A complete phonon-cloud basis for a chain of N molecules consists of N-boson states and leads to huge basis sets even for small occupation numbers. But a far smaller basis is sufficient to calculate the absorption spectrum.

In the molecular limit, optical absorption from the electronic and vibrational ground state only creates phonons at the site of the electronic excitation, i.e. only phonon clouds of the form $|\ldots 00\tilde{\nu}_0 00\ldots\rangle$. We call such clouds *joint configurations*. In contrast, excited states with any $\nu_m \neq 0$ for $m \neq 0$ cannot be reached optically. We call these clouds *separated configurations*, since there is at least one phonon excitation separated from the exciton position. An example of a joint and of a separated configuration is illustrated in Fig. 9 and Fig. 10, respectively. In the molecular limit, the absorption spectrum can be explained by considering exclusively the joint configurations since the separated configurations would not mix with the joint ones and they have no transition dipole moment with the ground state on their own.

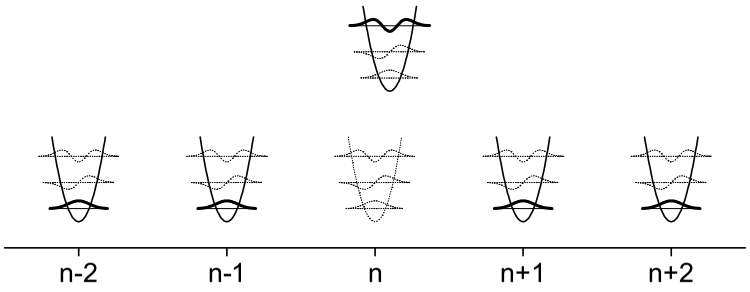

Figure 9:
Illustration of a joint configuration (here: $|\nu\rangle = |\ldots 00\tilde{2}00\ldots\rangle$).

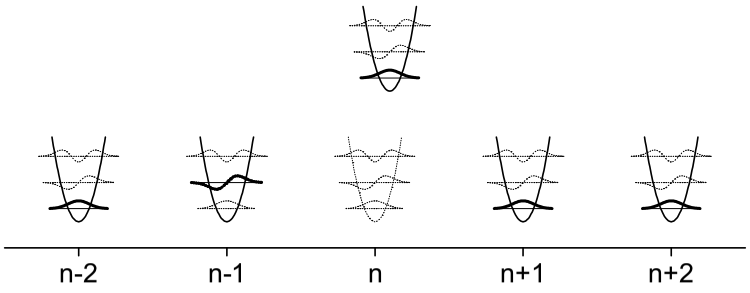

Figure 10:
Illustration of a separated configuration (here: $|\nu\rangle = |\ldots 01\tilde{0}00\ldots\rangle$).

For $|J| > 0$, the separated configurations can mix with the joint configurations. That means, optical absorption creates a state in which phonons are excited at arbitrary distance from the exciton site. However, the contribution of separated configurations decreases with increasing exciton-phonon separation. Thus, the photo-excited exciton will be surrounded by a *localized* phonon cloud. The localized nature of phonon clouds is the motivation for our choice of basis functions. Instead of N-dimensional cloud states $|\underline{\nu}\rangle$, a finite range $|\nu_{-M}\ldots\tilde{\nu}_0\ldots\nu_M\rangle$, with M denoting the extension of the phonon cloud, will be sufficient. Numerically, M can be increased until convergence is reached. Important qualitative insight can already be obtained from the inclusion of just nearest-neighbor phonon clouds ($M = 1$).

The choice of the displaced basis functions in Eq. (102) corresponds to applying the polaron canonical transformation (Lang-Firsov transformation) to a set of basis functions, in which all vibrational functions (including the site n of the exciton) are oscillator functions in the ground state potential ([79] or see also e.g. [5], p. 98, [53], p. 25).

With the restriction to local phonon clouds around the exciton, we Fourier transform the

basis states (102):

$$|k\underline{\nu}\rangle \equiv \frac{1}{\sqrt{N}} \sum_n \mathrm{e}^{\mathrm{i}kn} |n\underline{\nu}\rangle \; . \tag{104}$$

These states represent an exciton "dressed" with a local phonon cloud. The index k gives the quasi-momentum of the whole object, i.e. the dressed exciton, and k is a good quantum number due to translational symmetry. Thus, for any given k the basis set consists only of a set of phonon cloud configurations. We emphasize that in contrast to the real-space basis (102), the momentum-space basis functions (104) are not Born-Oppenheimer separable into a product of a purely electronic and a purely vibrational part.

Having specified the basis states, the Hamiltonian can be represented as a matrix. Application of $H_{\mathrm{Hol}}^{\mathrm{FE}}$ to the real space states from (102) yields the matrix elements:

$$\begin{aligned} \langle m\underline{\mu}|H_{\mathrm{Hol}}^{\mathrm{FE}}|n\underline{\nu}\rangle &= \delta_{m,n}\langle\underline{\mu}|\underline{\nu}\rangle \cdot \sum_i \nu_i \\ &+ J\left[\delta_{m,n-1}\mathcal{F}_{-1}\left(\frac{\underline{\mu}}{\underline{\nu}}\right) + \delta_{m,n+1}\mathcal{F}_{+1}\left(\frac{\underline{\mu}}{\underline{\nu}}\right)\right] . \end{aligned} \tag{105}$$

The first term in this compact notation results from the operators H^{ph} and $H^{\mathrm{FE-ph}}$. They contain no interactions between different sites and thus simply count the phonons in the Lang-Firsov basis. The overlap factor $\langle\underline{\mu}|\underline{\nu}\rangle$ stands for the total overlap of two phonon clouds centered at the same lattice site. It is nonzero only for identical clouds due to the orthogonality of the oscillator functions:

$$\langle\underline{\mu}|\underline{\nu}\rangle = \prod_i \delta_{\mu_i,\nu_i} \; . \tag{106}$$

The second term in Eq. (105) results from the purely electronic Frenkel transfer process $H_{\mathrm{elec}}^{\mathrm{FE}}$. The vibrational part of the basis functions factors out and leads to the Franck-Condon overlaps $\mathcal{F}_{\pm 1}$ for the total vibronic overlap of the phonon cloud $\underline{\nu}$ centered at n and the phonon cloud $\underline{\mu}$ centered at $m = n \pm 1$:

$$\mathcal{F}_{-1} = S\binom{\mu_0}{\nu_{-1}} \cdot S\binom{\nu_0}{\mu_{+1}} \cdot \prod_{i\neq 0,1} \langle\mu_i|\nu_{i-1}\rangle \tag{107}$$

$$\mathcal{F}_{+1} = S\binom{\nu_0}{\mu_{-1}} \cdot S\binom{\mu_0}{\nu_{+1}} \cdot \prod_{i\neq -1,0} \langle\mu_i|\nu_{i+1}\rangle \; . \tag{108}$$

Here, $S\binom{\nu}{\mu}$ is the overlap between a displaced oscillator function with quantum number ν and an undisplaced function with quantum number μ [80]

$$\begin{aligned} S\binom{\nu}{\mu} &\equiv \langle \frac{1}{\sqrt{\mu!}}(b^\dagger)^\mu \; o \mid \frac{1}{\sqrt{\nu!}}(\tilde{b}^\dagger)^\nu \; \tilde{o}\rangle \\ &= \frac{\mathrm{e}^{\frac{-g^2}{2}}}{\sqrt{\mu!\nu!}} \sum_{i=0}^{\min(\mu,\nu)} \frac{(-1)^{\nu-i} g^{\mu+\nu-2i} \mu!\nu!}{i!(\mu-i)!(\nu-i)!} \; . \end{aligned} \tag{109}$$

It is obvious that in the Lang-Firsov basis the strength g of the exciton-phonon coupling enters only through the magnitude of the factors $\mathcal{F}_{\pm 1}$ in the inter-site hopping term.

In the momentum space representation (104), the Hamiltonian matrix becomes

$$\begin{aligned}\langle k\underline{\mu}|H_{\mathrm{Hol}}^{\mathrm{FE}}|k\underline{\nu}\rangle = \langle\underline{\mu}|\underline{\nu}\rangle\hbar\omega\sum_i \nu_i \\ + J\left[\mathrm{e}^{-\mathrm{i}k}\mathcal{F}_{-1}\left(\frac{\underline{\mu}}{\underline{\nu}}\right) + \mathrm{e}^{+\mathrm{i}k}\mathcal{F}_{+1}\left(\frac{\underline{\mu}}{\underline{\nu}}\right)\right].\end{aligned} \tag{110}$$

For general momenta k, these matrix elements are complex numbers. For our intended application to spectroscopy, the values at the Brillouin-zone edges ($k = 0, \pi$) are of interest, and there the matrix elements are real. Representing the final eigenstates as

$$|\Psi_j(k)\rangle = \sum_{\underline{\nu}} u_{\underline{\nu}\,j}(k)|k\underline{\nu}\rangle\ , \tag{111}$$

we obtain the eigenvalue problem

$$\sum_{\underline{\mu}}\langle k\underline{\mu}|H_{\mathrm{Hol}}^{\mathrm{FE}}|k\underline{\nu}\rangle \cdot u_{\underline{\mu}\,j} = E_j \cdot u_{\underline{\nu}\,j} \tag{112}$$

for the real matrix $\langle k\underline{\mu}|H_{\mathrm{Hol}}^{\mathrm{FE}}|k\underline{\nu}\rangle$. Its eigenvalues E_j and eigenstates $|\Psi_j(k)\rangle$ are the stationary solutions of the Holstein Hamiltonian (101).

3.4 Transition dipoles and phonon clouds of the eigenstates

The properties of the eigenstates (111) are easily computed. We start with the Frenkel exciton character (FE character) defined as in Eq. (38) by the projection onto a purely electronic Frenkel exciton state $a_k^\dagger|o\rangle$:

$$F_{\mathrm{FE}j}(k) \equiv |\langle\Psi_j(k)|a_k^\dagger|o\rangle|^2\ . \tag{113}$$

By use of the explicit expression (111) for the basis state and the inverse Fourier transformations, one obtains:

$$F_{\mathrm{FE}j}(k) = \left|\sum_{\underline{\nu}} u^*_{\underline{\nu}\,j}(k)\langle n\underline{\nu}|a_n^\dagger|o\rangle\right|^2\ . \tag{114}$$

The matrix element $\langle n\underline{\nu}|a_n^\dagger|o\rangle$ can be split into its electronic and vibrational components according to Eq. (102):

$$\begin{aligned}\langle n\underline{\nu}|a_n^\dagger|o\rangle &= \langle a_n^\dagger\tilde{B}^\dagger_{n\underline{\nu}}o|a_n^\dagger|o\rangle \\ &= \underbrace{\langle a_n^\dagger o_{\mathrm{el}}|a_n^\dagger|o_{\mathrm{el}}\rangle}_{=1}\times\langle\tilde{B}^\dagger_{n\underline{\nu}}o_{\mathrm{vib}}|o_{\mathrm{vib}}\rangle\ .\end{aligned}$$

The vibrational overlap factor in this equation can be formally evaluated by use of Eq. (103). Very obviously, it gives a factor S from position n, where the displaced vibrational wave function

of level ν_0 overlaps with the undisplaced vibrational ground state. At all other lattice positions $n+r$, we have the Kronecker symbol for the orthogonality of the wave functions in the same undisplaced potential:

$$\langle n\underline{\nu}|a_n^\dagger|o\rangle = \langle \tilde{B}_{n\underline{\nu}}^\dagger o_{\rm vib}|o_{\rm vib}\rangle = S\binom{\nu_0}{0}\prod_{r\neq 0}\delta_{\nu_r,0}\ . \tag{115}$$

Thus, the Frenkel exciton character becomes:

$$F_{{\rm FE}j}(k) = \left|\sum_{\underline{\nu}} u_{\underline{\nu}j}^*(k) S\binom{\nu_0}{0}\prod_{r\neq 0}\delta_{\nu_r,0}\right|^2\ . \tag{116}$$

The characters obey the sum rule

$$\sum_j F_{{\rm FE}j}^2(k) = 1\ . \tag{117}$$

since

$$\begin{aligned}
\sum_j F_{{\rm FE}j}^2(k) &= \sum_j |\langle\Psi_j(k)|a_k^\dagger|o\rangle|^2 \\
&= \sum_j \langle o|a_k|\Psi_j(k)\rangle\langle\Psi_j(k)|a_k^\dagger|o\rangle \\
&= \langle o|a_k \underbrace{\sum_j |\Psi_j(k)\rangle\langle\Psi_j(k)|}_{=\mathbf{1}} a_k^\dagger|o\rangle \\
&= 1\ .
\end{aligned}$$

As in the electronic problem, the exciton character determines the oscillator strength of a $k=0$ state. The transition dipole of state $|\Psi_j(k)\rangle$ is

$$\begin{aligned}
\vec{P}_j &= \langle\Psi_j(k)|\hat{\vec{P}}|o\rangle \\
&= \sum_{\underline{\nu}} u_{\underline{\nu}j}^*(k)\langle k\underline{\nu}|\hat{\vec{P}}|o\rangle \\
&= \sum_{\underline{\nu}} u_{\underline{\nu}j}^*(k)\frac{1}{\sqrt{N}}\sum_n {\rm e}^{{\rm i}kn}\langle n\underline{\nu}|\hat{\vec{P}}|o\rangle\ .
\end{aligned} \tag{118}$$

For the transition dipole of the basis state $|n\underline{\nu}\rangle$, we have to use the approximate separability of the transition dipole moment into an electronic part and a vibrational overlap factor as in Eq. (84) for the isolated molecule. Then, the transition dipole of each basis state $|n\underline{\nu}\rangle$ becomes

$$\langle n\underline{\nu}|\hat{\vec{P}}|o\rangle = \langle a_n^\dagger \tilde{B}_{n\underline{\nu}}^\dagger o|\hat{\vec{P}}|o\rangle \tag{119}$$

$$= \underbrace{\langle a_n^\dagger o_{\rm el}|\hat{\vec{P}}|o_{\rm el}\rangle}_{\vec{p}_{\rm FE}} \times \underbrace{\langle \tilde{B}_{n\underline{\nu}}^\dagger o_{\rm vib}|o_{\rm vib}\rangle}_{\text{Eq. (115)}} \tag{120}$$

$$= \vec{p}_{\rm FE} \times S\binom{\nu_0}{0}\prod_{r\neq 0}\delta_{\nu_r,0}\ . \tag{121}$$

Thus, with identity (12) the transition dipole becomes

$$\vec{P}_j = \delta_{k,0}\sqrt{N}\vec{p}_{\mathrm{FE}} \times \sum_{\underline{\nu}} u^*_{\underline{\nu}\,j}(k) S \begin{pmatrix} \nu_0 \\ 0 \end{pmatrix} \prod_{r\neq 0} \delta_{\nu_r,0}$$

Comparison of this equation with the expression (116) for the Frenkel exciton character shows that the squared transition dipole is given by the character

$$|\vec{P}_j|^2 = \delta_{k,0} N \vec{p}^{\,2}_{\mathrm{FE}} F_{\mathrm{FE}j}(k) \;, \tag{122}$$

and the oscillator strength (see Eq. (53)) of a $k = 0$ state is proportional to the Frenkel character:

$$f_j = \frac{2mE_j}{e^2\hbar^2} N \vec{p}^{\,2}_{\mathrm{FE}} \times F_{\mathrm{FE}j}(0) \;. \tag{123}$$

This equation is identical to the corresponding expression (54) for the FE oscillator strength in the electronic problem, since the transition dipole is a purely electronic operator and its action on a vibronic state is only determined by the electronic character of this state.

As an illustration, we show in Fig. 11 the results of such a calculation for $k = 0$ and the parameters $J = 0.5\hbar\omega$ and $g = 1$. The energy levels E_j of the eigenstates are arranged at a vertical energy axis in the left part. Their FE character $F_{\mathrm{FE}j}$ is indicated by the horizontal length of each stick. The lowest state appears as a solitary stick at $E_1 = 0.0074\hbar\omega$. At higher energies, the spectrum consists of many densely packed lines resulting from the mixture of the various phonon cloud configurations in the basis set. The numerical spectrum remains discrete only since the basis is finite. To illustrate the dense vibronic manifold, we always convolve stick spectra with a Gaussian of constant standard derivation ($\sigma = 0.15\hbar\omega$) and show the broadened spectrum using a convenient scaling factor.

Another important property of a vibronic state $|\Psi_j(k)\rangle$ is the internal structure of its phonon cloud. One measure to characterize it is the set of expectation values $\langle \hat{N}_m \rangle$ for the occupation number operators:

$$\langle \hat{N}_m \rangle \equiv \langle \sum_n a^\dagger_n a_n b^\dagger_{n+m} b_{n+m} \rangle \;. \tag{124}$$

These occupation numbers show how many phonons are excited at the oscillator that is m lattice spacings apart from the exciton. Note that they depend on the displacement chosen for the oscillator functions in the basis set. Thus, they are no observable quantities. They are mainly important for choosing a reasonable basis set: Since numerically for each relative site m, only states up to a predefined number $\nu_m^{\max}$ can be included in the basis set, it must be assured that $\langle \hat{N}_m \rangle \ll \nu_m^{\max}$. These phonon occupation numbers are again illustrated in Fig. 11 for two representative eigenstates of high spectral weight. For the lowest state at $E_1 = 0.0074\hbar\omega$, there are 0.16 phonons at the exciton site ($m = 0$), and the total phonon number is $\sum_m \langle N_m \rangle = 0.34$. In the molecular limit, this state would be the zero-phonon state, but the hopping term J leads to a nonzero phonon occupation number. At a higher state $E_{41} = 2.28\hbar\omega$, the total phonon number is 2.12 with a peak value of $\langle \hat{N}_0 \rangle = 1.05$. This state originates from the 2-phonon state in the molecular limit. Electronic delocalization leads to broad phonon clouds.

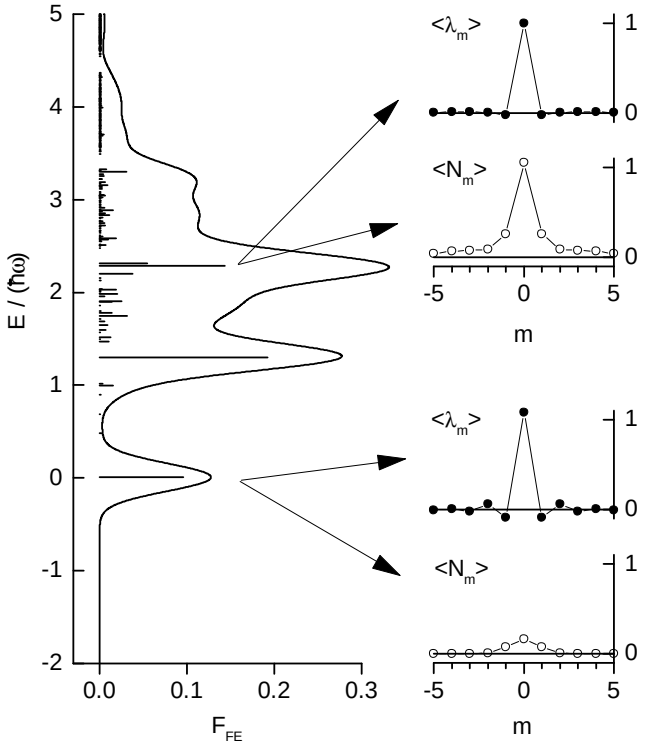

Figure 11:
Illustration of the eigenstates and their properties for a numerical solution of the Holstein model (101) with parameters $J = 0.5\hbar\omega$ and $g = 1$ at total momentum $k = 0$. In the left panel, the optically active eigenstates are shown at a vertical energy axis. The sticks indicate the FE character $F_{\mathrm{FE}j}$ of each state according to Eq. (116). For a visualization of the resulting spectrum, the stick spectrum is convolved with a Gaussian (standard derivation $\sigma = 0.15\hbar\omega$) and the broadened spectrum is scaled for easy superposition (here: area $\int f(E)dE = 0.5\hbar\omega$). In the right panels, the occupation number clouds $\langle\hat{N}_m\rangle$ and displacement clouds $\langle\hat{\lambda}_m\rangle$ are shown for two particular eigenstates (cf. comments to Eqs. (124) and (125)).

A description of the phonon cloud that is independent of the basis set can be provided by the expectation values of the displacement operators:

$$\langle\lambda_m\rangle \equiv \langle\sum_n a_n^\dagger a_n \frac{b_{n+m}^\dagger + b_{n+m}}{2}\rangle \ . \tag{125}$$

This displacement cloud $\langle\lambda_m\rangle$ gives the average distortion from equilibrium (along the dimensionless normal coordinate λ) at a molecule which is m sites from the exciton. Note that the exciton itself is completely delocalized in real space and so is its displacement cloud. This delocalization follows directly from the assumed perfect translational symmetry. The values $\langle\lambda_m\rangle$ as

a function of the distance m only show the spatial correlation between the electronic excitation and the lattice distortion.

With respect to the basis representation (102), the displacement cloud of a state $|\Psi_j(k)\rangle$ (111) is obtained as:

$$\begin{aligned}\langle\lambda_m\rangle &= \sum_{\underline{\mu}\,\underline{\nu}} u^*_{\underline{\mu}\,j} u_{\underline{\nu}\,j} \times \left(\prod_{r\neq m} \delta_{\mu_r,\nu_r}\right) \\ &\times \left(\frac{\sqrt{\nu_m+1}}{2}\delta_{\mu_m,\nu_m+1} + \frac{\sqrt{\nu_m}}{2}\delta_{\mu_m,\nu_m-1}\right. \\ &\left. + g\,\delta_{m,0}\,\delta_{\mu_0,\nu_0}\right) . \end{aligned} \tag{126}$$

Again, Fig. 11 may serve as an illustration. There, the displacement clouds are shown for the same representative states that were analyzed in terms of occupation number clouds. The narrow clouds show that the actual lattice distortion is much more localized around the exciton than the broad occupation number clouds might suggest. This difference results from the fact that the vibronic wavefunction in the actual eigenstates cannot be accurately represented by single oscillator functions of the special Lang-Firsov basis.

3.5 Truncated phonon basis and symmetry adaptation

By now, the formal tools for calculating and analyzing the eigenstates of the Holstein Hamiltonian (101) have been collected. The only remaining issue is how to truncate the infinite phonon-cloud basis to a number that allows numerical diagonalization. For this, we first restrict the basis to cloud states of the form

$$|\underline{\nu}_M\rangle = |\nu_{-M}\ldots\tilde{\nu}_0\ldots\nu_{+M}\rangle\ , \tag{127}$$

as motivated below Eq. (103). That means, only phonon clouds localized at the $2M+1$ molecules around the exciton are included. Strongly delocalized or even free phonons can only be approximated using large M.

Second, for each position in the phonon-cloud we restrict the maximum occupation number:

$$\nu_m \leq \nu_m^{\max}\ . \tag{128}$$

In this way, the localized nature of the phonon cloud can better be taken into account by considering only small occupation numbers $\nu_m^{\max}$ at sites far away from the exciton. A typical cut-off vector as used for the calculation in Fig. 11 has $M=5$ and looks like $|12345\tilde{6}54321\rangle$.

Third, among these states we include only those for which the total number of phonons does not exceed a given maximum:

$$\sum_m \nu_m \leq \nu_{\rm tot}^{\max}\ . \tag{129}$$

In this way, high energy basis states are excluded. Since the overlap factors for states with high vibrational excitation decrease rapidly, these states do not appear in the absorption spectrum. Condition (129) is only effective for $\nu_{\mathrm{tot}}^{\mathrm{max}} < \sum_m \nu_m^{\mathrm{max}}$, but typically it can be used as a strong restriction (e.g. $\nu_{\mathrm{tot}}^{\mathrm{max}} = 6$ in Fig. 11).

Now, we have arrived at a fairly complex description for the cut-off conditions of the basis set, given by the numbers M, $\underline{\nu}^{\mathrm{max}}$, $\nu_{\mathrm{tot}}^{\mathrm{max}}$. However, this complex scheme allows to choose a basis just large enough to represent the optically active eigenstates of the Hamiltonian.

The minimum radius, $M = 0$, is an important special case of the phonon basis in which electronic and vibrational excitations are always at the same site, just as in the $J = 0$ limit. These joint exciton-phonon configurations (see illustration in Fig. 9) can be considered as distinct molecular excited states and treated within the standard framework of Frenkel exciton theory. Following Broude, Rashba and Sheka ([47], p. 185), we call this the *molecular vibron model*:

$$M = 0 \; . \tag{130}$$

The molecular vibron model follows naturally from the exciton concept and was successfully applied to early interpretations of crystal spectra [26]. The approximation is additionally justified if — beyond the simplest Holstein Hamiltonian (101) — the phonon energy differs between the electronic ground and excited state of the molecule (cf. Ref. [3], p. 87ff or Ref. [47], p. 198f).

To find a suitable phonon basis for concrete calculations, we start with the molecular vibron model and gradually increase the phonon basis until the obtained absorption spectrum converges. This procedure is demonstrated in Ref. [41].

In addition to the general truncation scheme, in some cases the dimension of the phonon basis can be reduced by symmetry. For the Frenkel exciton problem in this section, we have inversion symmetry about the exciton's site. So we can introduce symmetry adapted basis states $|k\underline{\nu}\rangle_{\pm}$ in which the phonon cloud is either symmetric (+) or antisymmetric (−) with respect to inversion about its center. Inversion of the phonon cloud in the non-adapted basis (104) shall be denoted by a bar:

$$|\underline{\bar{\nu}}\rangle \quad : \quad \bar{\nu}_n = \nu_{-n} \; . \tag{131}$$

Even the non-adapted basis contains some symmetric phonon-clouds ($\underline{\bar{\nu}} = \underline{\nu}$). For all other states, a symmetry adaption has to be chosen. Thus, the symmetry adapted states can be obtained as:

$$\begin{aligned} |k\underline{\nu}\rangle_+ &= \begin{cases} |k\underline{\nu}\rangle & \text{for} \quad \underline{\bar{\nu}} = \underline{\nu} \\ \frac{1}{\sqrt{2}} \left(|k\underline{\nu}\rangle + |k\underline{\bar{\nu}}\rangle \right) & \text{for} \quad \underline{\bar{\nu}} \neq \underline{\nu} \end{cases} \\ |k\underline{\nu}\rangle_- &= \frac{1}{\sqrt{2}} \left(|k\underline{\nu}\rangle - |k\underline{\bar{\nu}}\rangle \right) \quad \text{for} \quad \underline{\bar{\nu}} \neq \underline{\nu} \end{aligned} \tag{132}$$

Now, the symmetric subspace spanned by the $|k\underline{\nu}\rangle_+$ states does not mix with the antisymmetric subspace spanned by the $|k\underline{\nu}\rangle_-$ states and the diagonalization can be done separately for both subspaces. For a large cut-off radius of the the phonon cloud, the dimension of the two subspaces is roughly one half of the original basis. Furthermore, the transition dipoles of all antisymmetric states vanish exactly and only the symmetric space is needed for the absorption spectrum.

3.6 The limit for weak intermolecular electronic coupling

In order to illustrate the qualitative effects that arise from exciton transfer, we will now apply perturbation theory for the limit of weak electronic coupling ($J \ll g\hbar\omega$). The reference system is given by the molecular limit ($J = 0$). Then, the molecular vibron model (130) gives an exact description of the optically active states, which form an equally spaced vibronic progression (cf. Fig. 11a). We consider the lowest (zero-phonon) and second lowest (one-phonon) molecular vibronic states.

The lowest state of the unperturbed system is $|k\underline{\nu}\rangle$ with $|\underline{\nu}\rangle = |\ldots 0\tilde{0}0\ldots\rangle$. This state at $E_1^{(0)} = 0$ is non-degenerate, and application of first order perturbation theory gives immediately

$$E_1^{(1)} = \langle k\underline{\nu}|H_{\rm Hol}^{\rm FE}|k\underline{\nu}\rangle = 2J\cos(k) \times S^2 \begin{pmatrix} 0 \\ 0 \end{pmatrix} = 2J\cos(k) \times {\rm e}^{-g^2} \; . \tag{133}$$

This result is well known from small polaron theory for zero temperature. The width $4J$ of the purely electronic band is renormalized by the overlap factor ${\rm e}^{-g^2}$ since the exciton moves together with its displacement cloud.

The second lowest state of the unperturbed system is, in the molecular vibron model, $|k\underline{\nu}\rangle$ with $|\underline{\nu}\rangle = |\ldots 0\tilde{1}0\ldots\rangle$. This is the molecular one-phonon state. Considering a complete phonon basis, the molecular one-phonon state is degenerate with with all other dark basis states that contain one phonon excitation at an arbitrary exciton-phonon separation n. A perturbation $J > 0$ will mix all these states and lift their degeneracy.

This can be analyzed by writing down the matrix elements (110) for the states of the one-phonon manifold. We define the state $|k\underline{\mu}(n)\rangle$ by a phonon cloud with the structure $\nu_i = \delta_{i,n}$ and analogously for $|k\underline{\mu}(m)\rangle$: $\mu_i = \delta_{i,m}$. The matrix representation (110) then becomes

$$\begin{aligned} H_{mn} &= \langle k\underline{\mu}(m)|H_{\rm Hol}^{\rm FE}|k\underline{\nu}(n)\rangle \\ &= \delta_{m,n}\hbar\omega + J{\rm e}^{-g^2}(W_{mn} + g^2 V_{mn}) \; , \end{aligned} \tag{134}$$

where

$$W_{mn} = \delta_{m,n+1} \times {\rm e}^{-{\rm i}k} + \delta_{m,n-1} \times {\rm e}^{+{\rm i}k} \tag{135}$$

$$= \begin{pmatrix} \ddots & & & & & & \\ \cdots & 0 & {\rm e}^{{\rm i}k} & 0 & 0 & 0 & \cdots \\ \cdots & {\rm e}^{-{\rm i}k} & 0 & {\rm e}^{{\rm i}k} & 0 & 0 & \cdots \\ \cdots & 0 & {\rm e}^{-{\rm i}k} & 0 & {\rm e}^{{\rm i}k} & 0 & \cdots \\ \cdots & 0 & 0 & {\rm e}^{-{\rm i}k} & 0 & {\rm e}^{{\rm i}k} & \cdots \\ \cdots & 0 & 0 & 0 & {\rm e}^{-{\rm i}k} & 0 & \cdots \\ & & & & & & \ddots \end{pmatrix} \; ,$$

and V_{mn} is a matrix that has nonzero-elements only for $|m|, |n| \leq 1$:

$$V_{mn} = \begin{pmatrix} \ddots & & & & & & \\ \cdots & 0 & 0 & 0 & 0 & 0 & \cdots \\ \cdots & 0 & 0 & -\mathrm{e}^{\mathrm{i}k} & \mathrm{e}^{\mathrm{i}k} & 0 & \cdots \\ \cdots & 0 & -\mathrm{e}^{-\mathrm{i}k} & 2\cos k & -\mathrm{e}^{\mathrm{i}k} & 0 & \cdots \\ \cdots & 0 & \mathrm{e}^{-\mathrm{i}k} & -\mathrm{e}^{-\mathrm{i}k} & 0 & 0 & \cdots \\ \cdots & 0 & 0 & 0 & 0 & 0 & \cdots \\ & & & & & & \ddots \end{pmatrix} . \tag{136}$$

The non-diagonal contributions in W_{mn} and V_{mn} mix the joint configuration from the molecular vibron model with separated configurations. However, V_{mn} only mixes the states where the phonon is located either at the exciton site or at its nearest neighbor. Therefore, W_{mn} and V_{mn} act in completely different ways.

Let us first discuss the case of $g \ll 1$ and neglect V_{mn} in Eq. (134). For $k = 0$ or $k = \pi$, W_{mn} is the Hamiltonian of a nearest-neighbor hopping particle on an infinite chain with open boundary. This gives a wave-like solution. In contrast to the ordinary hopping problem, the exact consideration of the specific boundary conditions is essential now. Only then, the correct amplitude at the special site $n = 0$ can be obtained; and this amplitude alone determines the exciton character. Thus, one obtains the eigenstates

$$|\Psi_j\rangle = \frac{1}{\sqrt{M+1}} \sum_{n=-M}^{M} \sin\left(\frac{n\, j\, \pi}{2M+2}\right) \; |k\underline{\nu}(n)\rangle \tag{137}$$

with

$$j = 1, 2, \ldots, 2M+1 \; . \tag{138}$$

Their energies are

$$E_j^{(1\mathrm{ph}, g \ll 1)} = \hbar\omega \pm 2J\mathrm{e}^{-g^2} \cos\left(\frac{j\,\pi}{M+1}\right) \; , \tag{139}$$

where $\pm$ refers to $k = 0$ and $k = \pi$, respectively. The FE character of state j at $k = 0$ follows from Eq. (116). It has only two values depending on the index j:

$$F_{\mathrm{FE}j} = \begin{cases} \frac{1}{M+1} \cdot g^2 e^{-g^2} & \text{for odd} \quad j \\ 0 & \text{for even} \quad j \end{cases} \; . \tag{140}$$

The M states with even j and zero FE character belong to the subspace of the antisymmetric states in the symmetry adapted basis (132). The $M+1$ optically active states with odd j are the symmetric states. These active states form a band of equally absorbing states with a total width of $4Je^{-g^2}$. The total FE character of these active states sums up to $g^2e^{-g^2}$ representing

the value of the molecular limit. In all these states, the phonon cloud is not localized around the exciton but consists of a standing phonon wave. We emphasize that this behavior is the limit for small g. In this limit, the total FE character of the considered one-phonon band gives only a small feature in the overall absorption spectrum since the major part of the FE character is concentrated in the zero-phonon state.

Complementary, the V_{mn} part in the perturbation expression (134) mixes only the cloud states with phonon excitations at or next to the exciton site. Therefore, in the limit of large g, the basis set can be reduced to include only local phonon cloud configurations up the the nearest neighbor ($M = 1$). Using the symmetry adapted basis functions (132), the symmetric one-phonon subspace consists only of two phonon configurations: $|\Phi_1(k)\rangle = |k\rangle|0\tilde{1}0\rangle_+$ and $|\Phi_2(k)\rangle = |k\rangle|1\tilde{0}0\rangle_+$. The Hamiltonian in the representation of these two states takes the form

$$H_{mn} = \delta_{mn}\hbar\omega + 2J\mathrm{e}^{-g^2}\cos(k) \times \begin{pmatrix} g^2 & \frac{1-g^2}{\sqrt{2}} \\ \frac{1-g^2}{\sqrt{2}} & \frac{1}{2}g^2 \end{pmatrix} \tag{141}$$

with eigenvalues

$$\begin{aligned} E_\pm^{(1\mathrm{ph},g\gg1)} = \hbar\omega \quad &+ \quad 2J\cos(k) \times g^2\mathrm{e}^{-g^2} \\ &\times\frac{3}{4}\left(1 \pm \sqrt{1 - \frac{16}{9g^2} + \frac{8}{9g^4}}\right). \end{aligned} \tag{142}$$

Thus, the zero-order energy $E = \hbar\omega$ splits into two bands $E_\pm(k)$. Similarly to the perturbation-in-J treatment of the lowest state (133), the electronic bandwidth $4J$ is multiplied by an overlap factor $g^2\mathrm{e}^{-g^2}$ which corresponds to the interaction of the transition-dipole moments of the molecular one-phonon state. However, there are *two* states now. In the limit $g \to \infty$, their energies tend to:

$$E_+^{(1\mathrm{ph},g\to\infty)} \quad \to \quad \hbar\omega + 2J\cos k \cdot g^2\mathrm{e}^{-g^2} \times \frac{3}{4} \tag{143}$$

$$E_-^{(1\mathrm{ph},g\to\infty)} \quad \to \quad \hbar\omega \tag{144}$$

In this limit, both states still have an FE character of $F_{\mathrm{FE}+} \to \frac{2}{3}$ and $F_{\mathrm{FE}-} \to \frac{1}{3}$.

This splitting into two states which both carry spectral weight is entirely caused by the delocalization of the phonon cloud. Such a delocalization is neglected in the simplest approach of the molecular vibron model (130), which would mean the neglect of state $|\Phi_2(k)\rangle$ in Hamiltonian (141). Looking at the non-diagonal term in Hamiltonian (141) suggests, and closer inspection of the full one-phonon subspace Hamiltonian (134) confirms: For the special value $g = 1$, the molecular vibron state $|k\underline{\nu}(n = 0)\rangle$ decouples from all other phonon cloud configurations. Only in this case, the molecular vibron model becomes exact (in the one-phonon subspace) and yields one energy band at

$$E^{(1\mathrm{ph},g=1)} = \hbar\omega + 2J\cos k \cdot g^2\mathrm{e}^{-g^2} \tag{145}$$

which includes the complete FE character of the one-phonon state ($g^2\mathrm{e}^{-g^2}$).

To give an illustration of the phenomena in the one-phonon subspace and to show the relevance of the described limiting cases, we show a numerical solution in Fig. 12. For this, we solved the Hamiltonian (134) numerically for a phonon cloud of radius $M = 20$ at the total momentum $k = 0$. For $k = \pi$, the spectra only have to be mirrored with respect to $E = \hbar\omega$.

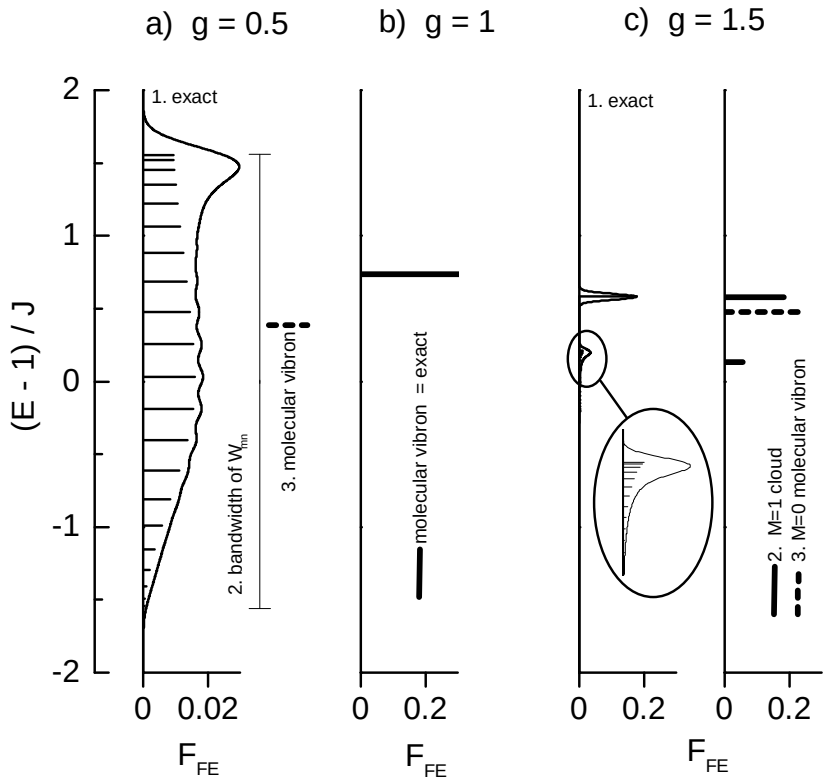

Figure 12:
Perturbative treatment $J \to 0$ of the one-phonon subspace for three coupling parameters g. The "exact" stick spectra are numerical solutions of the one-phonon Hamiltonian (134) for a phonon-cloud radius of $M = 20$. The envelopes are convolutions of the stick spectra with Gaussians of appropriate width. Fig. 12a represents the small-g case, where a broad one-phonon sideband is formed. The "exact" solution in graph 1 is compared to the bandwidth of the free-phonon part (W_{mn} from Eq. (139)) in graph 2 and to the position of the single active state from the molecular vibron model (130) in graph 3. Fig. 12b represents the $g = 1$ case, where the molecular vibron model becomes exact. Fig. 12c represents the large-g case, in which the exciton interacts mainly with a nearest neighbor phonon cloud. The "exact" numerical solution in graph 1 resembles the approximate solution (141) for a nearest neighbor cloud ($M = 1$) in graph 2. The single state from the molecular vibron model ($M = 0$) is shown in graph 3.

In Fig. 12a, the "exact" numerical results (graph 1) are shown for a relatively small $g = 0.5$.

The tendency of a broad band with constant FE character is clearly visible. This bandwidth is compared to the width the free phonon part W_{mn} from Eq. (139) in graph 2. Both agree very well. The molecular vibron model ($M = 0$) would give a single active sate at $(E-\hbar\omega)/J = 0.389$ (position indicated by graph 3). This state would represent the weighted center of the exact band but it would veil the large splitting ($\Delta E/J \approx 1.55$).

In Fig. 12c, the numerical solution is shown for a rather large $g = 1.5$ (graph 1). It clearly approaches the two active states from the nearest neighbor cloud (radius $M = 1$) given by Eq. (142), which is shown in graph 2. For comparison, the result of the molecular vibron model ($M = 0$) is also shown in graph 3. As for $g < 1$, the molecular vibron model can only represent the weighted center of the one-phonon states but not their qualitative splitting. Note that for both cases $g < 1$ and $g > 1$ the correct splittings of the one-phonon states are on the same order as the perturbation parameter J.

The situation for energies above the one-phonon subspace becomes more complex and will not be considered here. Already in the two-phonon subspace, which is spanned by all zero-order basis states with a total phonon number 2, there occurs a high degeneracy of various cloud configurations. The numerical calculations in Ref. [41] confirm that for not too strong electronic coupling ($J \lessapprox 0.5\hbar\omega$) and g in the order of 1, the approximation of highly localized phonon clouds or even the molecular vibron model yields a good description of the full absorption spectrum.

3.7 Numerical solutions for various electronic coupling strengths

In this section, we want to give an impression of absorption spectra for various conditions. We always consider an electron-phonon coupling constant of $g = 1$, which is a typical order of magnitude for the strongly coupled modes in π-conjugated systems. The numerical spectra were calculated with phonon cloud radius $M = 5$, a maximum total phonon number $\nu_{\mathrm{tot}}^{\max} = 6$ (cf. Eq. (129)) and a phonon cloud cut-off vector of $|\underline{\nu}^{\max}\rangle = |12345\tilde{6}54321\rangle$ (cf. Eq. (128)) corresponding to 4485 symmetric basis states in the symmetry adapted basis (132). This ensures a sufficient accuracy for all shown spectra (on the order of the graphic resolution) except for the numerically demanding case $J = 1\hbar\omega$, $k = 0$. In this case, deviations on the order of about 10% might occur on the high energy side ($E > 3\hbar\omega$).

As discussed in the previous section, for $g = 1$ the molecular vibron model (cf. Eq. (130)) is a good approximation for weak electronic coupling ($J \ll g\hbar\omega$). At first, we illustrate the quality of this approximation for intermediate positive J at $k = 0$ (top of the band). In Fig. 13, we compare the discrete vibronic states resulting from the molecular vibron model with the complete numerical solutions. For $J = 0.5\hbar\omega$, the molecular vibron model still gives a qualitatively reasonable description of the spectrum. The main effect of the delocalized cloud basis in the high energy region is a broadening of the spectra. The lowest state, however, moves considerably from $E_1 = 0.229\hbar\omega$ in the molecular vibron model to $E_1 = 0.0074\hbar\omega$ in the largest basis set. For $J = 1\hbar\omega$, the deviations between the molecular vibron model and the exact solution are already on the same order as all structures in the spectrum.

To give an overview about general trends, we show characters and electronic bands for $g = 1$

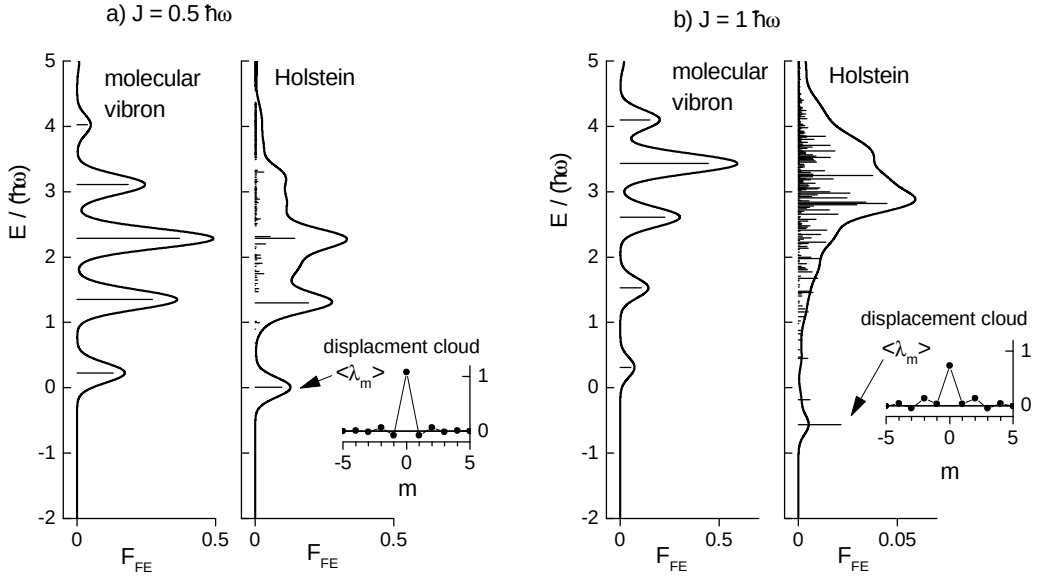

Figure 13:
Comparison of the molecular vibron model (left panels) and the numerical solution for the complete Holstein problem (right panels) for two exciton transfer integrals: **a)** $J = 0.5\hbar\omega$, **b)** $J = 1\hbar\omega$. Exciton-phonon coupling is $g = 1$ and quasi-momentum is $k = 0$.

and various J in Fig. 14. The electronic bands $E_{\mathrm{elec}}(k)$ in this figure are the solutions of the electronic Hamiltonian $H^{\mathrm{FE}}_{\mathrm{elec}} + g^2\hbar\omega$ (cf. Eq. (100)). The molecular Franck-Condon relaxation energy $g^2\hbar\omega$ has to be added to comply with our energy axis definition, in which the relaxed molecular zero-phonon state lies at $E = 0$. The states and spectra resulting from the complete Holstein Hamiltonian $H^{\mathrm{FE}}_{\mathrm{Hol}}$ (Eq. (101)) are shown at $k = 0$ and $k = \pi$.

In the non-interacting case $J = 0$ (Fig. 14a), the electronic dispersion is zero and the spectra are the vibronic states of the isolated molecule. The molecular zero phonon state lies below the electronic band by the amount of the Franck-Condon relaxation energy $g^2\hbar\omega$.

For a moderately small interaction $J = 0.5\hbar\omega$ (Fig. 14b), the spectrum still shows distinct peaks reminding of the molecular vibronic states. However, the shape of the spectrum is changed. In particular, the spectrum loses one fingerprint of a vibronic progression in the molecular case, namely the constant energy spacing between the peaks. The centers of mass of the spectra are shifted upwards at the top of the band ($k = 0$) and downwards at the bottom of the band ($k = \pi$), corresponding to the dispersion of the electronic band. The bandwidth of the lowest dressed exciton state is $\Delta E = 0.62\hbar\omega$, which is still similar to the weak-electronic coupling limit of $4J\mathrm{e}^{-g^2} = 0.74\hbar\omega$.

For stronger interaction, $J = 1\hbar\omega$ (Fig. 14c), the spectra already show the tendency towards the opposite limiting case. Instead of a number of vibronic peaks, just one major peak close to the position of the electronic bands starts to emerge. Furthermore, there remains a small

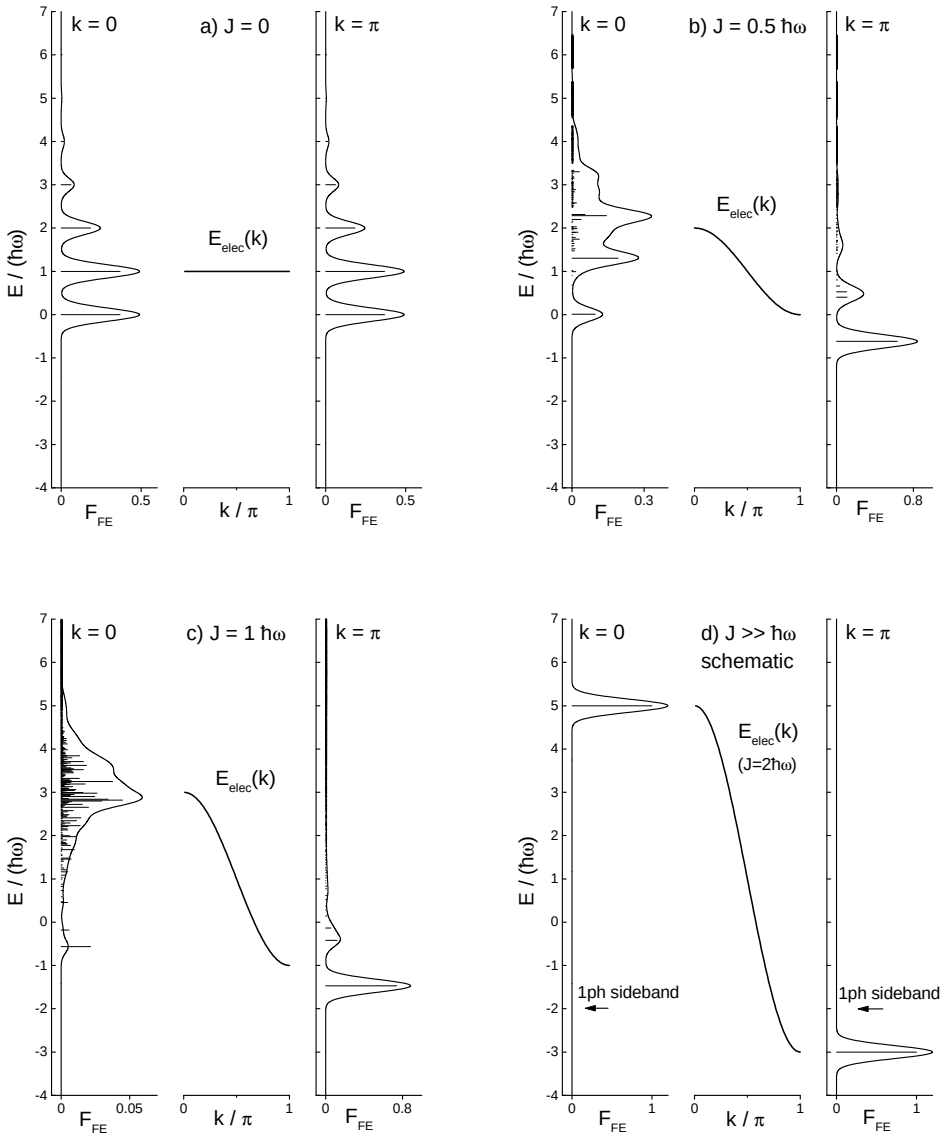

Figure 14:
Overview of band structures in the Holstein model for fixed exciton phonon coupling constant $g = 1$ and various exciton hopping integrals J. The vibronic spectra at $k = 0$ and $k = \pi$ were calculated and represented as for Fig. 11. For the limiting case $J \gg \hbar\omega$, we show only schematic spectra at energy positions corresponding to the electronic bands for $J = 2\hbar\omega$.

one-phonon sideband approximately one vibrational quantum above the bottom of the band structure (at $k = \pi$). The one-phonon sideband at $k = 0$ corresponds to a mixture of the lowest

$k = \pi$ dressed exciton and a $k = -\pi$ phonon. For further increasing J, this one-phonon sideband will more and more lose its spectral weight. Nevertheless, there remains a low-lying $k = 0$ state which determines the overall dispersion of the lowest state to approximately one-vibrational quantum, independently of the stronger and stronger electronic dispersion $4J$.[11]

The limit of strong electronic coupling is schematically depicted in Fig. 14d. The electronic band is shown for the example of $J = 2\hbar\omega$. The given absorption spectra, however, are not calculated but only serve as a schematic illustration. In the strong coupling limit, the electronic bandwidth $4J$ is large compared to the molecular Franck-Condon relaxation energy $g^2\hbar\omega$, the exciton hopping is "fast" compared to the exciton-phonon coupling and the Born-Oppenheimer approximation should be applied to the whole crystal as one object (cf. Ref. [81]). The total lattice displacement $\sum\langle\lambda_m\rangle = g$ is now equally distributed over the $N \to \infty$ molecules. Therefore, the total relaxation energy $E_{\rm FC} = g^2\hbar\omega\sum\langle\lambda_m\rangle^2$ tends to zero. Figuratively speaking, the very fast exciton loses its phonon cloud. Compared to the molecular limit (lowest state at $E = 0$), the lowest state will now be given by the purely electronic band at $E = 2J\cos k + g^2\hbar\omega$. Because of the vanishing relaxation energy, higher vibronic states have no spectral weight and the absorption spectrum consists of a narrow line at the electronic energy. The position of the one-phonon sidebands is also indicated, but these side-bands have vanishing spectral weight in the limit $J \to \infty$.

3.8 The Holstein Hamiltonian with charge-transfer states

The Holstein Hamiltonian for Frenkel excitons (101) can be very naturally extended to include charge-transfer states (CT states). Let $c^\dagger_{n,f}$ be the creation operator for a nearest-neighbor CT state in which an electron is transferred from lattice site n to site $n + f$ ($f = \pm 1$). The molecular limit is again defined as the case where no transfer interactions (neither Frenkel exciton transfer nor charge transfer nor Frenkel-CT interactions) are considered. Then, the electronic CT Hamiltonian is

$$H^{\rm CT} = D\sum_{n,f} c^\dagger_{n,f}c_{n,f}\ , \tag{146}$$

with D being the on-site energy of a CT state in the molecular limit (relative to the Frenkel exciton on-site energy at zero in our energy units).

The electron or hole excitation of the CT state are assumed to couple to the same effective vibrational coordinate λ as the Frenkel exciton. With the electron-phonon coupling constant $g_{\rm e}$ and the hole-phonon coupling constant $g_{\rm h}$, the linear coupling between CT states and phonons is described by the Hamiltonian

$$H^{\rm CT-ph} = \hbar\omega\sum_{n,f} c^\dagger_{n,f}c_{n,f}$$

[11] This behavior of the dispersion depends on the exciton-phonon coupling constant g. If the exciton-phonon coupling energy $g^2\hbar\omega$ is large compared to the electronic bandwidth $4J$, the bandwidth of the lowest dressed sate takes the value of the weak-electronic coupling limit $4J{\rm e}^{-g^2}$, which can be smaller than $\hbar\omega$. For a detailed discussion, see e.g. Ref. [60].

$$\times \Big[-g_{\mathrm{h}}(b_n^\dagger + b_n) - g_{\mathrm{e}}(b_{n+f}^\dagger + b_{n+f}) + g_h^2 + g_{\mathrm{e}}^2 \Big] . \tag{147}$$

These expressions are analogous to the Frenkel-exciton-phonon coupling in Eq. (99). The term $(g_h^2 + g_{\mathrm{e}}^2)\hbar\omega$ is the vibrational relaxation energy of a CT state in the molecular limit. As in Eq. (99), this term is added to align the on-site energy D of the CT states to its value in the molecular limit.

For the electronic mixing between Frenkel and CT excitons, we use the corresponding part from the Merrifield Hamiltonian (27):

$$\begin{aligned} H^{\mathrm{FE-CT}} = \sum_n \Big[& t_{\mathrm{e}}(a_n^\dagger c_{n,+1} + a_n^\dagger c_{n,-1}) + \\ & + t_{\mathrm{h}}(a_n^\dagger c_{n+1,-1} + a_n^\dagger c_{n-1,+1}) + \mathrm{h.c.} \Big] . \end{aligned} \tag{148}$$

Thus, the extended Holstein Hamiltonian for Frenkel and CT excitons becomes

$$H_{\mathrm{Hol}}^{\mathrm{FCT}} = H_{\mathrm{Hol}}^{\mathrm{FE}} + H^{\mathrm{CT}} + H^{\mathrm{CT-ph}} + H^{\mathrm{FE-CT}} . \tag{149}$$

This Hamiltonian corresponds to the dimer Hamiltonian used in Ref. [15].

A natural extension of the basis states $|n\underline{\nu}\rangle$ from Eq. (102) is obtained by including the new electronic degree of freedom f. The value $f = 0$ shall denote the former Frenkel exciton basis states:

$$[\, |nf\underline{\nu}\rangle \,]_{f=0} \equiv |n\underline{\nu}\rangle . \tag{150}$$

A Lang-Firsov-type basis for CT states ($f = \pm 1$) follows in complete analogy to Eqs. (102) and (103) for the Frenkel excitons:

$$[\, |nf\underline{\nu}\rangle \,]_{f=\pm 1} \equiv c_{n,f}^\dagger |o_{\mathrm{el}}\rangle \times B_{nf\nu}^\dagger |o_{\mathrm{vib}}\rangle , \tag{151}$$

with

$$\begin{aligned} B_{nf\nu}^\dagger \quad \equiv \quad & \underbrace{\frac{1}{\sqrt{\nu_0!}}(b_n^\dagger - g_{\mathrm{h}})^{\nu_0} \cdot \mathrm{e}^{-\frac{g_{\mathrm{h}}^2}{2}} \mathrm{e}^{g_{\mathrm{h}} b_n^\dagger}}_{g_{\mathrm{h}}\text{-disp. on } n} \times \underbrace{\frac{1}{\sqrt{\nu_f!}}(b_{n+f}^\dagger - g_{\mathrm{e}})^{\nu_f} \cdot \mathrm{e}^{-\frac{g_{\mathrm{e}}^2}{2}} \mathrm{e}^{g_{\mathrm{e}} b_{n+f}^\dagger}}_{g_{\mathrm{e}}\text{-disp. on } n+f} \\ & \times \underbrace{\prod_{m \neq 0,f} \frac{1}{\sqrt{\nu_m!}}(b_{n+m}^\dagger)^{\nu_m}}_{\text{undisp. otherwise}} . \end{aligned} \tag{152}$$

Here, $b_n^\dagger - g_{\mathrm{h}}$ creates phonons in the g_h displaced potential at the hole position n and $b_n^\dagger - g_{\mathrm{e}}$ creates phonons in the g_e-displaced potential at the electron position $n + f$. At all other sites, the vibrational potential is not displaced.

The real-space basis states from Eqs. (150),(151) can again be Fourier-transformed to momentum-space basis states with total momentum k:

$$|kf\underline{\nu}\rangle \equiv \frac{1}{\sqrt{N}} \sum_n \mathrm{e}^{\mathrm{i}kn} |nf\underline{\nu}\rangle . \tag{153}$$

As for the Frenkel problem, the matrix elements of the Frenkel-CT Holstein Hamiltonian (149) can be derived in a straightforward way. The final expressions become lengthy due to various overlap factors and we omit them here. The basis can be reduced to a manageable size by a truncation scheme as for the Frenkel problem. Then, the eigenstates $|\Psi_j(k)\rangle$ at $k = 0$ or $k = \pi$ can again be obtained by standard diagonalization methods for real matrices in the form

$$|\Psi_j(k)\rangle = \sum_{f\underline{\nu}} u_{f\underline{\nu}j}(k)|kf\underline{\nu}\rangle \tag{154}$$

As for the Frenkel exciton problem, the most important property for characterizing an eigenstate $|\Psi_j(k)\rangle$ is its electronic character. Since the states are now constructed from different electronic states (Frenkel and CT), we have to distinguish different electronic characters.

The Frenkel exciton character is given as in Definition (113) by the projection onto a Frenkel exciton:

$$F_{\mathrm{FE}j}(k) = |\langle\Psi_j(k)|a_k^\dagger|o\rangle|^2 \; . \tag{155}$$

Using the decomposition (154) into basis states, the FE character becomes:

$$F_{\mathrm{FE}j}(k) = |\sum_{f\underline{\nu}} u^*_{f\underline{\nu}j}\langle kf\underline{\nu}|a_k^\dagger|o\rangle|^2 \; . \tag{156}$$

The matrix element $\langle kf\underline{\nu}|a_k^\dagger|o\rangle$ is nonzero only for Frenkel-type basis states ($f = 0$). Then, it reduces to the same expression as for the Frenkel-only problem (see Eq. (116)) and we get:

$$F_{\mathrm{FE}j}(k) = \left|\sum_{\underline{\nu}} u^*_{0\underline{\nu}j} S \begin{pmatrix} \nu_0 \\ 0 \end{pmatrix} \prod_{r\neq 0} \delta_{\nu_r,0}\right|^2 \; . \tag{157}$$

For describing the CT character of the states, we use a projection onto the symmetric CT states

$$\tilde{c}^\dagger_{k+}|o\rangle = \frac{1}{\sqrt{2}t_k}\left\{(t_\mathrm{e} + t_\mathrm{h}\mathrm{e}^{+\mathrm{i}k})c^\dagger_{k,+1} + (t_\mathrm{e} + t_\mathrm{h}\mathrm{e}^{-\mathrm{i}k})c^\dagger_{k,-1}\right\}|o\rangle \; ,$$

which were introduced in Eq. (31) for the electronic problem. Then, the CT character becomes

$$\begin{aligned} F_{\mathrm{CT}j}(k) &\equiv |\langle\Psi_j(k)|\tilde{c}^\dagger_{k+}|o\rangle|^2 & (158)\\ &= |\sum_{f\underline{\nu}} u^*_{f\underline{\nu}j}\langle kf\underline{\nu}|\tilde{c}^\dagger_{k+}|o\rangle|^2 \; . & (159)\end{aligned}$$

The matrix element can be decomposed into an electronic part and a vibrational overlap factor:

$$\begin{aligned}\langle kf\underline{\nu}|\tilde{c}^\dagger_{k+}|o\rangle &= \frac{1}{\sqrt{2}t_k}\left\{(t_\mathrm{e} + t_h\mathrm{e}^{\mathrm{i}k})\delta_{f,+1} + (t_\mathrm{e} + t_h\mathrm{e}^{-\mathrm{i}k})\delta_{f,-1}\right\}\\ &\quad\times\langle\tilde{B}^\dagger_{nf\underline{\nu}}o_{\mathrm{vib}}|o_{\mathrm{vib}}\rangle \; .\end{aligned}$$

Naturally, the electronic part of the projection onto the symmetric CT state becomes zero for a pure FE basis state ($f = 0$). The vibrational overlap factor contains two overlap terms for the electron and hole displaced lattice site:

$$\langle \tilde{B}^{\dagger}_{nf\underline{\nu}} o_{\mathrm{vib}} | o_{\mathrm{vib}} \rangle = S_{g_{\mathrm{h}}} \begin{pmatrix} \nu_0 \\ 0 \end{pmatrix} \times S_{g_{\mathrm{e}}} \begin{pmatrix} \nu_f \\ 0 \end{pmatrix} \times \prod_{r \neq 0, f} \delta_{\nu_r, 0} \; .$$

At the important special points $k = 0$ and $k = \pi$, the electronic factor simplifies greatly and the projection of the basis state becomes for both k:

$$\langle k f \underline{\nu} | \tilde{c}^{\dagger}_{k+} | o \rangle = \frac{1}{\sqrt{2}} \times S_{g_{\mathrm{h}}} \begin{pmatrix} \nu_0 \\ 0 \end{pmatrix} \times S_{g_{\mathrm{e}}} \begin{pmatrix} \nu_f \\ 0 \end{pmatrix} \times \prod_{r \neq 0, f} \delta_{\nu_r, 0} \; . \tag{160}$$

Inserting this matrix element into Eq. (159) gives the formula for the CT character of a numerically obtained eigenstate.

The transition dipole can be discussed similarly to the Frenkel-only case (see Eq. (118)), and one obtains a Frenkel and a CT transition dipole component as in the electronic problem (see Eq. (46)). For the experimental interpretation, we will later assume that the CT component is a negligible contribution ($p_{\mathrm{CT}} \ll p_{\mathrm{FE}}$), and then the squared transition dipole becomes proportional to the Frenkel character at $k = 0$ as in Eq. (118):

$$|\vec{P}_j|^2 \approx |\vec{P}_{\mathrm{FE}j}|^2 = \delta_{k,0} N \vec{p}^{\,2}_{\mathrm{FE}} F_{\mathrm{FE}j}(k) \; . \tag{161}$$

A representative calculation is shown in Figs. 15 and 16 for the parameters $J = 0.5\hbar\omega$, $g = 1$, $D = 0$, $t_{\mathrm{e}} = t_{\mathrm{h}} = 0.5\hbar\omega$. The Frenkel part of this parameter set corresponds to the calculation in Fig. 11. The basis cut-off vector for the phonon-space was $|\underline{\nu}\rangle^{\max} = |1234\tilde{5}4321\rangle$ with $\nu_{\mathrm{tot}}^{\max} = 5$, resulting in 4332 basis states. An additional CT state is assumed at resonance with the Frenkel state ($D = 0$). The charge-transfer integrals t_{e} and t_{h} are chosen equal to the Frenkel hopping integral to give an illustration for strong Frenkel-CT mixing.

For the electron and hole coupling parameters, we used $g_{\mathrm{e}} = g_{\mathrm{h}} = g/\sqrt{2}$, which corresponds to equal relaxation energy for the CT state and the Frenkel exciton. In contrast to the Frenkel exciton-phonon coupling constant g, g_{e} and g_{h} are not easily accessible since absorption spectra of the ions would be needed. Alternatively, one might use quantum chemical calculations or at least qualitative arguments: Perylene's π-system is alternant. Simple Hückel theory then gives equal and opposite charges in the cation and anion, with half-filled HOMO and LUMO, respectively, while both are half-filled in the excited state. We have $g_{\mathrm{e}} = g_{\mathrm{h}} = g/2$ for noninteracting electrons. The Pariser-Parr-Pople model of interacting π-electrons yields $g_{\mathrm{e}} = g_{\mathrm{h}}$ for systems with electron-hole symmetry. The bond order changes and relaxation energy of the singlet excitation in anthracene or trans-stilbene are now approximately half that of the triplet, which in turn is comparable to the relaxation energy of dication or dianion [82, 83]. Our initial choice of equal relaxation energy for the Frenkel and CT excitation follows the correlated case, although this is a guess and PTCDA does not have e-h symmetry.

At the top of the band ($k = 0$, Fig. 15), the energetic degeneracy and the large charge-transfer integrals lead to a strong mixing of Frenkel and CT states throughout the whole spectrum. The overall distribution of the spectral weights gives more Frenkel character to the higher

states as a result of the positive J. The FE character in Fig. 15 should be compared to the Frenkel-only problem from Fig. 11. In the Frenkel-only problem, the lowest state gave rise to a single peak in the broadened spectrum at $E \approx 0$. This peak is now split into two well separated peaks at $E \approx -1\hbar\omega$ and $E \approx 0$. In such a way, strong mixing with CT states can add new features to the absorption spectrum even if their intrinsic transition dipoles are zero ($\vec{p}_{\mathrm{CT}} = 0$) as it was discussed for the electronic problem in Section 2.

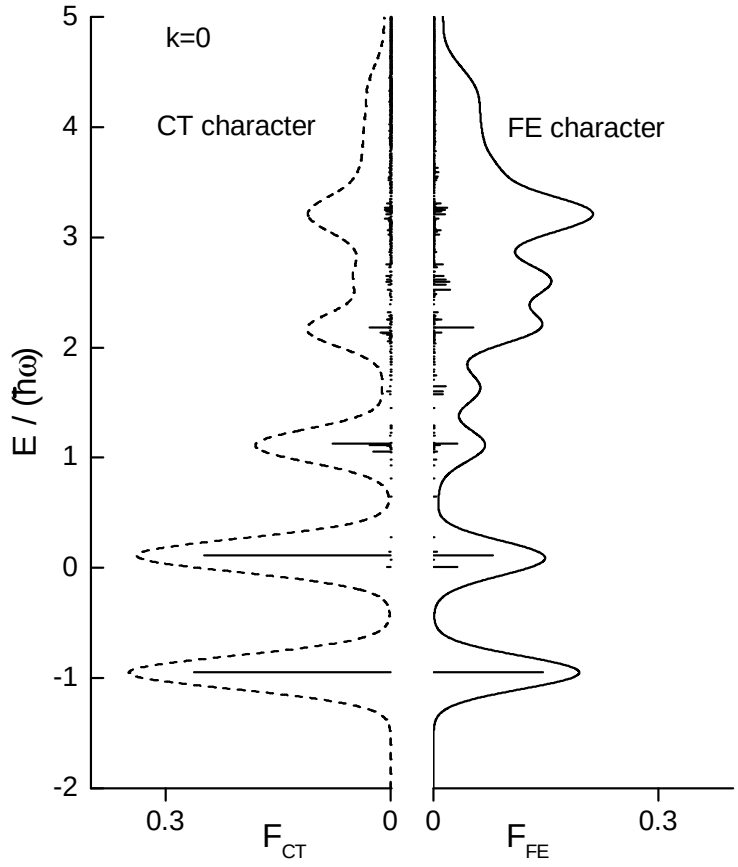

Figure 15:
Eigenstates of the extended Holstein model for Frenkel-CT mixing (149) at total momentum $k = 0$. Parameters: $J = 0.5\hbar\omega$, $g = 1$, $D = 0$, $t_{\mathrm{e}} = t_{\mathrm{h}} = 0.5\hbar\omega$, $g_{\mathrm{e}} = g_{\mathrm{h}} = 1/\sqrt{2}$. The Frenkel parameters and the illustration correspond to Fig. 11. F_{FE} shows the spectral weights (Frenkel character) of the Frenkel-part, F_{CT} shows the spectral weights of the symmetric CT part. The broadened spectra are both normalized to an area of $0.5\hbar\omega$.

At the bottom of the band ($k = \pi$, Fig. 16), the symmetry of the CT integrals ($t_{\mathrm{e}} = t_{\mathrm{h}}$) in this special case decouples the electronic Frenkel and CT states (cf. discussion below Eq. (39)).

Therefore, the electronic character of all states is either purely Frenkel or purely CT. Only some indirect mixing is introduced by the phonon part of the Hamiltonian, which mainly affects the vibronic structure of the CT-character states.

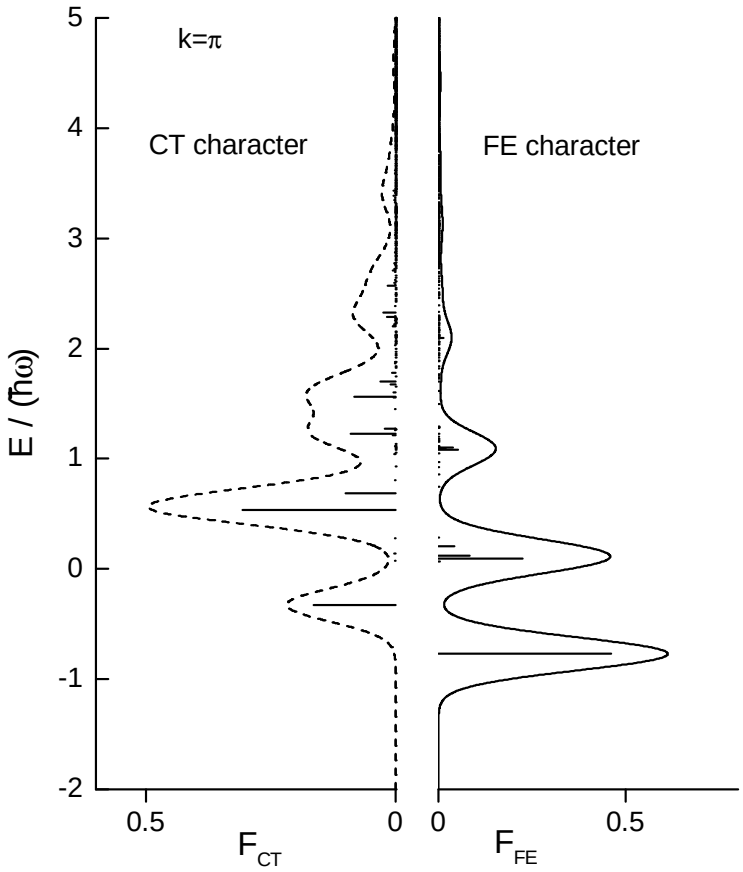

Figure 16:
Eigenstates of the extended Holstein model for Frenkel-CT mixing (149) at total momentum $k = \pi$. Parameters as in Fig. 15. Because of $t_\mathrm{e} = t_\mathrm{h}$, the electronic FE and CT states do not mix and all eigenstates have either pure FE or pure CT character.

4 Applications and consequences for quantum confinement

4.1 Description of PTCDA-derivatives

In Section 3.8, the energies E_j and transition dipoles P_j (Eq. (161)) of the eigenstates of the one-dimensional Holstein problem for mixed Frenkel-CT states were obtained. These quantities are essential but not yet sufficient for the description of a real absorption spectrum of a quasi-one-dimensional molecular crystal.

We still assume that *all* inter-stack interactions are on a much smaller energy scale than the in-stack interaction J. That means, the energy spectrum of the one-dimensional model is in first approximation not affected. However, the direction of the transition dipoles is determined by the complete three-dimensional crystal structure. In PTCDA and MePTCDI and many other organic crystals, the unit cell contains two non-equivalent molecules. Then, the transition dipoles of the non-equivalent molecules A and B couple and form two Davydov components ($\beta = p, s$) with orthogonal transition dipoles:

$$\vec{P}_{j\beta} = \frac{\vec{P}_j(\mathrm{A}) \pm \vec{P}_j(\mathrm{B})}{\sqrt{2}} \,. \tag{162}$$

For the crystal structure of PTCDA and MePTCDI, the p-direction is given as the crystallographic b axis. The s direction lies approximately in the (102) plane since the molecular planes of both inequivalent molecules are roughly parallel to the (102) plane (within 5° [84] for PTCDA and within 10° for MePTCDI, derived from [85]).

Knowing the transition dipoles per unit cell, the transverse dielectric constant for perturbation by an external light wave polarized along the $\beta = p, s$ directions can be expressed as a sum over the excited states (cf. e.g. [86, 4]):

$$\epsilon^0_\beta(E) = 1 + \frac{8\pi}{v} \sum_j \frac{\vec{P}^2_{j\beta} E_j}{E_j^2 - E^2 - \mathrm{i}\hbar\Gamma E} \,. \tag{163}$$

Here, v is the volume of the unit cell and Γ^{-1} the life time of the excited states. Furthermore, the energies now have to be taken as the absolute energies with respect to the total ground state. Thus, the excitation energy E_{00} of our reference state (zero-phonon state of the molecular limit) has to be included.

Equation (163) is rigorous for any quantum system if *all* excited states are included. However, we are considering only the lowest electronic excitation. Therefore, we include the contribution of the higher states (mixing of molecular configurations) by using a phenomenologically modified formula for the dielectric function:

$$\epsilon_\beta(E) = \epsilon^{\mathrm{bg}}_\beta + \frac{8\pi}{v} \sum_j \frac{(f^{\mathrm{bg}}_\beta \vec{P}_{j\beta})^2 E_j}{E_j^2 - E^2 - \mathrm{i}\hbar\Gamma E} \,. \tag{164}$$

Here, $\epsilon^{\mathrm{bg}}_\beta$ is a background dielectric constant that represents the value of $\epsilon_\beta(0)$ corresponding to a crystal in which the considered lowest electronic excitation would not exist. f^{bg}_β is a

screening factor describing the modification of the acting field by the higher transitions. Furthermore, the higher transitions will modify the Frenkel exciton hopping integral J and thereby all the eigenstates of the system. Since we treat J as an effective fitting parameter anyway, the effect of the higher transitions onto J is not important here but should be remembered in any microscopic interpretation of J. Such a background modification of the dielectric function was discussed for a simple model system of one purely electronic Frenkel exciton in a cubic crystal in Ref. [5]. In our general case, the effect of the higher transitions represented in the background parameters is also anisotropic in nature.

The dielectric function (164) includes a Lorentzian broadening of the individual eigenstates due to a finite lifetime Γ^{-1}. In a typical situation, however, there are several other sources of a much larger broadening: (i) coupling to further low energy vibrations, (ii) splitting of the single effective vibrational mode, which actually consists of several nearly degenerate modes, and (iii) inhomogeneous broadening. To account for all these effects empirically, we replace each eigenstate of the Holstein model $|\Psi_j\rangle$ by a Gaussian distribution of states with standard deviation σ_j as e.g. done in Ref. [87]. The individual broadenings σ_j have no microscopic meaning and should be seen as no more than a convenient tool to compare the spectrum from the eigenstates of the Holstein model to an experimental spectrum. Practically, we assigned constant values of σ_j for 4 separate regions of the spectrum in order to have only 4 different broadening parameters. The individual Lorentzian linewidth is assumed to be much smaller than the σ_j and does not contribute anymore.

From the complex dielectric function (164), the complex refractive index $(n + \mathrm{i}\kappa)^2 = \epsilon$ and the absorption coefficient $\alpha = 2E/(\hbar c)\kappa$ can be calculated for the special light waves that propagate perpendicular to the p-s plane and are polarized along the p or s direction. For general directions, the complex rules of crystal optics would have to be considered. We note that the consideration of the *absolute* absorption coefficient is essential for describing the shape of solid state spectra. The microscopic models provide predictions only about the *relative* spectral distribution of the transition dipoles, which determines the shape of the imaginary part $\epsilon_2(E)$ of the dielectric function. The shape of the absorption spectrum $\alpha(E)$ however, is strongly influenced by the variation of the refractive index in the absorption region ($\alpha = E\epsilon_2/(\hbar c n)$) and the variation of n is again determined by the absolute absorption coefficient. Only if α is very small, as typically for spectroscopy of solutions ("dilute limit"), n does not vary and the shape of the absorption spectrum is directly given by the distribution of the spectral weights (exciton characters).

For PTCDA and MePTCDI, it is possible to create vapor-deposited poly-crystalline films with a high preferential orientation such that the (102) crystal planes and thus approximately the p and s directions always lie parallel to the substrate. Only the azimuthal orientation, i.e. the orientation of the p and s directions within the substrate plane, is difficult to control.

In Ref. [41], low-temperature absorption spectra of such vapor deposited films were used to obtain model parameters for the Holstein Hamiltonian by fitting. The values for the monomer were taken from the solution spectra (see Fig. 3): $\hbar\omega = 0.17$ eV and $g = 0.88$ (for both PTCDA and MePTCDI). For the electron and hole coupling parameters, $g_\mathrm{e} = g_\mathrm{h} = g/\sqrt{2}$ was used as in Section 3.8. Furthermore, only one value was used for the charge-transfer integrals:

$t = t_e = t_h$. This simplification is motivated, since for absorption only the value $t_+ = t_e + t_h$ enters the electronic problem (cf. the discussion below Eq. (39)) and since comparable values are suggested by quantum chemical calculations (cf. Ref. [15]). Then, there remain four essential parameters in the model Hamiltonian: Frenkel exciton transfer integral J, CT separation D, charge-transfer integral t, and the zero-point reference energy E_{00} of the molecular limit. It has to be noted that the electronic Frenkel-CT mixing at a given quasi-momentum k is only determined by the absolute value of the transfer integrals (cf. Eqs. (32), (36)) and thus only $|t|$ can be derived. The key-parameters obtained in Ref. [41] are for PTCDA:$J = 42\,\text{meV}$, $D = 97\,\text{meV}$, $|t| = 42\,\text{meV}$, $E_{00} = 2.23\,\text{eV}$, and for MePTCDI:$J = 46\,\text{meV}$, $D = 240\,\text{meV}$, $|t| = 57\,\text{meV}$, and $E_{00} = 2.13\,\text{eV}$.[12]

The structure of the corresponding eigenstate spectrum at $k = 0$ is best visualized by the Frenkel exciton character and the CT character of the states. We illustrate these characters in Figs. 17(b) and 18(b) in the same scheme as in Figs. 15 and 16. In these fits, the composition of the optically active states at $k = 0$ shows a strong mixing of Frenkel and CT excitons. The Frenkel character determines the absorption coefficient α. The comparison of the experimental absorption coefficient and the model fit is given in the panels (a). The characteristic difference between the absorption coefficient spectrum in (a) and the distribution of the Frenkel characters in (b) is entirely caused by the spectral shape of the refractive index n, which becomes small at energies above the major absorption region.

It has to be emphasized that the fitting parameters contain many uncertainties. In particular for PTCDA, the absorption spectrum alone is not specific enough to determine the situation uniquely. Similarly good fits of the experimental spectra can be obtained for different parameter sets with varying degree of CT mixing. Even total neglect of CT states would give a satisfactory fit with a Frenkel transfer integral of 70 meV. Such a value corresponds to the three-dimensional Frenkel exciton model for PTCDA in Ref. [18] with a nearest-neighbor hopping of 82 meV. For MePTCDI, the absorption spectrum has a more characteristic shape with four main peaks. This spectrum can only be fitted within this framework by assuming a strong Frenkel-CT mixing.

The strongest support for the assumption of Frenkel-CT mixing is provided by the interpretation of electro-absorption rather than by linear absorption spectra [15, 17], since a pure Frenkel exciton model would not explain the strong response to electrical fields perpendicular to the molecular planes. In Ref. [17], a three-dimensional version of a Frenkel-CT Hamiltonian (in the molecular vibron approximation) was used to model electro-absorption spectra of PTCDA. The strongest effects were confirmed to arise from the one-dimensional stacks. Hamiltonian parameters could be obtained from fits and also confirmed by microscopic calculations. The essential transfer parameters corresponding to our one-dimensional version were obtained as $J = 180\,\text{meV}$, $D = 130\,\text{meV}$, $t = -55\,\text{meV}$ [17]. These parameters from the electro-absorption model essentially agree with our suggestion for the linear absorption spectra. The largest discrepancy is in the Frenkel exciton transfer integral J, where our smaller value mainly results from the use of a dielectric function.

Apart from the remaining uncertainty about the Frenkel-CT mixing, the obtained charge-

[12] In Ref. [41], the values of t_+ were given.

transfer integrals would imply single-particle bandwidths $4t_\mathrm{e}$, $4t_h$ on the order of no more than 0.2 eV, which is still smaller than the total exciton binding energy. Thus, the qualitative picture is consistent with the approach of a small radius exciton theory (cf. discussion in Section 1).

We will now discuss following Ref. [88] what the proposed model for the absorbing states ($k = 0$) means for the complete exciton band structure. In order to rationalize the k dependencies, we first concentrate on the purely electronic bands shown in Figs. 17(c) and 18(c). As in Section 3.7, the electronic bands are given by the purely electronic parts of the Holstein Hamiltonian (149):

$$H_\mathrm{elec} = H_\mathrm{elec}^\mathrm{FE} + H_\mathrm{elec}^\mathrm{CT} + H_\mathrm{elec}^\mathrm{FE-CT} + g^2\hbar\omega \; . \tag{165}$$

This electronic Hamiltonian corresponds to the electronic problem in Eq. (29), were the resulting bands and characters were visualized in Figs. (4) and (5). As for the Frenkel exciton case in Section 3.7, the Franck-Condon relaxation energy of the molecular zero-phonon state is added because this state defines the reference energy. The electronic bands in the Holstein model proposed for PTCDA and MePTCDI show that the electronic Frenkel character disperses to lower energies as a result of the positive Frenkel exciton hopping integral J. The center of mass of the CT character remains at a constant position since a CT dispersion is not considered in the model. Furthermore, for this special choice of charge-transfer integrals $t_\mathrm{e} = t_\mathrm{h}$, the Frenkel and CT states do not mix at $k = \pi$ (see discussion below Eq. (39)).

The complete vibronic eigenstate structure at $k = \pi$ is shown in Figs. 17(d) (PTCDA) and 18(d) (MePTCDI). As at $k = 0$, the inclusion of exciton-phonon coupling at $k = \pi$ transforms the two electronic states into a broad vibronic spectrum. With the model parameters from the absorption fit, the lowest $k = \pi$ state lies at $E = 2.18$ eV for PTCDA and at $E = 2.06$ eV for MePTCDI.

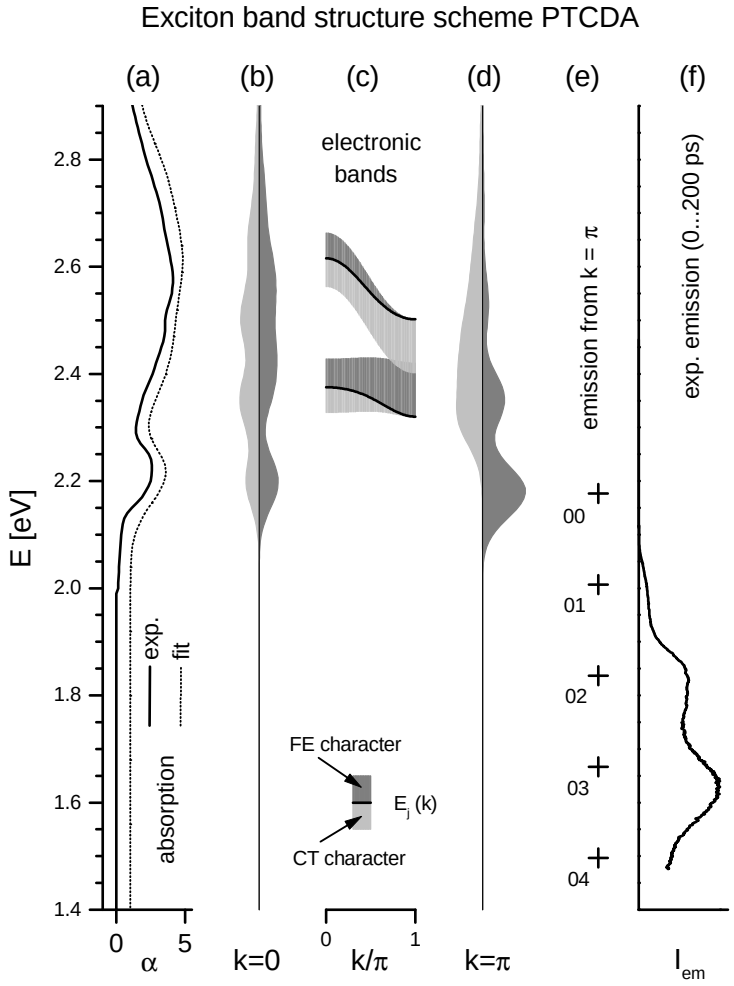

Figure 17:
Suggested exciton band structure in PTCDA and experimental spectra. (a) solid line: experimental low temperature absorption spectrum of thin poly-crystalline film as reported in Ref. [41], α in $10^5\,\mathrm{cm}^{-1}$; dotted line: α from model fit (plotted with offset $+1\times10^5\,\mathrm{cm}^{-1}$). (b) Vibronic model states at $k = 0$. The right side (dark shading) gives the Frenkel character $F_{\mathrm{FE}\,j}$ of the states j from Eq. (156), the left side the CT character $F_{\mathrm{CT}\,j}$ from Eq. (158). Instead of the closely lying individual states, we show a broadened spectrum that summarizes the net contribution. The Frenkel character at $k = 0$ determines the oscillator strength and corresponds to the model absorption spectrum in (a). (c) Electronic bands $E_j(k)$ corresponding to Eq. (165). These bands show the overall dispersion and the k-dependent Frenkel-CT mixing, which result from the electronic interaction parameters. (d) Vibronic model states for $k = \pi$. (e) Emission energies for transitions from the lowest $k = \pi$ state to the vibrational levels of the electronic ground state. The highest transition (00) is strictly dipole-forbidden. (f) transient emission spectrum of a PTCDA single crystal at 10 K (time window $0 \ldots 200\,\mathrm{ps}$), from Ref. [88].

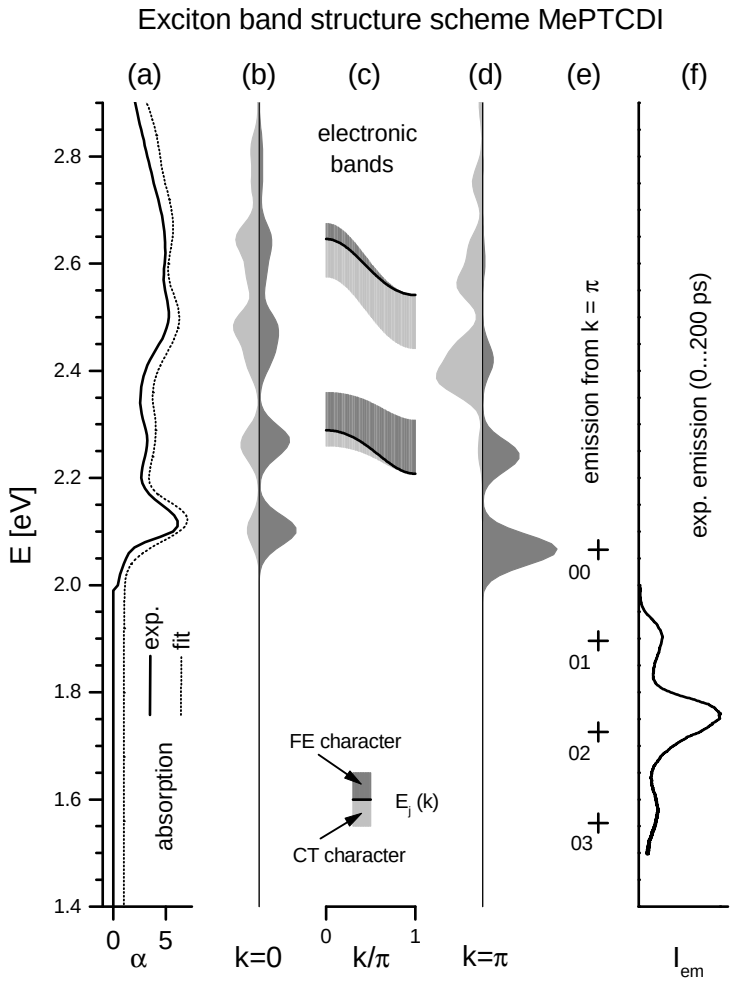

Figure 18:
Suggested exciton band structure in MePTCDI and experimental spectra. For detailed explanations see Fig. 17. The experimental absorption spectrum in (a) is measured at 10 K at a highly oriented poly-crystalline film with polarization parallel to the strong Davydov component (crystallographic b-axis), cf. Ref. [16]. The transient emission spectrum in (f) is measured at 4 K at a single crystal, time window 0 . . . 200 ps, from from Ref. [88].

The band bottom of the exciton band structure is a starting point for the discussion of emission spectra since all photo-excited states will rapidly relax to these lowest states. The transition from these $k = \pi$ states to the total ground state is strictly dipole-forbidden, at least in perfect crystals. However, transitions to $k = \pi$ phonons in the electronic ground state are allowed. We indicate the resulting transition energies (including the forbidden 00-transition) in the panels (e). For a qualitative comparison, these transition energies are compared to transient low-temperature photoluminescence spectra of single crystals in the panels (f) of both figures. The comparison shows that the energetic positions of the 01 and 02 transition do approximately agree with the peaks in the emission spectra. This supports the order of magnitude of the model parameters, especially the relatively small value of the Frenkel hopping J. A larger J, as could be expected from quantum chemical arguments and from models without dielectric function [15, 17], would give a larger separation between the lowest absorption peak and the 01-emission peak.

The assignment of the emission spectra still is very tentative, since the spectra do not show an exact vibronic progression and the decay times of the peaks are slightly different, which becomes much more pronounced at higher temperatures. Furthermore, the emission spectra sensitively depend on the concrete sample configurations, on the considered time scale (up to cw) and on the temperature. This leads to widely varying emission spectra and assignments. It is not clear at this stage to what extent extrinsic defects or further intrinsic effects determine the emission behavior. In particular, a strong coupling to external phonon modes, corresponding to excimer emission, can be expected as an additional effect (cf. the explicit treatment for perylene in Ref. [89]). Such effects might be reasons for the discrepancies, which are particularly pronounced in the lowest PTCDA emission peak. A detailed discussion of time-resolved PTCDA emission spectra was recently given in Refs. [90, 91]. These works are based on a pure Frenkel exciton band structure model within the molecular vibron approximation [18]. The various spectral features and their temperature dependencies are explained by including the small interactions between the non-equivalent molecules, which leads to Davydov splitting of the exciton bands, and by considering vibrational relaxation along several different coordinates.

Since the fine details of the experimental emission spectra are very complex there is a large number of conceivable models for their interpretation. At present, there are not enough tests available that would allow independent confirmation of many model aspects. In particular, the complexity of model assumptions seems to be comparable to the complexity the explained observations. Therefore, it is very desirable to identify basic and unique features in the excited state structure of the considered class of materials. The exciton band structure within a Frenkel-CT-Holstein model provides such a unified framework for the description of absorption spectra and it is a starting point for a discussion of emission spectra and relaxation processes after photo-excitation.

4.2 Inclusion of finite size and quantum confinement effects

Up to here, the treatment of molecular crystals was presented for the case of an infinite chain. Real systems are always finite, and many systems of current interest cover the complete range of

one-dimensional chain lengths starting from a single molecule. For example, thin films consisting of one or just a few monolayers of PTCDA can be prepared by organic molecular beam epitaxy (OMBE) and they can be studied with spectroscopic methods (e.g. [7, 92]). Thus, it is important to know down to which chain length N the picture of an infinite chain is still correct. It is even more important to investigate which qualitatively new effects can occur in finite systems. We will discuss these questions in the framework of the one-dimensional exciton models presented in the previous sections.

The existence of a finite system size N affects all model descriptions at the very beginning. The starting point still is a model Hamiltonian expressed by on-site energies and interaction terms for localized excitations. However, the site index is restricted now ($n = 1 \ldots N$) and the boundary conditions play a major role. Furthermore, the sites are not equivalent anymore and therefore the on-site energies ϵ_{FE} and exciton transfer integrals J might have site-dependent values.

Let us illustrate the effects for the simplest example of the nearest-neighbor Frenkel exciton model from Eq. (16). In a finite chain, it can be written as:

$$H_{\mathrm{NN}}^{\mathrm{FE}}(N) = \sum_{n=1}^{N} \epsilon_{\mathrm{FE}}(n) a_n^\dagger a_n + \sum_{n=1}^{N-1} J(n)(a_n^\dagger a_{n+1} + a_{n+1}^\dagger a_n) \; . \tag{166}$$

In this notation, the boundary conditions are expressed by the index range for the hopping term: Transfer from site $n = 1$ is only possible towards higher indices and transfer from site $n = N$ only towards lower indices. Even if the site-dependence of $\epsilon_{\mathrm{FE}}(n)$ and $J(n)$ is neglected, the boundary conditions in Hamiltonian (166) do not allow the separation into non-mixing subspaces with different quasi-momentum (Eq. (11)). Thus, a general diagonalization scheme has to work with basis states in real space. Even for a Frenkel-CT-Holstein model as in Eq. (149), a numerical diagonalization can be done in real-space along similar lines as presented for the momentum-space basis states, and only the number of basis states increases by a factor N.

The solutions of our example in Eq. (166) for constant $\epsilon_{\mathrm{FE}}(n) = \epsilon_{\mathrm{FE}}$ and $J(n) = J$ are well known (e.g. [93]). The N eigenstates have energies

$$E_j(N) = \epsilon_{\mathrm{FE}} + 2J \cos \frac{\pi j}{N+1} \qquad j = 1, 2, \ldots N \; . \tag{167}$$

The size dependence of the lowest and highest state energy is shown in Fig. 19. The difference between the highest and lowest state corresponds to the exciton bandwidth in the infinite system and it approaches its value $\Delta E = 4J$ for the limit $N \to \infty$. For the dimer ($N = 2$), the bandwidth has already half of its maximum value. This size dependence results entirely from the effect that the exciton is confined in its hopping motion by the system boundaries. Therefore, the effect can be approximately described by the picture of a "particle in a box".

We will illustrate this particle-in-a-box behavior by an alternative approach based on the effective mass approximation (cf. also [94]): In the infinite system, the exciton states for Hamiltonian (166) are entirely characterized by their dimensionless quasi-momentum k and their dispersion relation is (cf. Eq. (20))

$$E_k^{\mathrm{eff}} = \epsilon_{\mathrm{FE}} + 2J \cos k \; . \tag{168}$$

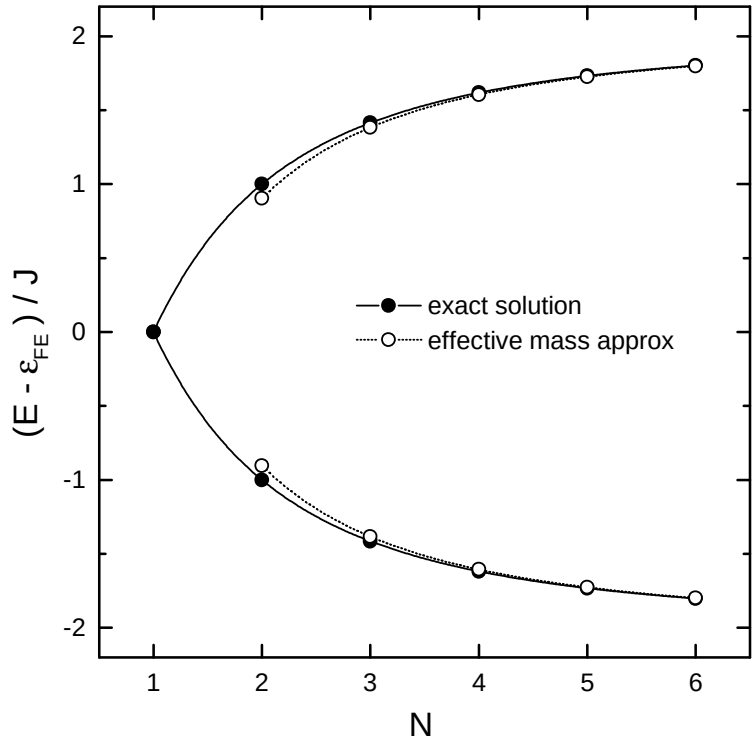

Figure 19:
Size dependence of the highest and lowest Frenkel exciton state in a linear nearest-neighbor hopping model (Eq. (166)) for constant $\epsilon_{\rm FE}$ and J. The "exact solution" shows the state energies from Eq. (167), the "effective mass approximation" shows the band edges from Eq. (171).

The effective mass of the exciton follows as

$$m_{\rm eff}^{-1} = \frac{a^2}{\hbar^2}\frac{\partial^2 E_k^{\rm eff}}{\partial k^2} = -\frac{a^2}{\hbar^2} \times 2J\cos k \quad , \tag{169}$$

where a is the lattice constant. We now treat this exciton as a real particle with mass $m_{\rm eff}$, which is confined within the chain. Thus, the wave function should be zero at the non-available lattice positions $n = 0$ and $n = N+1$. This corresponds to a potential well of size $L = (N+1)a$ with infinitely high boundaries. The ground state energy of the particle in such a well is $\pi^2\hbar^2/(2m_{\rm eff}L^2)$. This ground state energy corresponds to the energy shift $\Delta E^{\rm eff}$ that is induced by the finite system size:

$$\Delta E^{\rm eff} = \frac{\pi^2\hbar^2}{2m_{\rm eff}L^2} \; . \tag{170}$$

From Eqs. (168) and (170), the energy $E_k^{\text{eff}}(N)$ of the confined exciton follows as

$$\begin{aligned} E_k^{\text{eff}}(N) &= E_k^{\text{eff}} + \Delta E^{\text{eff}} \\ &= \epsilon_{\text{FE}} + 2J\cos(k) \times \left(1 - \frac{1}{2}\frac{\pi^2}{(N+1)^2}\right) \end{aligned} \tag{171}$$

We show this energy from the effective mass approximation for $k = 0$ and $k = \pi$ in comparison with the exact energies in Fig. 19. The effective mass approximation works very good even down to a chain length of $N = 2$, where the deviation is still only $J(\pi^2 - 9)/18 = 0.048J$.

The comparison in Fig. 19 illustrates for the case of the one-dimensional Frenkel exciton: The effect of the finite system size can approximately be described by treating the exciton as a particle in a box, where the effective mass of the particle is given by the dispersion relation. This approach can be extended for the case that the exciton has a more complicated structure, i.e., if the localized basis states have additional internal degrees of freedom (cf. Section 2.1). Even in this case, the translational symmetry of the infinite system assures that the eigenstates can be classified by their total momentum k and further quantum numbers for their internal structure. The dispersion $E(k)$ of a given state determines its effective mass and can thereby cause a quantum size effect as given by Eq. (170). However, this simple picture obviously breaks down if the internal structure of the exciton state is affected by changes of the system size. Such a change must occur if the internal structure is related to a characteristic size (quantum length) of the exciton and the system size becomes comparable to or smaller than this intrinsic quantum length.

For the simple Frenkel exciton in Fig. 19, there is no internal degree of freedom and therefore no intrinsic quantum length. For the Merrifield model (see Eq. (24)) of one electron and one hole on a one-dimensional chain, the eigenstates do have an internal structure and a characteristic length is given by the mean separation between electrons and holes. For the Holstein model (see Eq. (101)), an internal structure is introduced by the structure of the phonon cloud and a characteristic quantum length follows from the extension of the lattice distortion $\langle \lambda_m \rangle$ around the exciton (cf. Fig. 11). In all such cases with internal structure, one can therefore distinguish two finite size effects: (I) A *quantum size effect* according to Eq. (170) that results from the confinement of the center-of-mass motion and (II) a *quantum confinement effect* that results from a confinement of the internal exciton structure.

A mathematically explicit version of the heuristic distinction between quantum size and quantum confinement effects is shown by Kayanuma for three dimensional Wannier-Mott excitons [95]. In this case, the intrinsic quantum length of the exciton is the electron-hole separation R. Kayanuma shows that for a system size $L \gg R$ ("weak confinement" in the classification of Kayanuma), the size dependence of the eigenstate energies is given by Eq. (170). For $L \lessapprox R$ ("strong confinement"), the internal structure of the exciton is drastically changed, and the eigenstates are rather characterized by the confinement of the single particles.

From this discussion we can conclude that the internal structure, more specifically the intrinsic quantum length R, of exciton states is crucial for estimating the effects of a finite system size. In the framework of the Frenkel-charge-transfer Holstein model (Eq. (149)) from

this chapter, there are three effects that give rise to an intrinsic quantum length:

(I) Because of the CT states involved, one has a non-trivial electron-hole separation. However, since only nearest-neighbor CT states are included, this electron-hole separation has an upper limit of one lattice constant and quantum-confinement is of very limited interest.

(II) In a finite system, the subtle boundary conditions for CT states can lead to the appearance of Tamm-like surface states [96]. These surface states have a decay length which is entirely given by the parameters in the Hamiltonian and which can be in the order of many lattice constants. Thus, this decay length has the nature of an intrinsic quantum length. If the finite chain becomes smaller than the quantum length of the surface states, their internal structure is changed, i.e. quantum-confinement occurs [97, 98].

(III) Exciton-phonon coupling leads to the appearance of phonon clouds, i.e., the exciton is surrounded by a lattice displacement $\langle \lambda_m \rangle$ (see Eq. (125)), which is illustrated for specific examples in Figs. 11 and 13. For the scenario presented in Section 4.1, i.e., for the strongly coupled internal vibrations in PTCDA derivatives, the phonon clouds have extensions not much larger than one lattice constant. However, one might also consider phonon modes which are not that strongly coupled. With respect to such modes, one has the situation of strong electronic coupling, and the approach of localized phonon clouds from Section 3 is not appropriate. Now, one can use the continuum model for large phonon clouds described by Rashba [99]. This situation was studied for Frenkel excitons by Agranovich et al. in Ref. [100]. The intrinsic quantum length (extension of the phonon cloud) in this case is $R = Ja/(2g^2\hbar\omega)$,[13] and R can easily become large for small coupling constants or small phonon energies. This results in quantum confinement effects, which are quantitatively discussed in Ref. [100].

In a realistic finite system, not only the quantum-size effect according to Eq. (170) and the quantum confinement effects (I)-(III) from above may occur, but also the possibility of site-dependent on-site and interaction energies should be considered as in Eq. (166). However, it is very difficult to predict trends for the dependencies $\epsilon_{\mathrm{FE}}(n)$, $\epsilon_{\mathrm{CT}}(n)$, $J(n)$, $t_{\mathrm{e/h}}(n)$.

A strong effect is expected for the variation of the on-site energy of the Frenkel exciton. For this case, at least some knowledge is available for the lowest transition in anthracene. The total gas-to-crystal shift is on the order of $2500\,\mathrm{cm}^{-1}$ ($0.3\,\mathrm{eV}$),[14] whereas surface states were experimentally identified with energy differences to the bulk states of about $200\,\mathrm{cm}^{-1}$ ($20\,\mathrm{meV}$) [101]. In Ref. [101], the energetic separation was interpreted as being mainly due to the gas-to-crystal shift of the molecules from the outermost surface layer. The shift for the next (sub-surface) layer was already considerably smaller. Thus, one can assume that $\epsilon_{\mathrm{FE}}(n)$ is almost constant for $n > 1$, and even that the change at $n = 1$ is by far not as large as the upper limit given by the gas-to-crystal shift.

The on-site energy ϵ_{CT} of the CT states is strongly affected by the electronic polarization of the surrounding molecules. Thus, close to the surface, strong changes of $\epsilon_{\mathrm{CT}}(n)$ can be expected. Modern microscopic calculations of polarization energies seem to allow estimations for this effect using a methodology that has already been applied for the polarization energy of

[13] This follows from Eq. (26) of Ref. [100]. Note that there the meaning of g is different.

[14] The shift is given as the difference of the vapor-phase transition ($27688\,\mathrm{cm}^{-1}$ taken from [101]) and the center of the $\parallel b$ and $\perp b$ polarized crystal transitions (values taken from [4]).

ions in finite systems [102].

The Frenkel transfer integral J is also strongly influenced by dielectric screening from the surrounding molecules and therefore can be expected to change significantly close to the surface. Thus, one has to cope with a variety of different effects and unknown parameters and it is not surprising that even for the experimentally well investigated case of PTCDA a coherent picture has not been presented yet. Shifts in the absorptions spectra of PTCDA/NTCDA multilayer structures [103] were initially interpreted as quantum-confinement (in the strict sense discussed above) of Wannier-Mott excitons. However, a pure Wannier-Mott exciton picture seems not to be adequate for PTCDA (see discussion in Section 4.1). An alternative interpretation for the shifts is given in terms of a varying contribution from the gas-to-crystal shift at the surface by Agranovich et al. in Ref. [104]. The situation becomes even more complicated due the possible mixture of different crystal phases in thin layers [105]. Thus, a clear identification of quantum size and quantum confinement effects in PTCDA-related quasi-one-dimensional crystals requires considerably more information than currently available. In particular, one has to find ways in which the various contributing effects can be separately estimated from independent theoretical or experimental methods.

5 Conclusion

In this chapter, we illustrated the application of basic exciton models for describing optical spectra of quasi-one-dimensional molecular crystals. We concentrated on two essential effects: Mixing of electronic Frenkel and charge-transfer excitations and strong coupling to one internal molecular vibration. For these models, we gave a comprehensive and self-contained discussion with emphasis on illustrational examples.

In Section 2, the electronic states were described as one-dimensional collective excitations consisting of molecular excitations (Frenkel excitons) and nearest-neighbor charge-transfer excitations. This special case of the more general Merrifield model [32] seems to be suitable for molecular crystals that form stacks with close coplanar arrangement of the molecular planes. The essential parameters are given by the nearest-neighbor Frenkel transfer integral J, the separation of the CT states from the molecular excitation D and the electron and hole transfer integrals t_e and t_h. The interplay of these parameters is illustrated in terms of band structure plots showing the two resulting bands and their mixed character. The mixing of two electronic states can lead to two peaks in the absorption spectra — even if the CT states have a vanishing intrinsic transition dipole moment. This effect is one probable candidate for the explanation of broadening or peak-splitting in absorption spectra of quasi-one-dimensional crystals. An alternative explanation would be Davydov splitting due to Frenkel-type interactions of non-equivalent molecules. This Davydov splitting, however, is expected to be significantly smaller [16]. We also discussed the qualitative nature of the intrinsic CT transition dipole.

Section 3 considers strong coupling of the electronic excitations to internal molecular vibrations, which is a typical feature in many molecules of current interest. This coupling is most obvious in the vibronic progression in absorption spectra of isolated molecules. In a one-dimensional crystal, even the simplest model description for such exciton-phonon coupling (Holstein Hamiltonian) leads to a complicated many-particle problem that cannot be generally solved. Here, we describe a numerical approach that is conceptually simple and allows the calculation of optical spectra by standard numerical diagonalization tools. This approach is appropriate for weak electronic coupling and exciton-phonon coupling constants in the order of one. This means in other words: The isolated molecules show a pronounced vibronic progression (0-0 and 0-1 peak of comparable height) and the spectral changes in the crystal concern only an energy range comparable to the range of the vibronic progression.

In Section 4, we outlined the application of the basic models to experimental spectra of thin organic films. The first step is a realistic description of bulk optical constants. The capabilites and limitations of the minium models are illustrated for spectra of two archetypal perylene derivatives. For very thin layers, a number of additional finite size and quantum confinement effects can occur. We qualitatively discussed the nature of such effects in the framework of our minimum model. A general distinction can be made on the basis of the internal exciton structure. If, as in the pure electronic Frenkel case, the exciton has no internal structure, the finite system size leads to a simple particle-in-a-box behavior. This quantum size effect is still the leading effect if the system size is larger than any intrinsic length scale of a more complicated exciton. As soon as the system size affects the internal structure, we speak of

quantum confinement. Intrinsic quantum lengths responsible for quantum confinement can occur in the idealized problem in two ways: (I) The electronic problem for Frenkel and CT states can lead to surface states with a finite decay length. (II) Exciton-phonon coupling leads to phonon clouds with finite extension around the electronic excitation. Further effects are expected to arise from a site dependent modification of the Hamiltonian parameters.

At the present stage, there is still no general agreement about the specific interpretation of experimental spectra in terms of microscopic exciton models. Even in the case of bulk spectra, the available information is typically not sufficient for a unique parameterization. Furthermore, a comparison between different interpretations is often difficult since typically different aspects are explained by different models. More certainty can be expected if not just single materials are studied but general trends are investigated and described by a common framework.

6 Acknowledgments

Most of the material reviewed here is a result of fruitful collaborations that I enjoyed during the past years. The aspects of mixed Frenkel-CT excitons in Section 2 were developed together with Vladimir M. Agranovich, Karin Schmidt and Karl Leo, and the exciton-phonon problem in Section 3 was investigated together with Zoltan G. Soos. I am very thankful to these collaborators for their help and inspiration. To K. Schmidt I am also indebted for discussions on quantum confinement and for providing Fig. 7. I want to thank all members of the Institut für Angewandte Photophysik at Technische Universität Dresden for their support. Financial support by Deutsche Forschungsgemeinschaft is gratefully acknowledged.

References

[1] C. Kittel, Introduction to Solid State Physics, John Wiley & Sons, New York, 1996.

[2] E. V. Tsiper and Z. G. Soos, *Phys. Rev. B* **64** (2001) 195124.

[3] D. P. Craig and S. H. Walmsley, Excitons in Molecular Crystals, W. A. Benjamin, Inc., New York, 1968.

[4] A. S. Davydov, Theory of Molecular Excitons, Plenum Press, New York, 1971.

[5] V. M. Agranovich and M. D. Galanin, Electronic Excitation Energy Transfer in Condensed Matter, North-Holland, Amsterdam, 1982.

[6] D. W. Schlosser and M. R. Philpott, *J. Chem. Phys.* **77** (1982) 1969.

[7] S. R. Forrest, *Chem. Rev.* **97** (1997) 1793.

[8] E. Umbach, K. Glöckler, and M. Sokolowski, *Surface Science* **402-404** (1998) 20.

[9] C. W. Tang, *Appl. Phys. Lett.* **48** (1986) 183.

[10] P. Peumans, V. Bulović, and S. R. Forrest, *Appl. Phys. Lett.* **76** (2000) 2650.

[11] D. Meissner and J. Rostalski, *Synth. Met.* **121** (2001) 1551.

[12] P. M. Kazmaier and R. Hoffmann, *J. Am. Chem. Soc.* **116** (1994) 9684.

[13] E. I. Haskal, Z. Shen, P. E. Burrows, and S. R. Forrest, *Phys. Rev. B* **51** (1995) 4449.

[14] V. Bulović, P. E. Burrows, S. R. Forrest, J. A. Cronin, and M. E. Thompson, *Chem. Phys.* **210** (1996) 1.

[15] M. H. Hennessy, Z. G. Soos, R. A. Pascal Jr., and A. Girlando, *Chem. Phys.* **245** (1999) 199.

[16] M. Hoffmann, K. Schmidt, T. Fritz, T. Hasche, V. M. Agranovich, and K. Leo, *Chem. Phys.* **258** (2000) 73.

[17] G. Mazur, P. Petelenz, and M. Slawik, *J. Chem. Phys.* **118** (2003) 1423.

[18] I. Vragović, R. Scholz, and M. Schreiber, *Europhys. Lett.* **57** (2002) 288.

[19] M. Sadrai, L. Hadel, R. R. Sauers, S. Husain, K. Krogh-Jespersen, J. D. Westbrook, and G. R. Bird, *J. Phys. Chem.* **96** (1992) 7988.

[20] M. Adachi, Y. Murata, and S. Nakamura, *J. Phys. Chem.* **99** (1995) 14240.

[21] G. Klebe, F. Graser, E. Hädicke, and J. Berndt, *Acta Cryst.* **B45** (1989) 69.

[22] V. M. Agranovich, Theory of Excitons, Nauka, Moscow, 1968 (in Russian).

[23] J. Frenkel, *Phys. Rev.* **37** (1931) 17.

[24] J. Frenkel, *Phys. Rev.* **37** (1931) 1276.

[25] A. S. Davydov, *Zh. Eksperim. i Teor. Fiz.* **18** (1948) 210.

[26] D. P. Craig, *J. Chem. Soc.* (1955) 2302.

[27] V. Agranovich, *Fizika Tverdogo Tela* **3** (1961) 811 [Sov. Phys. - Solid State 3(1961), 592].

[28] V. M. Agranovich and Y. V. Konobeev, *phys. stat. sol.* **27** (1968) 435.

[29] D. Haarer and M. R. Philpott, 'Excitons and polarons in organic weak charge transfer crystals', in: V. M. Agranovich and R. M. Hochstrasser, (Eds.), Spectroscopy and Excitation Dynamics of Condensed Molecular Systems, North-Holland, Amsterdam, 1983, pp. 27–82, Chapter 2.

[30] Z. G. Soos, *Ann. Rev. Phys. Chem.* **25** (1974) 121.

[31] L. E. Lyons, *J. Chem. Soc.* (1957) 5001.

[32] R. E. Merrifield, *J. Chem. Phys.* **34** (1961) 1835.

[33] J. P. Hernandez and S.-I. Choi, *J. Chem. Phys.* **50** (1969) 1524.

[34] W. L. Pollans and S.-I. Choi, *J. Chem. Phys.* **52** (1970) 3691.

[35] L. Sebastian and G. Weiser, *Chem. Phys.* **61** (1981) 125.

[36] L. Sebastian, G. Weiser, G. Peter, and H. Bässler, *Chem. Phys.* **75** (1983) 103.

[37] P. Petelenz, M. Slawik, K. Yokoi, and M. Z. Zgierski, *J. Chem. Phys.* **105** (1996) 4427.

[38] M. Slawik and P. Petelenz, *J. Chem. Phys.* **107** (1997) 7114.

[39] M. Slawik and P. Petelenz, *J. Chem. Phys.* **111** (1999) 7576.

[40] P. J. Bounds, P. Petelenz, and W. Siebrand, *Chem. Phys.* **63** (1981) 303.

[41] M. Hoffmann and Z. G. Soos, *Phys. Rev. B* **66** (2002) 024305.

[42] A. Szabo and N. S. Ostlund, Modern Quantum Chemistry, Dover Publications, Inc., Mineola, New York, 1996.

[43] R. S. Mulliken, *J. Amer. Chem. Soc.* **74** (1952) 811.

[44] R. S. Mulliken and W. B. Person, Molecular Complexes. A Lecture and Reprint Volume, Wiley-Interscience, New York, 1969.

[45] H. Haken and H. C. Wolf, Molekülphysik und Quantenchemie, Springer-Verlag, Berlin, 1994.

[46] D. B. Fitchen, 'Zero-phonon transitions', in: W. Fowler (Ed.), Physics of Color Centers, Academic Press, New York, 1968, pp. 294–350, , Chapter 5.

[47] V. L. Broude, E. I. Rashba, and E. F. Sheka, Spectroscopy of Molecular Excitons, Springer-Verlag Berlin, 1985.

[48] H. Haken, Quantum Field Theory of Solids, North Holland, Amsterdam, 1976.

[49] T. Holstein, *Ann. Phys.* **8** (1959) 325.

[50] T. Holstein, *Ann. Phys.* **8** (1959) 343.

[51] J. Appel, 'Polarons', in: F. Seitz, D. Trunbull, and H. Ehrenreich (Eds.), Solid State Physics. Advances in Research and Applications, Vol. 21, Academic Press, New York, 1968, pp. 193–391, , Chapter 3.

[52] M. I. Klinger, Problems of Linear Electron (Polaron) Transport Theory, in: Semiconductors, Pergamon Press, Oxford, 1979.

[53] H. Böttger and V. V. Bryskin, Hopping Conduction in Solids, VCH Weinheim, 1985.

[54] E. A. Silinsh and V. Čápek, Organic Molecular Crystals. Interaction, Localization, and Transport Phenomena, AIP Press, New York, 1994.

[55] D. R. Yarkony and R. Silbey, *J. Chem. Phys.* **67** (1977) 5818.

[56] P. O. J. Scherer, E. W. Knapp, and S. F. Fischer, *Chem. Phys. Lett.* **106** (1984) 191.

[57] Y. Zhao, D. W. Brown, and K. Lindenberg, *J. Chem. Phys.* **106** (1997) 5622.

[58] A. H. Romero, D. W. Brown, and K. Lindenberg, *Phys. Rev. B* **60** (1999) 4618.

[59] A. H. Romero, D. W. Brown, and K. Lindenberg, *Phys. Rev. B* **60** (1999) 14080.

[60] A. H. Romero, D. W. Brown, and K. Lindenberg, *Phys. Rev. B* **59** (1999) 13728.

[61] A. H. Romero, D. W. Brown, and K. Lindenberg, *J. Lum.* **83-84** (1999) 147.

[62] A. S. Alexandrov, V. V. Kabanov, and D. K. Ray, *Phys. Rev. B* **49** (1994) 9915.

[63] G. Wellein, H. Röder, and H. Fehske, *Phys. Rev. B* **53** (1996) 9666.

[64] G. Wellein and H. Fehske, *Phys. Rev. B* **56** (1997) 4513.

[65] G. Wellein and H. Fehske, *Phys. Rev. B* **58** (1998) 6208.

[66] J. Bonča, S. A. Trugman, and I. Batistić, *Phys. Rev. B* **60** (1999) 1633.

[67] H. De Raedt and A. Lagendijk, *Phys. Rev. Lett.* **49** (1982) 1522.

[68] H. De Raedt and A. Lagendijk, *Phys. Rev. B* **27** (1983) 6097.

[69] H. De Raedt and A. Lagendijk, *Phys. Rev. B* **30** (1984) 1671.

[70] P. E. Kornilovitch and E. R. Pike, *Phys. Rev. B* **55** (1997) R8634.

[71] E. Jeckelmann and S. R. White, *Phys. Rev. B* **57** (1998) 6376.

[72] M. R. Philpott, *J. Chem. Phys.* **54** (1971) 111.

[73] R. E. Merrifield, *Radiation Research* **20** (1963) 154.

[74] P. O. J. Scherer and S. F. Fischer, *Chem. Phys.* **86** (1984) 269.

[75] N. Lu and S. Mukamel, *J. Chem. Phys.* **95** (1991) 1588.

[76] F. C. Spano and S. Siddiqui, *Chem. Phys. Lett.* **314** (1999) 481.

[77] F. C. Spano, *J. Chem. Phys.* **116** (2002) 5877.

[78] F. C. Spano, *J. Chem. Phys.* **118** (2003) 981.

[79] I. G. Lang and Y. A. Firsov, *JETP (U.S.S.R.)* **43** (1962) 1843.

[80] P. M. Morse and H. Feshbach, Methods of Theoretical Physics, McGraw-Hill, New York, 1953.

[81] W. T. Simpson and D. L. Peterson, *J. Chem. Phys.* **26** (1957) 588.

[82] Z. G. Soos, S. Ramasesha, D. S. Galvão, and S. Etemad, *Phys. Rev. B* **47** (1993) 1742.

[83] S. Ramasesha, D. S. Galvão, and Z. G. Soos, *J. Phys. Chem.* **97** (1993) 2823.

[84] M. Möbus, N. Karl, and T. Kobayashi, *J. Crystal Growth* **116** (1992) 495.

[85] E. Hädicke and F. Graser, *Acta Cryst. C* **42** (1986) 189.

[86] F. Wooten, Optical Properties of Solids, Academic Press New York, 1972.

[87] R. Brendel, *J. Appl. Phys.* **71** (1992) 1.

[88] M. Hoffmann, Z. G. Soos, and K. Leo, *Nonlinear Optics* **29** (2002) 227.

[89] T.-W. Wu, D. W. Brown, and K. Lindenberg, *Phys. Rev. B.* **47** (1993) 10122.

[90] A. Y. Kobitski, R. Scholz, I. Vragović, H. P. Wagner, and D. R. T. Zahn, *Phys. Rev. B* **66** (2002) 153204.

[91] R. Scholz, I. Vragović, A. Y. Kobitski, M. Schreiber, H. P. Wagner, and D. R. T. Zahn, *phys. stat. sol. b* **234** (2002) 402.

[92] E. Umbach, W. Gebauer, A. Soukopp, M. Bässler, and M. Sokolowski, *J. Lum.* **76-77** (1998) 641.

[93] H. Fidder, J. Knoester, and D. A. Wiersma, *J. Chem. Phys.* **95** (1991) 7880.

[94] K. Schmidt, Electronic Excited States in Quasi-Onedimensional Organic Solids with Strong Coupling of Frenkel and Charge-Transfer Excitons, Ph. D. thesis, TU Dresden, 2002.

[95] Y. Kayanuma, *Phys. Rev. B* **38** (1988) 9797.

[96] V. Agranovich, K. Schmidt, and K. Leo, *Chem. Phys. Lett.* **325** (2000) 308.

[97] K. Schmidt, *Phys. Lett. A* **293** (2002) 83.

[98] K. Schmidt, K. Leo, and V. M. Agranovich, 'Surface states and quantum confinement in linear molecular chains with strong mixing of Frenkel and charge-transfer excitons', in: V. M. Agranovich and G. C. L. Rocca (Eds.), Organic Nanostructures: Science and Applications. Proceedings of the International School of Physics "Enrico Fermi", Course CXLIX, Varenna, 2001, IOS Press, Amsterdam, 2002, pp. 521–541.

[99] E. I. Rashba, 'Self-trapping of excitons', in: E. I. Rashba and M. D. Sturge (Eds.), Excitons, North-Holland, 1982, p. 543.

[100] V. M. Agranovich and A. M. Kamchatnov, *Chem. Phys.* **245** (1999) 175.

[101] J. M. Turlet, P. Kottis, and M. R. Philpott, *Advan. Chem. Phys.* **54** (1983) 303.

[102] E. V. Tsiper, Z. G. Soos, W. Gao, and A. Kahn, *Chem. Phys. Lett.* **360** (2002) 47.

[103] F. F. So, S. R. Forrest, Y. Q. Shi, and W. H. Steier, *Appl. Phys. Lett.* **56** (1990) 674.

[104] V. Agranovich, R. Atanasov, and G. Bassani, *Chem. Phys. Lett.* **199** (1992) 621.

[105] M. Leonhardt, O. Mager, and H. Port, *Chem. Phys. Lett.* **313** (1999) 24.

[106] T. W. Canzler, Ultrafast Dynamics in Quasi-One-Dimensional Organic Molecular Crystals. Self-Assembled Monolayers of Photochromic Molecules, Ph. D. thesis, TU Dresden, 2002.

[107] HyperChem, Computational Chemistry (Manual), Hypercube, Inc., Waterloo, Ontario, Canada, 1996.